UNIVERSITA' DEGLI STUDI DI PAVIA

FACOLTA' DI SCIENZE MM, FF, NN

CORSO DI LAUREA MAGISTRALE IN SCIENZE FISICHE

Thermal and Epithermal neutron beam tailoring for BNCT research at CN proton accelerator of INFN Legnaro National Laboratories

Relatore
Dott. Silva Bortolussi
Correlatore
Chiar.mo Prof. Saverio Altieri

Tesi di laurea di:
Jacopo Valsecchi
Matricola:
414059

Anno Accademico 2013/2014

Contents

List of Figures

Introduction

In radiotherapy, a large dose of radiation is delivered to the tumor with the purpose of destroying and damaging the cancer cells, without exceeding the tolerance dose of the surrounding healty tissues. Conventional external radiotherapy is usually delivered via high-energy photons or electrons, but new techniques are being developed as *Hadrontherapy*, which uses protons and ions to deliver a lethal radiation dose to the cancer cells.
The idea of *neutron capture therapy (NCT)* is to selectively target tumor cells by *higt-LET* heavy particle radiation, which is released when a tumor-seeking compound is exposed to an external neutron field [1]. In *Boron Neutron Capture Therapy (BNCT)* a pharmaceutical compound carrying ^{10}B and able to concentrate selectively into the tumour cells, is administered to the patient, and subsequently, the target is irradiated by an external neutron beam. ^{10}B has a large capture cross section of 3830 barns for thermal neutrons [2] and ^{11}B created in the capture reaction decays into highly energetic short-range ($<10\mu m$) particles, an α-particle and ^{7}Li nucleus, with a $Q = 2.79\,MeV$:

$$^{10}B(n,\alpha)^{7}Li.$$

The initial clinical BNCT trials were carried out with the thermal neutron beam on malignant tumors at Brookhaven National Laboratory.
This first clinical trial did not show the expected results because the thermal neutrons penetrated insufficiently into the deep-seated tumors, damaging the shallow tissues. From 1990's, thermal neutrons were substituted with higher energy epithermal neutrons. The optimum neutron beam energy for treating deep seated tumors with BNCT was found to be in the range between 4 eV and 40 KeV, with the maximum of the spectrum located around 10 keV [3]. Clinical BNCT trials were started in Japan, USA, Argentina and Europe combining *sodium borocaptate*, *BSH*, and epithermal neutron beams in brain cancer treatments [4]. Epithermal neutron beams combined with *boronophenylalanine, BPA*, were then employed in brain, head and neck cancer treatments in Japan [5], in Sweden [6] and in Finland [7]. The first human liver cancer patients were treated with thermal neutrons in an isolated liver after surgical removal of the organ from the patient at Pavia University and INFN [8]. The first BNCT for hepathic tumour without organ expantation was carried out at Kyoto University Research Reactor (KUR) in Japan: a patient with multiple inoperable liver tumors received BNCT without surgical procedure, using a newly developed boron delivery system [9]. Phase I/II protocol for treating cutaneuos melanomas with BNCT was designed in Argentina by the *Comision Nacional de Energia Atomica* and the medical center *Instituto Roffo*, employing BPA as boron carrier and an hypertermal beam (mixed thermal and epithermal) [10].
Originally, BNCT was applied as the last salvage therapy for heavily pretreated patients with recurrent cancer, but, in 2010, it was successfully applied as the first-line treatment of a large inoperable head and neck tumor in combination with intensity-modulated chemoradiotherapy in Finland [11].
Nowadays, in many resarch and clinical centers BNCT is being investigated as a primary or adjuvant therapy for many types of tumours such as lung cancer, mesothelioma, osteosarcoma and others.

Due to the high neutron flux required (about $10^9\ cm^{-2}\, s^{-1}$), all clinical BNCT trials have been carried out using reactor based neutron beams, moderated by different materials and compounds such as graphite, lead, iron, aluminium and Fluental^{TM}. As an alternative to nuclear reactors, accelerator-based neutron sources offer a number of petential advantages. First, neutrons are not produced via critical assembly of fissile material, thus regualtions associated with maintaining the source are substancially simplified. Second, the variety of nuclear reactions that it is possible to exploit via proton or deuteron interaction, allow for a number of neutron energy spectra to be produced. Consequently a clinical neutron beam can be easily produced by tailoring the moderator according to the tumour that must be treated [12].
An accelerator-based neutron source, *ABNS*, for BNCT is composed by many components: the accelerator hardware for producing a high-current charged particle beam, a neutron-producing target, the heat removal system and the moderator/reflector assembly to tailor the flux spectrum, this last part of the facility is named Beam Shaping Assembly (BSA). Progress has been made on designing, manufacturing and testing various components of the ABNS, and today it is possible to construct accelerators able to produce suitable neutron beams for clinical applications.
Different accelerator types have been proposed as potential candidate, such as Cyclotrons, Linear Accelerators, Electrostatic Linear Accelerators and Rf Linear Accelerators [12, 13]. The *MUNES* project [14] at INFN-Laboratori Nazionali di Legnaro (INFN-LNL, Legnaro, Italy), in collaboration with INFN section of Pavia, concerns the development of an accelerator-based RFQ machine for BNCT.
This thesis has been performed in this context, in particular it was dedicated to the design of a BSA for two neutron beams at the CN accelerator in Legnaro National Laboratories. This accelerator provides a proton beam of the same energy as the RFQ developed for BNCT but with lower current. It is in fact coupled with a beryllium target surrounded by a graphite moderator. The neutron beams optimized at this facility will be of high interest for BNCT research, in particular to perform neutron dosimetry and microdosimetry experiments. The main characteristic of this facility is that it will provide two beams of different energy spectra, that will be employed for measurements in two relevant BNCT clinical scenarios: an epithermal beam used for deep-seated tumours and a thermal beam used for shallow ones. The *Monte Carlo N-Particle Transport Code, (MCNP6),* was used as a simulation tool for tailoring and evaluating the suitability of the BSA of the compact accelerator-based neutron sources. The MCNP code is widely used, due to its reliability and great flexibility in coupled photon-neutron transport calculations.
This thesis is made up of 6 chapters and 3 Appendixes:

Chapter 1 introduces the most important concepts connected to the neutron production reaction of interest in BNCT.

Chapter 2 describes the implementation of the MCNP6 code used for simulating the neutron source and the geometry of the facility.

Chapter 3 figures out the design of the thermal neutron beam.

Chapter 4 works out, step by step, the tailoring of the epithermal neutron beam.

Chapter 5 evaluates the radiation dose contribution of thermal neutrons, epithermal neutrons, fast neutrons and gamma-rays to the environment for a radioprotection issues.

Chapter 6 conclusions.

Appendix A reports the cross-sections of the elements that have been considered for the construction of the BSA.

Appendix B reports the elemental composition of the materials used in the simulation.

Appendix C reports the whole *MCNP6* code of the final BSA.

Chapter 1

Neutron Sources

Free neutrons do not exist in nature and must be artificially produced by nuclear reactions. In the following paragraphs, the various types of reactions useful for this goal and some concepts of neutron physics are described.

1.1 Cross-Section and Neutron Flux

Neutrons are neutral particles. Neither the electrons surrounding a nucleus nor the electric field caused by a positively charged nucleus affect a neutron's flight. Thus neutrons travel in straight lines, deviating from their path only when they actually collide with a nucleus to be scattered into a new direction or absorbed. If neutrons interact with atomic nuclei, they can produce a variety of nuclear reactions. It is convenient to describe each type of interaction in terms of a characteristic cross section: *elastic scattering cross section*, σ_s, *inelastic scattering cross section*, σ_i; etc. The sum of the cross section for all possible interactions is known as the *total cross section*:

$$\sigma_t = \sigma_s + \sigma_i + \sigma_\gamma + \sigma_f + ... \tag{1.1}$$

The sum of the cross sections of all absorption reactions is known as the *absorption cross section*:

$$\sigma_a = \sigma_\gamma + \sigma_f + \sigma_p + \sigma_\alpha + ... \tag{1.2}$$

The interaction rate can be found by a straightforward generalization. If we introduce the function $n(r, \omega)$ which is the *neutron density distribution function* and it is defined so that $n(r, \omega)d\Omega$ is the number of neutrons per cm^3 at the point r whose velocity vectors lie within the differential solid angle $d\Omega$ about the direction ω; the interaction rate per unit volume $F(r, \omega)$ is:

$$F(r) = \Sigma_t \int_{4\pi} n(r, \omega) v d\Omega = \Sigma_t n(r) v. \tag{1.3}$$

where Σ_t is the macroscopic cross section and v is the speed of neutrons assumed to be constant.

The quantity $n(r)v$ is called the *one-velocity neutron flux*:

$$\phi(r) = n(r)v. \tag{1.4}$$

From Eq. 1.3 the interaction rate per unit volume is:

$$F(r) = \Sigma_t \phi(r). \tag{1.5}$$

In these calculation only monoenergetic neutrons have been considered, this can easly be generalized by incorporating the energy distribution of the neutrons in the neutron density distribution function, and the neutron flux turns:

$$\phi(r) = \int_{E_1}^{E_2} dE \int_{4\pi} d\Omega \phi(r, E, \omega). \tag{1.6}$$

Neutrons are divided into three groups according to their kinetic energy:

Thermal Neutrons with $E < 0.5\, eV$.

Epithermal Neutrons with $0.5\, eV < E < 10\, keV$.

Fast Neutrons with $10\, keV < E < 20\, MeV$.

Different reactions can occour due to the interaction of neutrons and the following division is used [15]:

Elastic scattering may take place via compound nucleus formation followed by the emission of a neutron that returns the compound nucleus to the ground state of the original nucleus. In such a resonance elastic scattering event the kinetic energy of the original neutron-nuclear system is conserved. The neutron and the nucleus may also interact without neutron absorption and the formation of a compound nucleus.

Inelastic scattering plays an important role in nuclear reactor theory. It appears when the compound nucleus formed by neutron capture decays by the emission of one neutron, leaving the nucleus in an excited state which subsequently undergoes further delays. The energy of the emitted neutron can be considerably lower than the energy of the incident neutron. If the compound nucleus decays by the emission of two or more neutrons, the events are referred to as *(n,2n)*, *(n,3n)*, and so on.

Radiative capture can occur at all energies, but it is most probable at low energies. In this process the compound nucleus decays with the emission of one or more gamma rays. The energy of the emitted gamma is equal to the difference in the excited- and ground-state energy levels of the compound nucleus. The resonances characterizing the cross sections over certain ranges correspond to the discrete excited states of the compound nucleus that is formed upon neutron capture.

Fission process consists of splitting a nucleus into roughly equal parts and it occurs when a neutron is absorbed into a heavy nucleus forming a compound, instable nucleus. The amount of excitation energy required to enable nuclear fission depends on the magnitude of the electrostatic barrier and the dissociation energy of the fission in question.

The microscopic cross section behavior as a function of energy can be summarised as:

Capture and fission : 1/v + resonances.

Elastic scattering : constant/decreasing + resonances.

Inelastic scattering : threshold reaction; for light nuclides a few MeV, for heavy nuclides 10 – 100 keV.

In the neighborhood of a single isolated resonance, the cross section can be described by the *Breit-Wigner Formula*:

$$\sigma_{n,\gamma} = \frac{\lambda^2}{4\pi} \frac{\Gamma_n \Gamma_\gamma}{(E - E_R)^2 + (\Gamma/2)^2}. \tag{1.7}$$

As an example of the different cross section behaviours of each interaction is shown in Fig. 1.1. The cross section plots of all the elements considered in the simulations are reported in Appendix A.

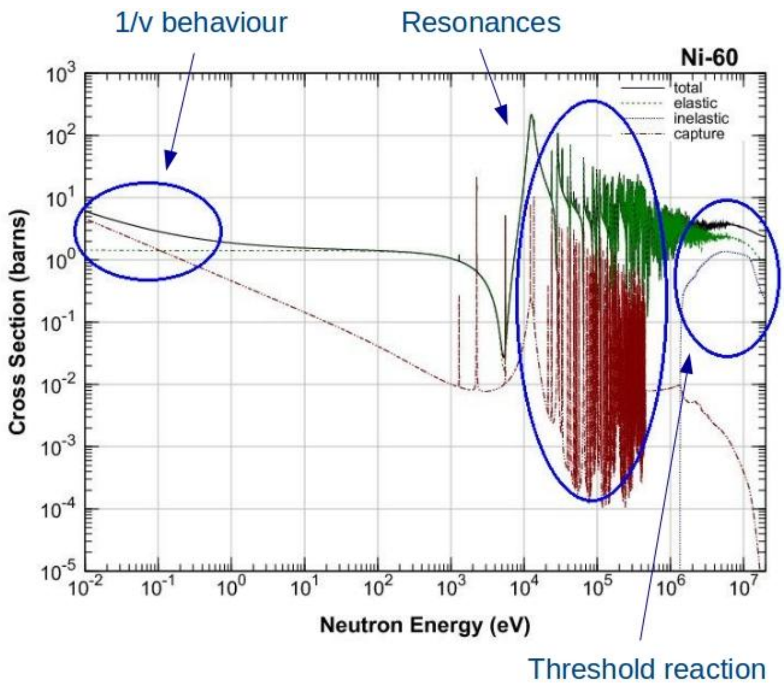

Figure 1.1: Cross section behaviour.

1.2 Thermal Neutrons

Free neutrons introduced into an infinite, non absorbing medium, remain there for an infinitely long time. Then equilibrium is established between the neutrons and the thermal motion of the scattering atoms, distributing as a Maxwellian with the temperature of the scattering medium. Such an ideal case does not occur, because all media capture neutrons to different extents. When the source emits neutrons with energies higher than thermal energies, a certain time elapses before a neutron is *thermalized*. Thus, if the medium is not infinite, there is a certain probability that the neutron is lost by absorption or leakage (in case of a finite medium) before its complete thermalization; that means, in this case, that the equilibrium is never reached. However, in a good moderator that is sufficiently large and only weakly absorbent, the neutron energy distribution at the end of the slowing-down process approximates an equilibrium distribution.
According to the Maxwell distribution law the number of neutrons of energy E per unit energy interval, $N(E)$, and the number of neutrons of velocity v per unit velocity interval, $N(v)$, can be expressed in terms of the neutron velocity:

$$\frac{dN_0}{dv} = N(v) = \frac{4\pi v^2 N_0}{(2\pi kT/m)^{3/2}} e^{-mv^2/2kT}, \tag{1.8}$$

where k is Boltzmann's constant; T is the absolute temperature of the medium; and N_0 is the total number of neutrons per unit volume, that is:

$$N_0 = \int_0^\infty N(v)dv = \int_0^\infty N(E)dE. \tag{1.9}$$

The most probable energy and velocity, respectively, are:

$$v_p = \sqrt{\frac{2kT}{m}}. \tag{1.10}$$

and

$$E_T = \frac{1}{2}mv_p^2 = \frac{1}{2}m(\frac{2kT}{m}) = kT, \tag{1.11}$$

At the room temperature the thermal neutrons energy is:

$$E_0 = kT = 0.025\ eV.$$

If a substance with the cross section $\Sigma(E)$ is placed in a thermal neutrons field, the number of reaction per cm^3 and per sec is given by:

$$F = \int_0^\infty \Sigma(E)\phi(E)dE. \tag{1.12}$$

This reaction rate can be written as the product of the total neutrons flux ϕ and an average cross section $\overline{\Sigma}$. The latter is obtained averaging the flux over the energy distribution of the flux:

$$F = \overline{\Sigma}\phi; \quad \overline{\Sigma} = \int_0^\infty \Sigma(E)(\frac{E}{E_T})e^{-E/E_T}\frac{1}{E_T}dE. \tag{1.13}$$

In the important special case of a $1/v$ absorber:

$$\Sigma_a(E) = \Sigma_a(E_T)\sqrt{\frac{E_T}{E}} \quad \overline{\Sigma}_a = \frac{\sqrt{\pi}}{2}\Sigma_a(E_T). \tag{1.14}$$

The average cross section of a $1/v$ absorber is thus smaller by a factor of $\frac{\sqrt{\pi}}{2}$ than the cross section at the energy E_T. Furthermore for $1/v$ absorbers, the absorption rate is independent of the neutron energy distribution.
The microscopic thermal absorption cross section is:

$$\overline{\sigma}_{a,th} = \frac{\sqrt{\pi}}{2}\sigma_0\sqrt{\frac{T_0}{T}}. \tag{1.15}$$

1.3 Neutron Production by Nuclear Reactions

A particle accelerator suitable for BNCT should have similar costs of the machines for other types of particle therapy, but the critical issue for BNCT is that a high neutron flux is required, thus the accelerator must provide a high proton/deuteron beam intensity. Untill now the accelerator devices were not able to reach sufficient intensities, but in the last few years the technological development of accelerators has produced beam currents up to about 50 mA, enough for BNCT purposes.
From BNCT point of view there are also other advantages related to the employ of accelerators instead of the reactors. It is possible, by manipulating parameters as incident beam, energy, moderator materials and thickness, to produce neutron beams of different characteristics, optimized according to the type of tumours that must be treated. In particular, the spectral characteristics of the neutron beams obtained by accelerators are more advantageous because usually neutrons are produced with lower energies, see Fig. 1.2, i.e. the amount of material necessary to shape the final beam is lower, furthermore γ-rays are emitted in the fission process. In this sense, the quality of the obtained beam is higher in case of accelators.
There are a number of accelerator configurations which deserve some attention, including moderation of beams from high energy proton accelerators, and designs for neutron production at threshold for direct incidence onto the patient without a moderator:

- High energy accelerators;
- Unmoderated neutrons low energy accelerator systems;
- Moderated neutrons low energy accelerator systems.

All these different approaches depend on the material target, used in the accelerator systems and hence the choice of a proton/deuteron beam with an energy spectrum adapted to the aim.

There is a variety of reactions wich lead to neutron production, some reactions proceed directly without the formation of a compound nucleus, such as neutron stripping. In other reactions excited compound nuclei are formed by bombardment of target nuclei with α-particles, protons, deuterons, or γ-rays and then a neutron in the compound nucleus is emitted. The excitation energy is distributed as kinetic energy between the neutron and the residual nucleus, which can remain excited and later return to the ground state by $\gamma - emission$.
The possible types of reactions are:

(α, n) reactions

$${}_zX^A + {}_2He^4 \longrightarrow {}_{z+2}X^{A+3} + n + Q.$$

(d, n) reactions

$${}_zX^A + {}_1H^2 \longrightarrow {}_{z+1}X^{A+1} + n + Q.$$

(p, n) reactions

$${}_zX^A + {}_1H^1 \longrightarrow {}_{z+1}X^A + n + Q.$$

(γ, n) reactions

$${}_zX^A + \gamma \longrightarrow {}_zX^{A-1} + n + Q.$$

For each of them, the Q-value can be > 0 (exothermic reaction) or < 0 (endothermic reaction).

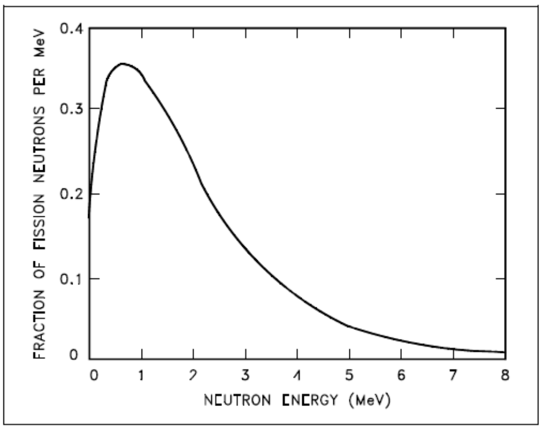

(a) Neutron spectra from a nuclear reactor neutron source [16].

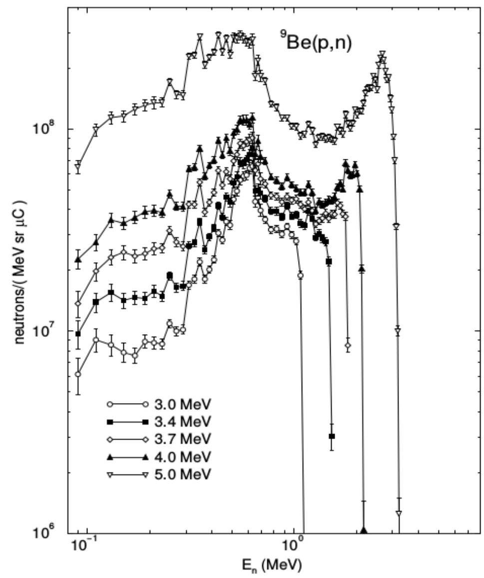

(b) ${}^9Be(p,n)$ neutron spectra at 0 degrees for five energies: 3.0 MeV, 3.4 MeV, 3.7 MeV, 4.0 MeV, and 5.0 MeV [17].

Figure 1.2: Neutron spectra comparison between nuclear reactor neutron source and accelerator-based neutron source.

1.4 (p,n) and (d,n) Reactions

The dependence of the neutrons produced in a (p,n) reaction on the direction of emission is very important. If we denote the energy and mass of the emitted neutron by E_n and m_n, the energy and mass of the projectile nucleus by E and m_G, and the masses of the target and residual nuclei by m_t and m_r ($m_r \approx m_t + m_G - m_n$), then:

$$\begin{aligned} E_n = E\frac{m_G m_n}{(m_n+m_r)^2}\Big\{ & 2\cos^2\theta + \frac{m_r(m_r+m_n)}{m_G m_n}\left[\frac{Q}{E}+\Big(1-\frac{m_G}{m_r}\Big)\right] \\ & \pm 2cos\theta\sqrt{\cos^2\theta + \frac{m_r(m_r+m_n)}{m_G m_n}\left[\frac{Q}{E}+\Big(1-\frac{m_G}{m_r}\Big)\right]}\Big\}. \end{aligned} \tag{1.16}$$

With increasing primary energy, the neutrons are emitted in a cone around the forward direction whose apex angle is given by:

$$\cos\theta_0 = \left|\sqrt{\frac{m_r(m_r+m_n)}{m_G m_n}\left[\frac{|Q|}{E}+\Big(1-\frac{m_G}{m_r}\Big)\right]}\right|. \tag{1.17}$$

Many different neutron-producing reactions could be exploited with an accelerator. The neutron-producing reactions are induced by accelerated protons, deuterons, or tritons targeting ^7Li, ^9Be, ^{12}C, ^{13}C, ^2H, or ^3H nuclei, via the reactions listed in Table 1.1.

Table 1.1: Characteristics of charged particle reactions considered for accelerator-based BNCT [18].

Reaction	Bombarding Energy (MeV)	Average n Energy (MeV)	Max n Energy (MeV)	n Production Rate ($mA^{-1}s^{-1}$)
$^7Li(p,n)^7Be$	2.5	0.55	0.79	$9.1 \cdot 10^{11}$
$^9Be(p,n)^9B$	4.0	1.06	2.12	$1.0 \cdot 10^{12}$
$^9Be(p,n)^9B$	30.0		28	$1.9 \cdot 10^{14}$
$^9Be(d,n)^{10}B$	1.5	2.01	5.81	$3.3 \cdot 10^{11}$
$^{13}C(d,n)^{14}N$	1.5	1.08	6.77	$1.9 \cdot 10^{11}$
$^2H(d,n)^3He$	0.15	2.5	2.5	$4.7 \cdot 10^8$
$^3H(d,n)^4He$	0.15	14.1	14.1	$5.0 \cdot 10^{10}$

1.4.1 Li(p,n)Be Reaction

Probably, the most studied accelerator-based neutron source application is the endothermic $^7Li(p,n)^7Be$ reaction, at approximately 2.5 MeV proton energy, because sufficiently low accelerator current (10 mA) is needed for producing a high intensity of reasonably low-energetic neutrons (up to 1 MeV) [19]. There is a tradeoff between total yield and maximum neutron energy. The $^7Li(p,n)^7Be$ cross section exhibits a large high-energy tail increasing with the incident proton energy that can produce fast neutrons, but this contamination is an unwanted source of background dose delivered to the patient that may limit the effectiveness of the therapy.
The Q-value for this reaction is 1.644 MeV and the threshold energy is 1.881 MeV:

$$^7Li + p \longrightarrow {}^{7*}Be + n - 1.644\,MeV. \tag{1.18}$$

Neutron energy increase with proton energy.. At a proton energy of 2.378 MeV the reaction $^7Li(p,n)^7Be^*$ becomes possible:

$$\begin{aligned} ^7Li + p &\longrightarrow {}^7Be^* + n - 2.076\,MeV \\ &\longrightarrow {}^7Be + \gamma + 430\,keV. \end{aligned} \tag{1.19}$$

Neutrons emerging from the target must be moderated in order to produce a suitable beam for BNCT purposes, according to the types of tumours that have to be treated. To exploit the lithium cross section (see Appendix A.2), a proton current of about 10 mA is required in order to produced the sufficient neutron flux. This current dissipates a high power in the target, producing a thermal shock. Consequently, the removal of heat from an accelerator target is one of the principal technological challenges to be overcome by all low energy accelerator systems. The melting point of lithium metal is around 180^oC, which means that heat removal must be highly efficient to avoid the melting of the target. The minimum beam power requirements for a moderated low energy accelerator system approximates to a proton beam current of 5 mA at an energy of 2.5 MeV [20]. According to the nuclear reaction 1.19, the beryllium radionuclide is formed and this implies in strong activation of the target materials within the device. Furthermore lithium is a material which suffers severe oxidation process in air exposure. Some alternative target materials are Li_2O_3, which has a melting point of 1700^oC, or Li_3N, which should ensure a higher yield [21].
In Argentina a project to develop a Tandem-Electrostatic Quadrupole (TESQ) accelerator for accelerator-based BNCT is under way at National Atomic Energy Commission. The machine is intended to be able to deliver a high intensity proton beam of approximately 30 mA at 2.3-2.4 MeV, [22]. A research study to use a liquid lithium target is under working at the *Soreq research center*, in Israel [23], and at the *Kyoto University Research Reactor Institute* in Japan [24], where the proton beam hits on a film of liquid lithium.

1.4.2 Be(d,n)B Reaction

The use of the $^9Be(d,n)^{10}B$ is promising, especially for the treatment of superficial lesions, this reaction has often been mentioned as possible source of neutrons for BNCT. Being an exothermic reaction, it has the advantage of no threshold and a significant neutron production cross section at relatively low energies. Its drowback is its high Q value which leads to significant fast neutron production, about 4 MeV for 1.5 MeV bombarding energy. However ^{10}B, the heavy product in the $Be(d,n)$ reaction, is a complex nucleus because it has a number of excited sates, but in particular, it has three states at excitation energies between 5.1 and 5.2 MeV, which are strongly populated as soon as they become energetically accessible. Hence, if the final state is one of that group, the reaction becomes effectively endothermic and the emitted neutrons have very small energies depending on the exact bombarding energy. The Q value is $-0.802\,MeV$ and the corresponding threshold is $0.981\,MeV$. At $1.2\,MeV$ bombarding energy, the maximum neutron energy is $0.297\,MeV$, this fact opens the possibility for suppressing most of the fast neutrons produced in this reaction [12].

1.4.3 Be(p,n)B Reaction

Another studied nuclear reaction is the endothermic $^9Be(p,n)^9B$ with a threshold of 2.5 MeV. Its cross section is much lower than the one of protons on Li at the same energy, but in order to get a comparable production, one has to work at energies of about 4 MeV. At these energies, the average neutron energy is higher than the p-Li case. The reason why Be reaction is investigated is to avoid the target cooling problem due to the low melting point of lithium, the melting point of beryllium is in fact around 1300^oC, making it easier

the implementation of a target heat removal system, [12,13].
Furthermore lithium has got another problem: the blistering effect. When the proton goes through the target, it produces hydrogen bubbles, which damage the lithium slab. Beryllium has a low gas permeability, therefore the idea is to realize targets of thin beryllium films brazed on copper substrates target of thin beryllium films welded on copper thiknesses. In this way when the neutron is produced when proton crosses the beryllium film, but then proton is absorbed by copper thus preventing the damage of the target.
The MUNES project at INFN-Laboratori Nazionali di Legnaro (INFN-LNL, Legnaro, Italy) is dedicated to the completion of an accelerator-based neutron beam by bombarding a beryllium target with 5 MeV protons and moderating neutrons through a Beam Shaping Assembly system [14].
At the Kyoto University Research Reactor the cyclotron accelerator (HM-30) manufactured by Sumitomo Heavy Industry is employed to provide a 1 mA, 30 MeV proton beam incidents on a beryllium target. With this setting the proton beam has a 30 kW power. In the reaction between 30 MeV protons and a Be target, the neutrons that are emitted in the forward direction have an energy of up to 28 MeV. In order to reduce the neutron energy range, a BSA composed of a moderator and a sharper has been built [25].
An accelerator-based BNCT facility is now under construction and the entire system including the patient treatment system will be installed in the Ibaraki Medical Center for Advanced Neutron Therapy, in Tokio. The accelerator produces an 8 MeV, 80 kW, 10 mA proton beam impinging on a beryllium target [26,27].

1.4.4 H(d,n)He Reaction

Another solution based on a different kind of devices is to exploit the fusion reaction for yielding neutrons. A compact neutron source based on the exothermic $^2H(d,n)^3He$ (D-D) or $^3H(d,n)^4He$ (D-T) fusion reactions yielding 2.45 MeV and 14.1 MeV neutrons, rispectively, has been suggested for BNCT use [28].

$$\begin{aligned} ^2H + \, ^2H \; &\longrightarrow \; ^3He + \, n + \, 2.5\, MeV; \\ ^2H + \, ^3H \; &\longrightarrow \; ^4He + \, n + \, 14.1\, MeV. \end{aligned} \tag{1.20}$$

These reactions have positive Q-values and thus, low incident energy is required in comparison to the other neutron-producing reactions. The fusion neutron source is compact in size and also safe for hospital use, and are commercialy available. Such neutron sources used to be very common in neutron research facilities and at universities, and thus, the technology required is well know. However, the neutron yield obtained to date with fusion fusion neutron sources is usually of about 10^8 neutron per second. The Plasma and Ion Source Technology group, at the Ion Beam Technology Group, LBNL, has developed high-current D-D fusion neutron generators for various applications with neutron yields up to 10^{11} neutron per second, an intensity not yet sufficient for clinical BNCT. The generators are of various designs, but all are operated with radio-frequency (RF) induction discharge, which ensures high efficiency and long lifetime [29]. Basically, RF induction generates the deuterium plasma in the discharge chamber. An advantage of RF induction discharge is its ability to generate high plasma densities for high extractable ion currents from relatively small discharge volumes. At an energy of 120keV, the $^2H(d,n)^3He$ fusion reaction cross section is already sufficiently high, while it further increases with energies up to 2.4 MeV. The $^3H(d,n)^4He$ fusion reaction cross-section has a maximum at about 120 kV, which is clearly a favorable voltage for D-T neutron production. The D-T fusion reaction cross-section is about 200 times higher than the D-D fusion reaction, and thus the same ion beam current and voltage with D-T fusion provides 200 times higher neutron yield. The most powerful compact D-D neutron generator developed at LBNL is designed to operate with a 330 mA ^2H ion current and 120 kV acceleration voltage providing about 10^{11} neutrons per second. The same neutron generator is aimed to run with mixed ^2H and ^3H gas to yield about 10^{13} D-T fusion neutrons per second.

Chapter 2

Simulation of Be(p,n) Neutron Source

This Chapter is dedicated to the description of the facility, to the simulation of the neutron source emerging from the target and to its validation by comparison with experimental data.

2.1 CN-Accelerator

The CN-Accelerator is a *Van de Graaff* electrostatic device, it is a vertical accelerator about 7 m tall, the high voltage terminal is placed on the top and the electrostatic voltage is uniformly distributed between the 7 MV of the head, down to the ground potential (0 V). The whole structure is contained in a large metal tank, filled in with a high pressure gas (SF_6) having good insulating properties against electrical discharge. The generated ions are inside the terminal, they are protected from its Faraday cage and therefore not affected by the voltage stage of the latter. However, as soon as they are downward driven, from proper deflection as well as electrostatic focusing systems, and leave the terminal region, ions are subject to the electrical field distribution along the vacuum pipe. Such an acceleration process all along the accelerating column, at the end of which a final energy $E = qV$ is gained. Where q is the ion charge state, while V is the difference between the terminal and ground voltages. Accelerated particles are directed towards the target station through a beam selector made by magnetic lenses and deflectors.
This thesis has focused on neutrons generated by 5 MeV proton beam on a beryllium target at CN. An equipped and properly shielded neutron target station, using beryllium, able to exploit the accelerator maximum authorized proton beam current ($3\,\mu A$), providing a neutron source intensity up to $10^9 - 10^{10}\ s^{-1}$ is available.
(http://www.lnl.infn.it/index.php/en/accelerators-3/cn)
The existing set-up of the whole facility is composed of:

- A graphite moderator (length 1110 mm, thickness 1160 mm and height 1425 mm);
- *D_2O Tank* covered by a teflon film (length 570 mm, thickness 400 mm and height 320 mm);
- Vacuum tube cladded by teflon, iron and aluminium films.

The vacuum tube, in the graphite box, leads the proton beam on the beryllium target, Fig 2.1. The D_2O tank, placed around the source, has been tested as first moderator for slowing down the fast neutrons [21,30].
This set-up was firstly simulated by means of MCNP6, version 1, in order to evaluate the

performance of the D_2O tank and the facility design. Subsequently, other set-ups have been tested, characterized by different materials and different orientation of the extracted beams. The goal, was to design a low cost, easy to fabricate BSA which ensures neutron beams with the required spectral characteristics of clinical beams.

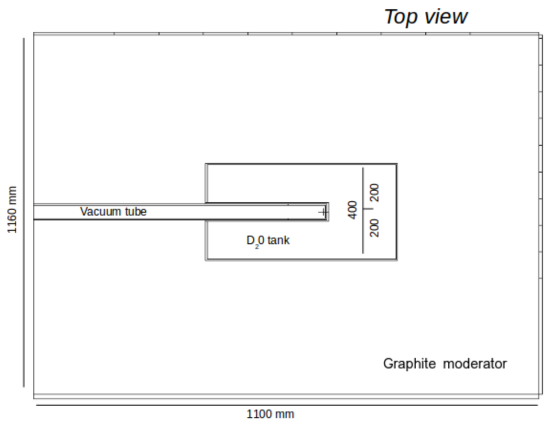

Figure 2.1: First set-up.

2.2 Energy Distribution of neutrons emerging from Be

The neutron spectra emitted form the Be target at CN were measured whith a recoil-proton spectrometer based on a silicon detector for neutron spectrometry in the MeV range by S. Agosteo et al [14]. The detection system consists of a monolithic silicon telescope coupled to polyethylene converter. This detection system is capable of discriminating effectively recoil-protons from secondary electrons generated by background photons. The energy distribution of the neutron yield was measured at 0^o, 20^o, 40^o, 60^o, 80^o, 90^o, 100^o and 120^o angles. The distance between the beryllium target and the detector surface was about $5{\pm}0.1cm$, corresponding to an angular resolution of about 0.6^o. From the kinematics of the ${}^9Be(p,n)^9B$ reaction, it turns out that the maximum neutron energies are about 3.2, 3.1, 3.0, 2.7, 2.5, 2.3, 2.2 and 2.1 MeV for each angle respectively.. The neutron yields distribution versus the laboratory angle shows a maximum close to 0^o and then it drops sharply with increasing angle up to about 60^o where it reaches a minimum value. Up to 120^o it increases again. The total neutron yield of the reaction is determinated by integrating the neutron spectra over the energy range and solid angle and it turns to be $(3.50 \pm 0.3) \cdot 10^{12}\, mC^{-1}$, Fig. 2.2.

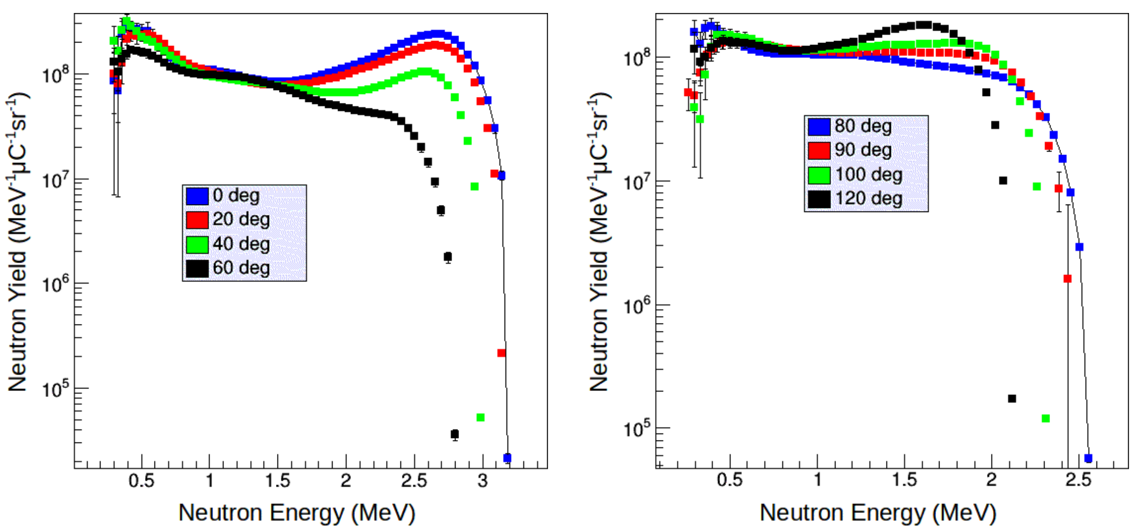

(a) Emission angles: 0^o, 20^o, 40^o and 60^o.   **(b)** Emission angles: 80^o, 90^o, 100^o and 120^o.

Figure 2.2: Distribution of neutron yield measured at different emission angles [14].

2.3 MCNP Source Specification

MCNP6 is the last version of a software package for simulating neutrons, photons, electrons and other charged particles transport, it is developed by *Los Alamos National Laboratory*. The MCNP code is widely used especially in coupled photon-neutron transport calculations [31].
For the purposes of this thesis, it is useful to introduct some features of MCNP code, especially the source specification instructions (called "cards"). A source definition card *SDEF* that can be implemented in MCNP: the user-defined particle source. With this method, the user specifies each variable that characterize the particle emission in the transport problem. In particular, SDEF is followed by the specification of other parameters, as indicated below:

SDEF Variables.

```
c************************************************************
sdef <KEYWORDvar1=values(s)var1> <KEYWORDvar2=values(s)var2>...

Variables:
POS = x y z
SUR = surface number
CEL = starting cell number
VEC = reference vector for DIR in vector notation
DIR = cos of angle between VEC and u,v,w
AXS = reference vector for EXT and RAD in vector notation
RAD = radial distance of the position from POS or AXS
EXT = for a volume source is the distance from POS along AXS,
      for a surface source is th e cosine of angle from AXS .
ERG = starting energy
WGT = starting weight
TME = time
PAR = source particle type
c************************************************************
```

The values of the source variables can be set in three different forms:

Explicit value	sdef ERG=2
Distribution Number	sdef ERG=d1
Function of another variable	sdef POS=d1 ERG FPOS d2

In the distribution number the "*d1*" points to the source info card, *SI*:

Source Info Card

```
c************************************************************
SIn option entries

Options:
H = histogram bin
L = discrete values follow
A = points where probability density function is defined
S = distribution numbers follow
c************************************************************
```

In addition, for each point listed on the *SI* card, the corresponding value of the differential distribution is listed in the source probability card, *SP*.

Source Probability Card

```
c************************************************************
```

```
SPn option entries

Options:
D = bin probabilities
C = cumulative bin probabilities
V = probability proportional to volume
F = built-in functions
c*************************************************************
```

2.4 Source Code

Geometrically, the neutron source was approximated as a point-like source due to the small dimensions of the target. The location of the source is at (42, 27.5, 62), being the origin of the cordinate system at (0, 0, 0). The angular distribution was reproduced starting from the experimental values: the integral of the spectra measured at each angle is the sampling probability of each angle. Thus, while si card reports the angle at which the measurements were performed, the corresponding sp card reports these probabilities. However, being the spectrum continuous in angles, the option A was added to allow MCNP to linearly interpolate for the angles not specified. The same strategy was adopted for energy spectra: si cards were written for each angular distribution reporting the energy binning, and corresponding sp were written with the probability for each energy bin.

Probability density distribution source

```
c ******************************************************************
c  Neutron source Be-9(p,n)
c  beam energy = 5 MeV
c  yielding emission directions:120,100,90,80,60,40,20,0
c  Yield reported in neutron/(sr*microC)
c  Parabolic distribution (si1,sp1) along X axis of absolute ref
c  *****************************************************************
sdef pos 42 27.5 62.0000001 vec=0 0 1 dir=d4 erg fdir=d5
c   ---------------------------------------------------------------
c   yielding directions:  130,120,110,100,95,90,85,80,70,60
c                                   50,40,30,20,10,0
c   ---------------------------------------------------------------
c         130    120   110    100      95       90 85       80
si4    A  -0.6428 -0.5 -0.342 -0.17365 -0.087156 0  0.087156 0.17365
       0.342 0.5 0.6428 0.766 0.866 0.9397 0.98481 1
c      70    60  50     40    30    20     10      0
c
c  yileding direction probability (% total)
c      130    120   110    100      95       90   85    80
sp4   5.6151097499 5.5640632976 5.5130168453 5.4619703931 5.3088310362
      5.1556916794 5.1301684533 5.1046452272 4.8494129658 4.5941807044
      5.6661562021 6.7381316998 7.6569678407 8.5758039816 9.213884635
      9.8519652884
c     70    60  50     40    30    20     10      0
c
c      source spectra in 8 yileding directions
c       (120,  100,  90,  80,  60, 40,   20,  0)
c
ds5 S 31 31 32 32 33 33 34 34 35 35 36 36 37 37 38
c
c       energy bin (MeV) and yielding
c
c -------*---------*---------*---------*---------*---------*---------*
si31 A 0.298 0.328 0.358 0.391 0.426 0.464 0.503
       0.543 0.585 0.627 0.67 0.714 0.758 0.802
       0.847 0.891 0.936 0.982 1.027 1.074 1.12
       1.166 1.212 1.259 1.306 1.353 1.4 1.448
       1.495 1.542 1.59 1.638 1.685 1.733 1.781
       1.829 1.877 1.925 1.973 2.021 2.069 2.118
sp31   114600 90240 99160 117300 125500 132300 129900
       129300 127900 125300 121900 117900 114100 111200
       110000 110800 113000 115900 118200 121000 123800
       127300 131700 137700 144300 151300 158700 166500
       172700 177000 178900 177700 173100 165500 152700
       132300 106400 78360 51220 27620 9915 170.783
si32    ....
sp32    ....
```

```
si38     ....
sp38     ....
c ****************************************************************
```

To verify if the si and sp cards reproduced adequately the experimental values, a run was performed scoring the energy of neutrons at the same angles and in the same energy ranges as the experimental ones and compared with the data. The comparison is shown in Fig. 2.3, 2.4, 2.5 and 2.6 showing a very good agreement. This demonstrates the correctness of the source description.

The score of the quantities of interest in MCNP are called tallies. There are several types of tallies that can be computed (see MCNP Manual , [31]),but in this work three tallies have been employed: F2 and F4, that calculate the neutron flux in a surface and in a cell, respectively. Cells are the units of the geometry in MCNP: parts of the volume of the problem characterized by homogeneous material and density and delimited by surfaces. The flux is calculated by MCNP by averaging the track length of the particles in the volume of interest. The tallies can be modified by separating the results in user-defined energy range or directions range (in case of current).

Moreover the flux tally can be coupled with the kerma factors in order to calculate doses. In particular card F4 is associated with the cards:

DEn and DFn cards are a dose energy and dose function, these features allow entering a pointwise response function (such as flux-to-dose conversion factors) as a function of energy to modify a regular tally.

The kerma factors and the absorption coefficients, for neutrons and photons respectively, were taken in [32, 33]. (http://www.nist.gov/pml/data/radiation.cfm)

Another method to produce results with MCNP is to implement mesh tallies, that is a grid superimposed on the geometry of the problem where the flux is calculated. This method allows visualizing flux distribution over the geometry by a color map.

In general, all the results are given in MCNP per unit of source particle, thus the user must normalize the tally by the intensity of the source to obtain the flux or the dose in the specific cases. In this thesis, tallies were normalized by the factor $2.58 \cdot 10^9\ \mu C^{-1}$. To accomplish this, the tally multiplier card FM was used:

FMn card integrates the flux with any function of energy, typically a cross section. It can be used also to multiply the tally by a constant.

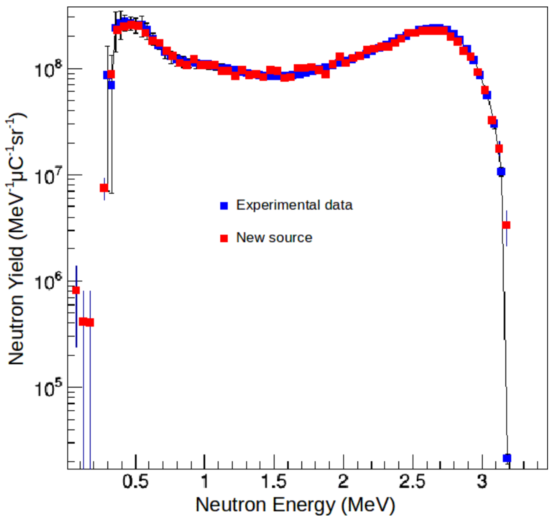

(a) Emission angle: 0^o.

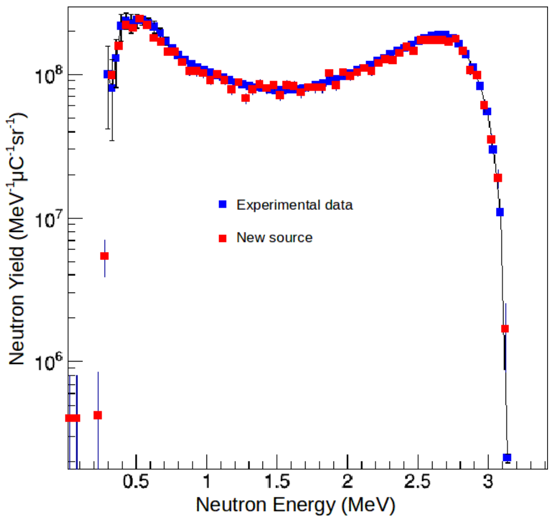

(b) Emission angle: 20^o.

Figure 2.3: Distribution of neutron yield sampled at 0^o and 20^o with the implemented source.

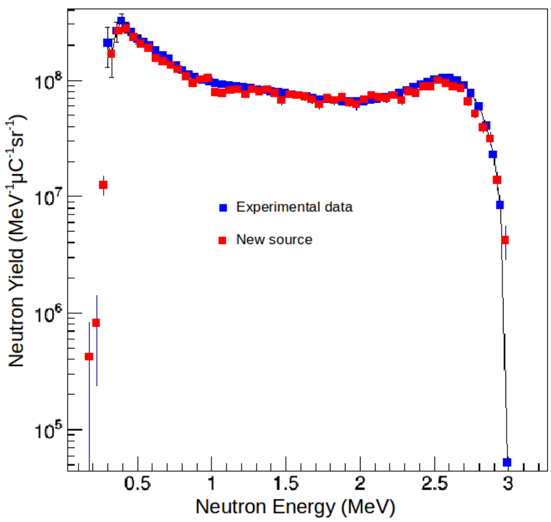

(a) Emission angle: 40^o.

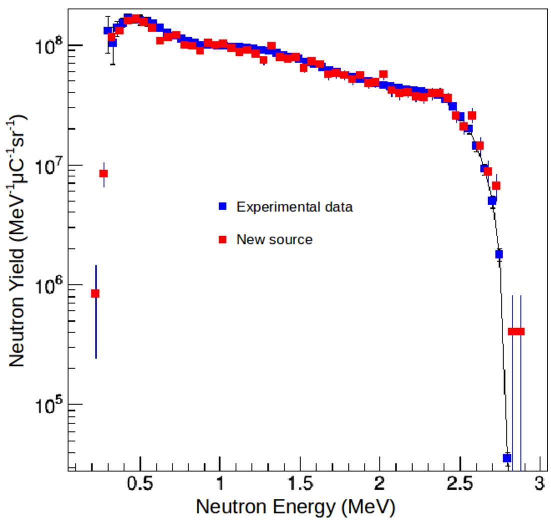

(b) Emission angle: 60^o.

Figure 2.4: Distribution of neutron yield sampled at 40^o and 60^o with the implemented source.

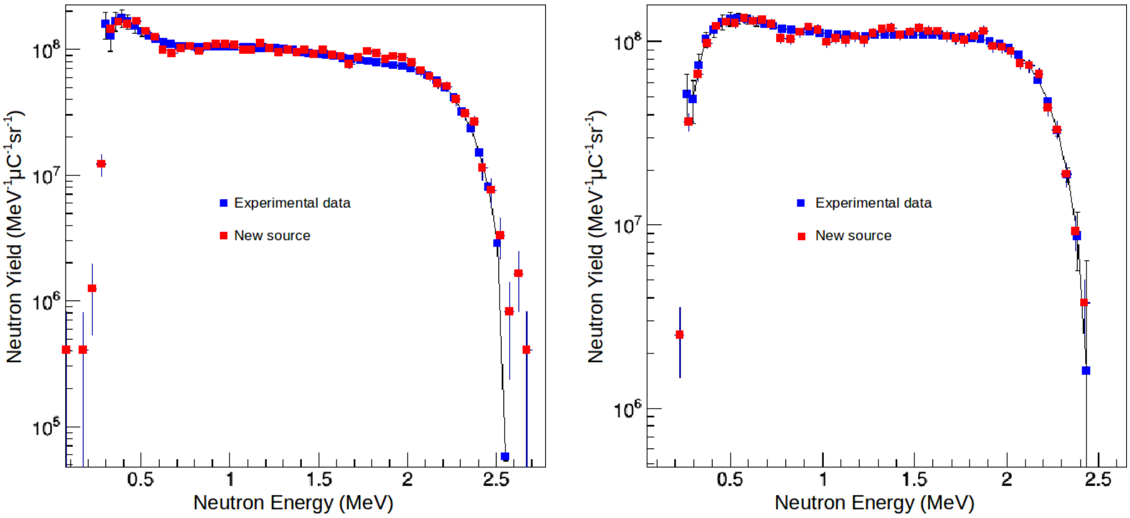

(a) Emission angle: 80^o.

(b) Emission angle: 90^o.

Figure 2.5: Distribution of neutron yield sampled at 80^o and 90^o with the implemented source.

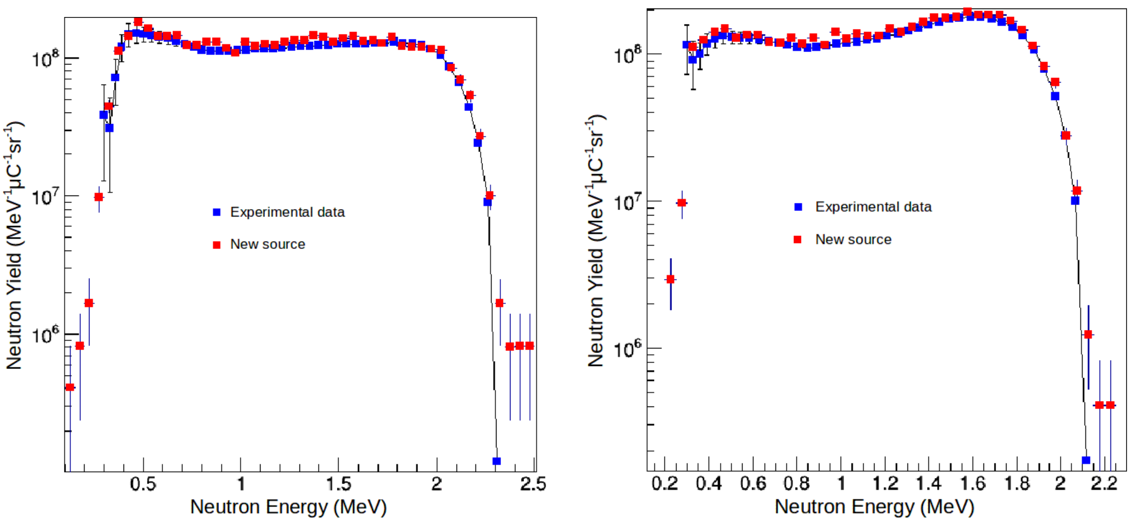

(a) Emission angle: 100^o.

(b) Emission angle: 120^o.

Figure 2.6: Distribution of neutron yield sampled at 100^o and 120^o with the implemented source.

Chapter 3

Tailoring of a thermal neutron beam

This chapter is dedicated to the optimization of a thermal neutron irradiation port at the CN facility. The beam should have the same characteristics required for a clinical BNCT beam dedicated to the treatment of superficial tumours such as skin melanoma: the spectrum of neutrons should be thermal with low epithermal and fast contaminations.

The fact that two beams had to be tailored at the same facility, required careful checks to verify that a change in the configuration of one beam did not change the results obtained for the other. After many simulations, however, it was demonstrated that the tailoring of the two irradiation positions was essentially independent, in particular: the complex set-up necessary for a good epithermal beam did not change significantly the neutron spectrum and the flux obtained at the thermal irradiation position. Thus this chapter reports the work in its subsequent phases: a first optimization of the facility with the existing set-up, characterized by the presence of a heavy water tank, followed by the simulations performed after its removal due to the requirements of the epithermal beam.

Usually a good way to obtain a thermal neutron beam from a neutrons source is *thermalizing* all the fast neutrons with a moderator. The best candidates are the light elements due to the kinematics[1] of the elastic scattering. Hydrogenated materials can thermalize fast neutrons in a few bumps, but also graphite is often used as a moderator due to its scattering cross section (Appendix A) and to the fact that it does not capture thermal neutrons.

3.1 Water Tank

An initial series of simulations has been performed to calculate the thermal neutrons production due to the tank of heavy water placed around the source. D_2O has been considered to be the most efficient and convenient moderating material in which $\gamma - ray$ production by inelastic scattering is minimal [21, 30] and it has a large scattering cross section A.1.

The dimensions of the D_2O tank present at the CN facility are: length 570 mm, thickness 400 mm and height 320 mm and it is covered by a watertight teflon film. The tank is placed around the vacuum tube, but the volume of haevy water is not symmertrical around the target: there is more water towards the upper face (Fig 3.1). To evaluate the effect of this set-up three tallies F4, have been placed on the outer surface of the graphite

[1] Considering the head-on collision between a neutron and a stationary nucleus of atomic mass A and letting E_i and E_f be the neutron energy before and after the collision, the ratio of neutron energies is: $\frac{E_f}{E_i} = \left(\frac{A-1}{A+1}\right)^2$.

box aligned with the source, one is on the frontal face (cell 525) and two are on the sides (cells 624-724), as shown in the Fig. 3.2. At first the neutron flux has been calculated for three neutron energy bins: thermal (from 0 eV to 0.5 eV), epithermal (from 0.5 eV to 10 keV) and fast (from 10 keV). Table 3.1 shows the outcomes of the simulation, the statistical error for each bin is lower than 7%; the values of tallies 624 and 724 are the same due to the symmetrical geometry. The results obtained are satisfactory because the spectrum has a peak at thermal energies. Moreover, the ratio between thermal and total neutron flux is advantageous, in particular at the lateral position it is 94%, thus showing almost no contamination.
In addition to the tallies calculated in the cells, mesh tallies have been employed to visualize the distribution of the neutron flux over the whole geometry (Fig. 3.2). In order to exploit the forward direction to obtain the epithermal beam, the lateral position was chosen as the thermal irradiation port. All the thermal neutrons flux values are evaluated at 1 μA, even if this accelerator can produce a proton current up to 3 μA.

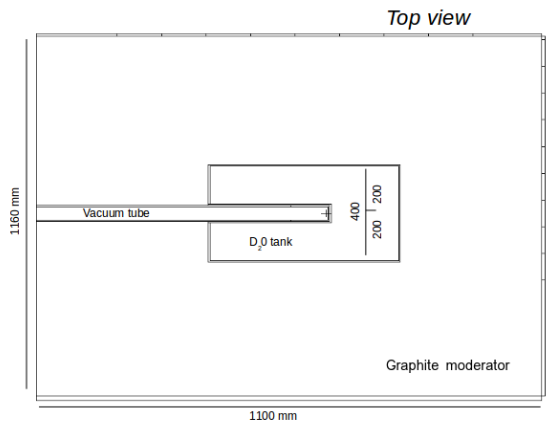

Figure 3.1: CN facility. Set-up characterized by the heavy water tank.

Table 3.1: Neutron flux for the three energy ranges calculated at the three positions. Set-up characterized by the heavy water tank.

Energy Range	Tally 525 Neutron Flux ($cm^{-2}s^{-1}$)	Tally 624 Neutron Flux ($cm^{-2}s^{-1}$)	Tally 724 Neutron Flux ($cm^{-2}s^{-1}$)
0 eV $<$ E $<$ 0.5 eV	$2.08 \cdot 10^5$	$1.14 \cdot 10^5$	$1.14 \cdot 10^5$
0.5 eV $<$ E $<$ 10 keV	$3.51 \cdot 10^4$	$5.12 \cdot 10^3$	$5.12 \cdot 10^3$
E $>$ 10 keV	$5.82 \cdot 10^3$	$1.12 \cdot 10^2$	$1.12 \cdot 10^2$
Total Flux	$2.5 \cdot 10^5$	$1.21 \cdot 10^5$	$1.21 \cdot 10^5$
$\frac{\phi_{the}}{\phi_{tot}}$	83%	94%	94%

To improve the thermalization of the fast neutrons the container has been turned by 90 degrees and a bismuth shield (dimensions 230 mm x thickness 100 mm x height 100 mm) was added to remove the gamma contamination: Fig. 3.3 shows the new geometry to be compared with the original one in Fig. Fig. 2.1.

The same three tallies of the previous case have been calculated and Table 3.2 shows the results. Fig. 3.4 displays the distribution of the thermal neutron flux obtained by mesh tally calculation in this set-up. Furthermore, a calculation of the thermal flux in the lateral position have been performed with a more detailed energy binning (Fig. 3.5).

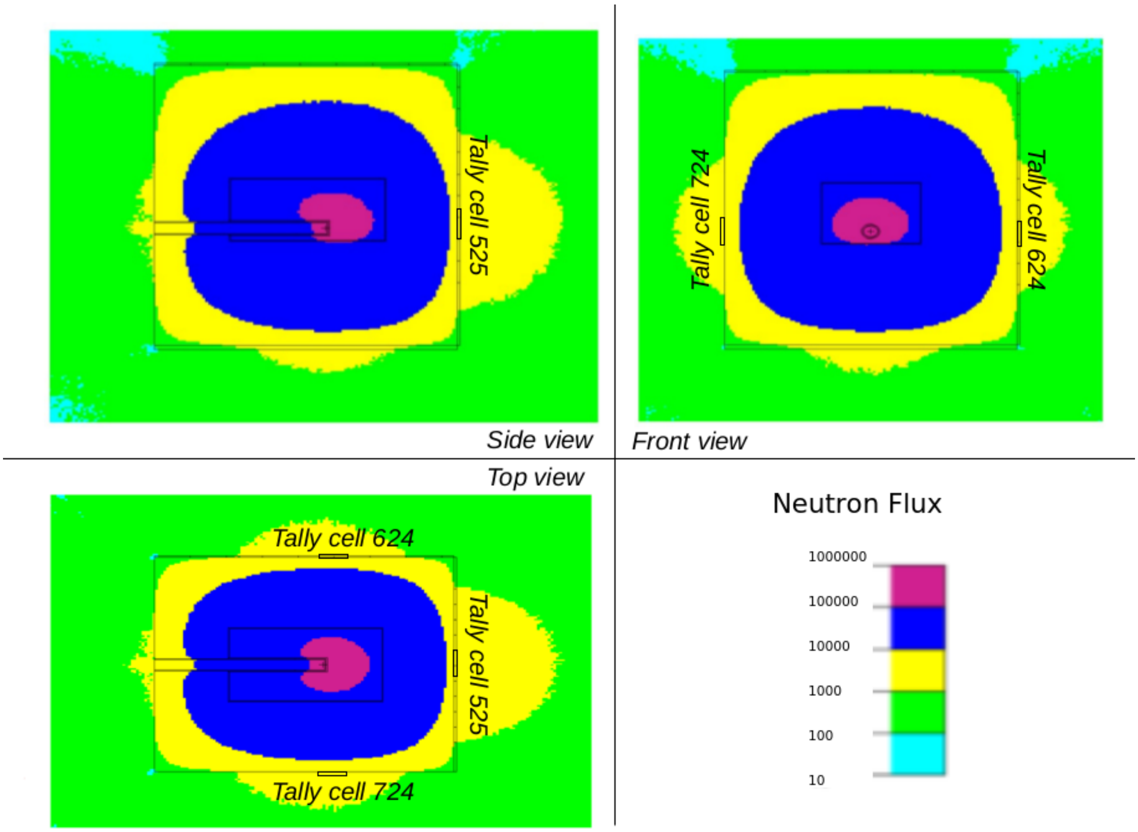

Figure 3.2: Thermal neutron flux distribution superimposed to the geometry of the problem (mesh tally calculation), along the planes centered on the source.

These results show that in the position closer to the bismuth shield (cell 624) the thermal neutron flux is higher than in the previous configuration: the increase is about 45%. The statistical error for each bin is lower than 8%.

Table 3.2: Neutron flux for the three energy ranges calculated at the three positions. Set-up characterized by the rotated heavy water tank.

Energy Range	Tally 525 Neutron Flux $(cm^{-2}s^{-1})$	Tally 624 Neutron Flux $(cm^{-2}s^{-1})$	Tally 724 Neutron Flux $(cm^{-2}s^{-1})$
0 eV $<$ E $<$ 0.5 eV	$2.4 \cdot 10^5$	$1.7 \cdot 10^5$	$1.1 \cdot 10^5$
0.5 eV $<$ E $<$ 10 keV	$5.46 \cdot 10^4$	$1.3 \cdot 10^4$	$1.22 \cdot 10^4$
E $>$ 10 keV	$1.06 \cdot 10^4$	$2.6 \cdot 10^2$	$3.4 \cdot 10^2$
Total Flux	$3.13 \cdot 10^5$	$1.83 \cdot 10^5$	$1.25 \cdot 10^5$
$\frac{\phi_{the}}{\phi_{tot}}$	76%	93%	88%

The heavy water tank set-up has, however, been set aside because with this solution it was not possible to obtain a good epithermal neutron flux (see Chapter 4), due to the high thermalization power of deuterium.

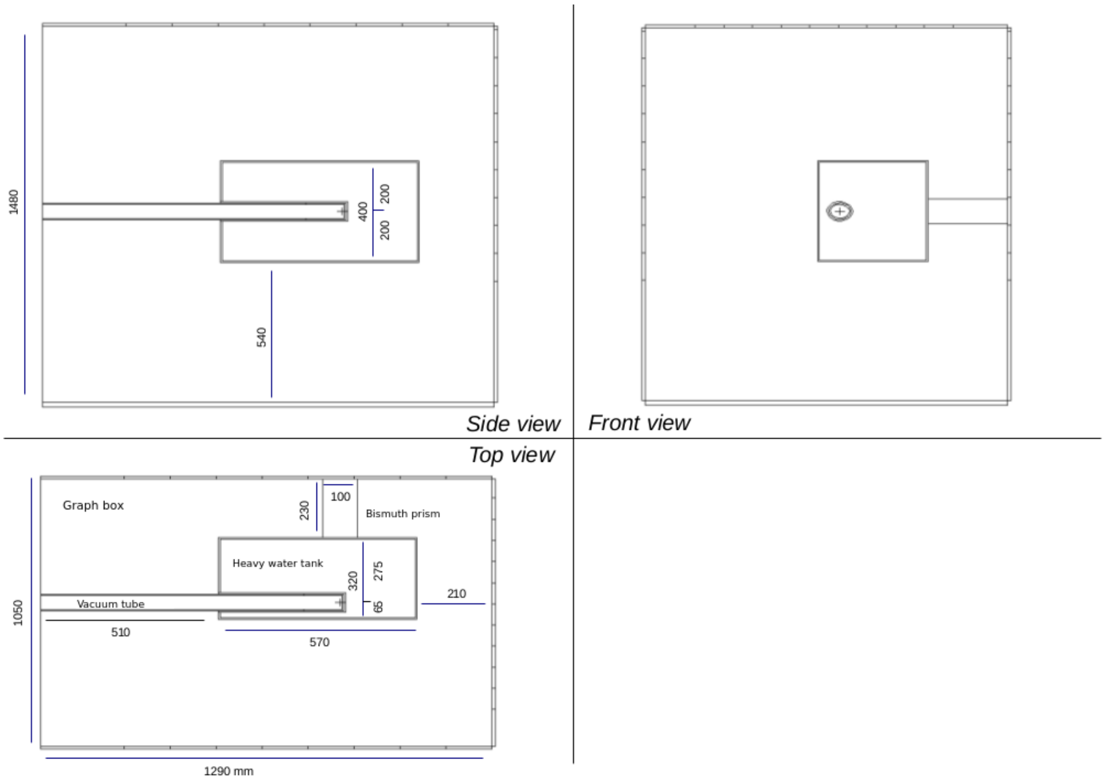

Figure 3.3: Rotated heavy water tank set-up.

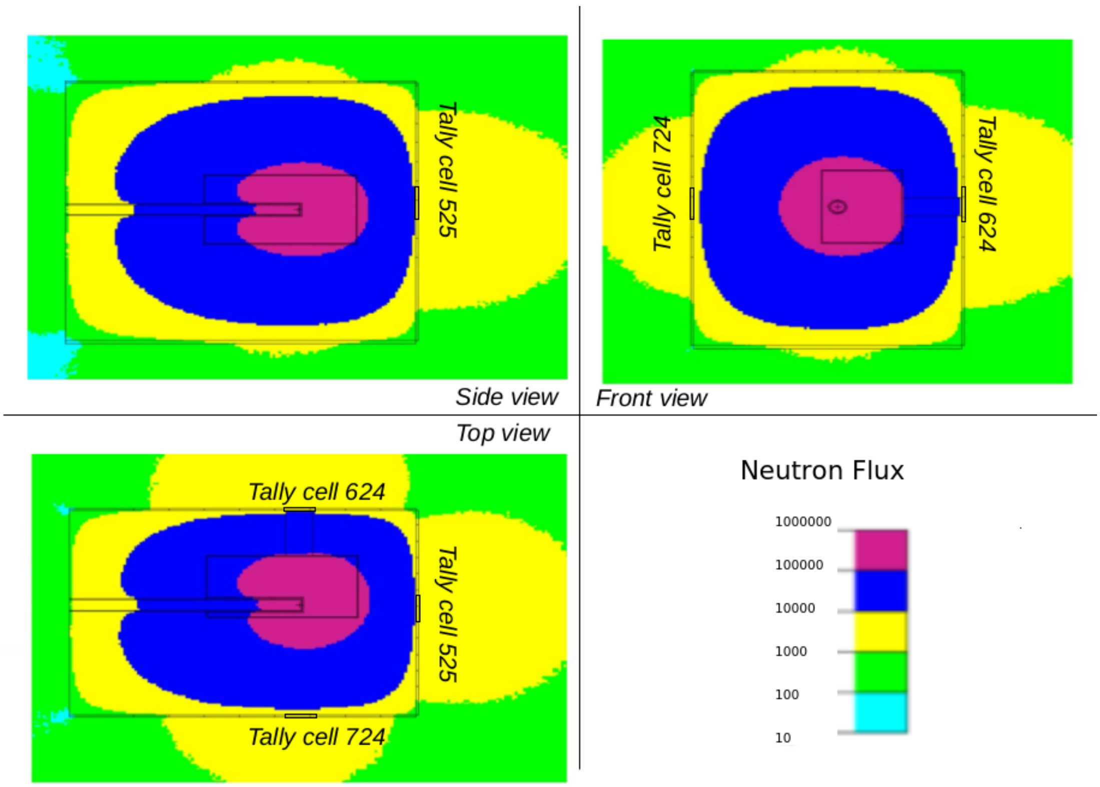

Figure 3.4: Distribution of thermal neutron flux in the set-up with rotated heavy water tank, superimposed to the planes perpendicular to the neutron source. Results were obtained with mesh tallies calculation.

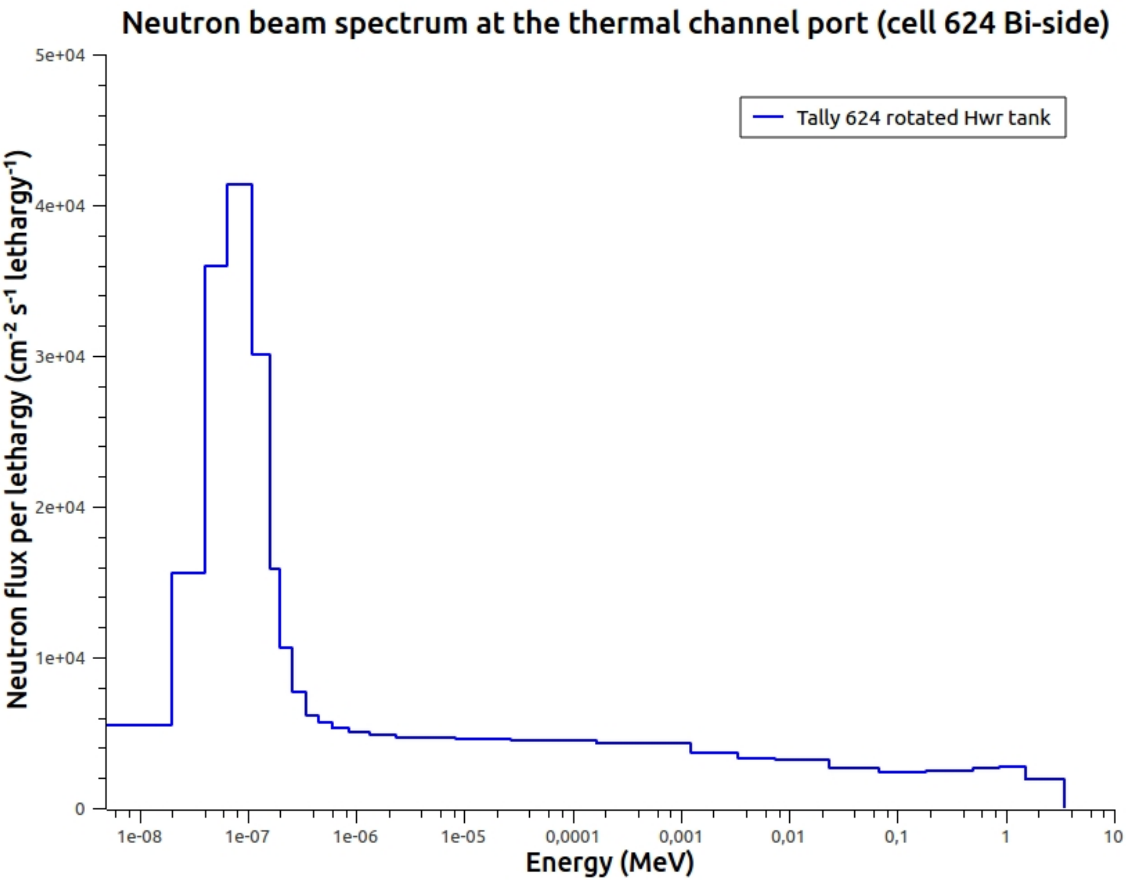

Figure 3.5: Spectrum of neutrons emerging in the sideward direction with the set-up characterized by the rotated heavy water tank. Neutron flux Tally in cell 624.

3.2 Replacing the Water Tank with Graphite

At this stage the heavy water has been replaced by graphite, gaining further freedom in the design of the BSA because the structural constraint of the tank has been removed. New simulations were run with this new configuration, maintaining the dimensions of the graphite box moderator as before. The results achieved are satisfactory because the thermal neutrons flux has not substantially changed, the ratio is slightly decreased, but the value is still acceptable (Table 3.3 and Fig. 3.6). The statistical error for each bin is lower than 6.5%.

Table 3.3: Neutron flux in the three energy rages plus total neutron flux in the forward direction (cell 525), when the heavy water has been replaced with graphite.

Energy Range	Tally 624 Neutron Flux ($cm^{-2}s^{-1}$)
0 eV < E < 0.5 eV	$1.8 \cdot 10^5$
0.5 eV < E < 10 keV	$3.0 \cdot 10^4$
E > 10 keV	$2.5 \cdot 10^3$
Total Flux	$2.2 \cdot 10^5$
$\frac{\phi_{the}}{\phi_{tot}}$	82%

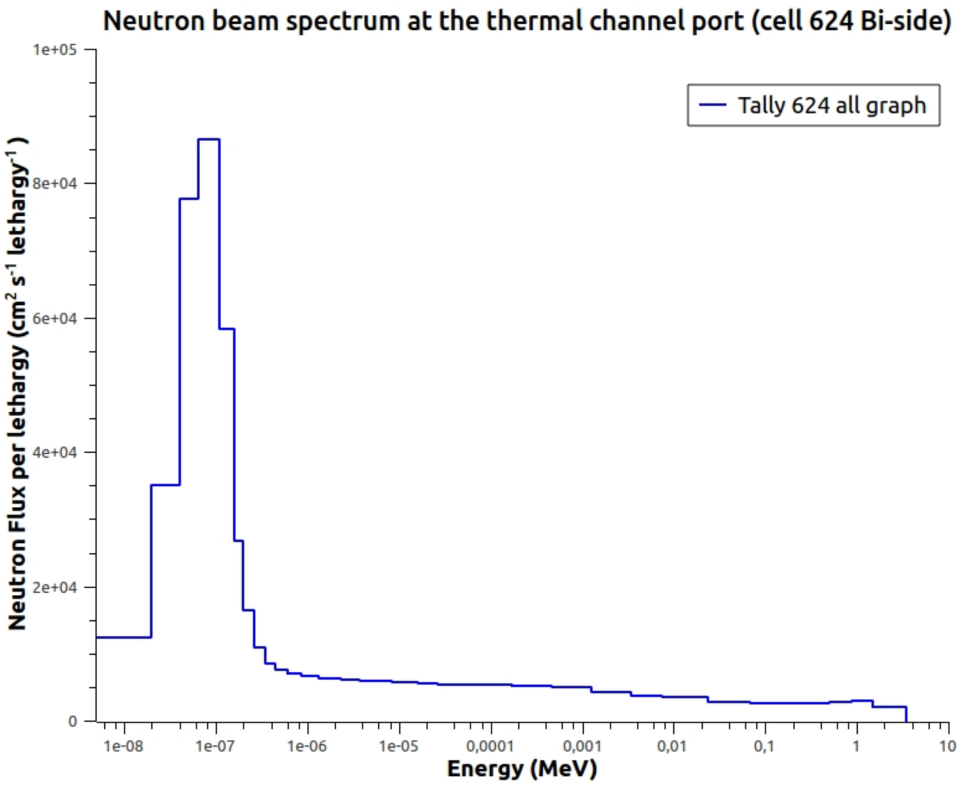

Figure 3.6: Spectrum of neutrons emerging in the sideward direction with the set-up characterized when the heavy water has been replaced with graphite. Neutron flux Tally in cell 624.

3.3 Final Set-up

After several simulations it has been shown that, to thermalize neutrons, it is necessary at least 500 mm of graphite and then other 220 mm of bismuth to absorb γ-rays (Chapter 5). In order to obtain a more compact geometry, some graphite was replaced by a prism of polytetrafluoroethylene (teflon), which is a solid fluorocarbon (Appendix B.4). Teflon is an excellent moderator for fast neutrons due to the fact that the fluorine cross section has got many resonance above 20 keV and below it is constant around 4 barn (Appendix A.8). In this new set-up, between the source and the beam exit port, on cell 624, there is a total thickness of about 620 cm: 170 cm of teflon, 220 mm of graphite and 230 mm of bismuth (Fig. 3.7).

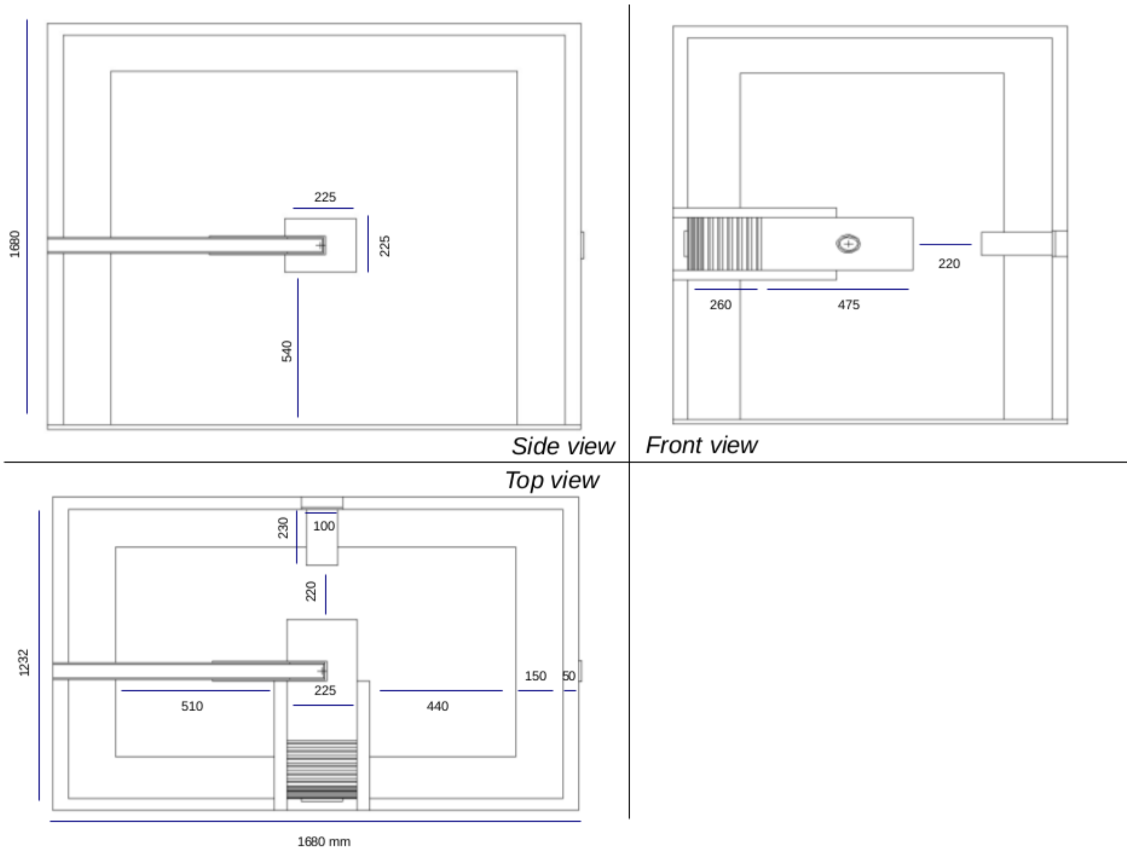

Figure 3.7: Final set-up, the thermal neutron beam port is on the right in the fron view and on the top of the top view. These figures show also the epithermal beam port that will be described in the next Chapter 4

The results obtained are very satisfactory: the neutrons flux shows a maximum at 0.05 eV and then it sharply decreases above 0.4 eV (Fig. 3.9). The thermal neutrons flux is already sufficiently intense at 1 μA, but it could be tripled increasing the proton current to 3 μA. The ratio of the gamma dose and the thermal neutron flux ($\dot{D}_\gamma/ThermalFlux$), the ratio of the dose due to fast neutrons and the thermal neutron flux ($\dot{D}_{fast}/ThermalFlux$) and the ratio of the dose due to epithermal neutrons and the thermal neutron flux per thermal neutrons flux ($\dot{D}_{epi}/ThermalFlux$) are reported in Table 3.4. These values comply with the guidelines provided by IAEA about the characteristics of a clinical thermal neutron beam for BNCT [34]. The flux intensity obtained by the final set-up is half of the one obtained by the heavy water due to the the better thermalization power of deuterium compared to the graphite (Table 3.2 and Table 3.4). The statistical error for each bin is lower than 5.3%. Fig. 3.8 displays the meshes of the final set-up.

Table 3.4: Neutron flux in the three energy ranges of interest, total neutron flux and beam quality parameters obtained with the final set-up shown in Fig. 3.7, compared with IAEA recommendations.

Energy Range	Tally 624 Neutron Flux ($cm^{-2}s^{-1}$)	IAEA guidelines values
0 eV < E < 0.5 eV	$0.9 \cdot 10^5$	
0.5 eV < E < 10 keV	$1.7 \cdot 10^4$	
E > 10 keV	$2.03 \cdot 10^3$	
Total Flux	$1.07 \cdot 10^5$	
$\frac{\phi_{the}}{\phi_{tot}}$	84%	
$\frac{\dot{D}_{epi}}{\phi_{the}}$	$1.2 \cdot 10^{-14}$	$2.5 \cdot 10^{-13}$
$\frac{\dot{D}_{fast}}{\phi_{the}}$	$2.1 \cdot 10^{-13}$	$2.5 \cdot 10^{-13}$
$\frac{\dot{D}_{\gamma}}{\phi_{the}}$	$2.0 \cdot 10^{-13}$	$2.0 \cdot 10^{-13}$

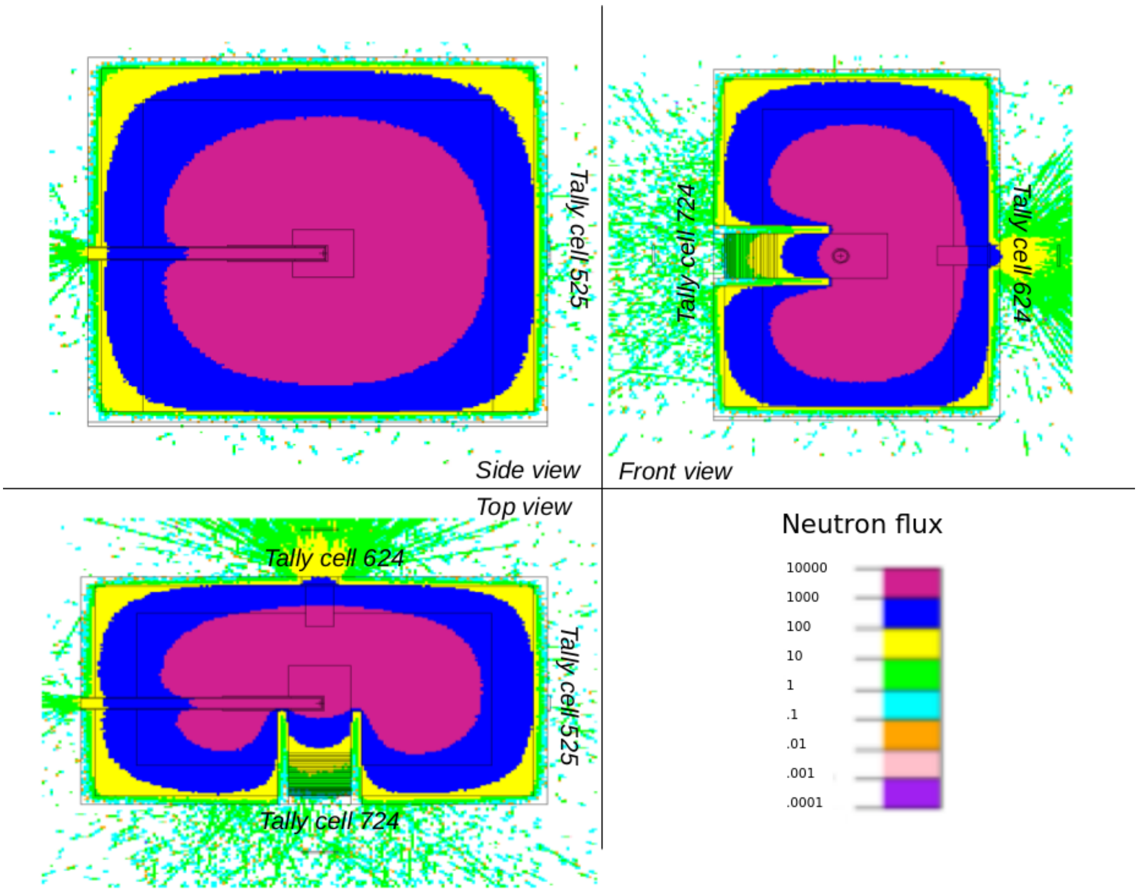

Figure 3.8: Distribution of thermal neutron flux in the final set-up with teflon, graphite and bismuth, superimposed to the planes perpendicular to the neutron source. Results were obtained with mesh tallies calculation.

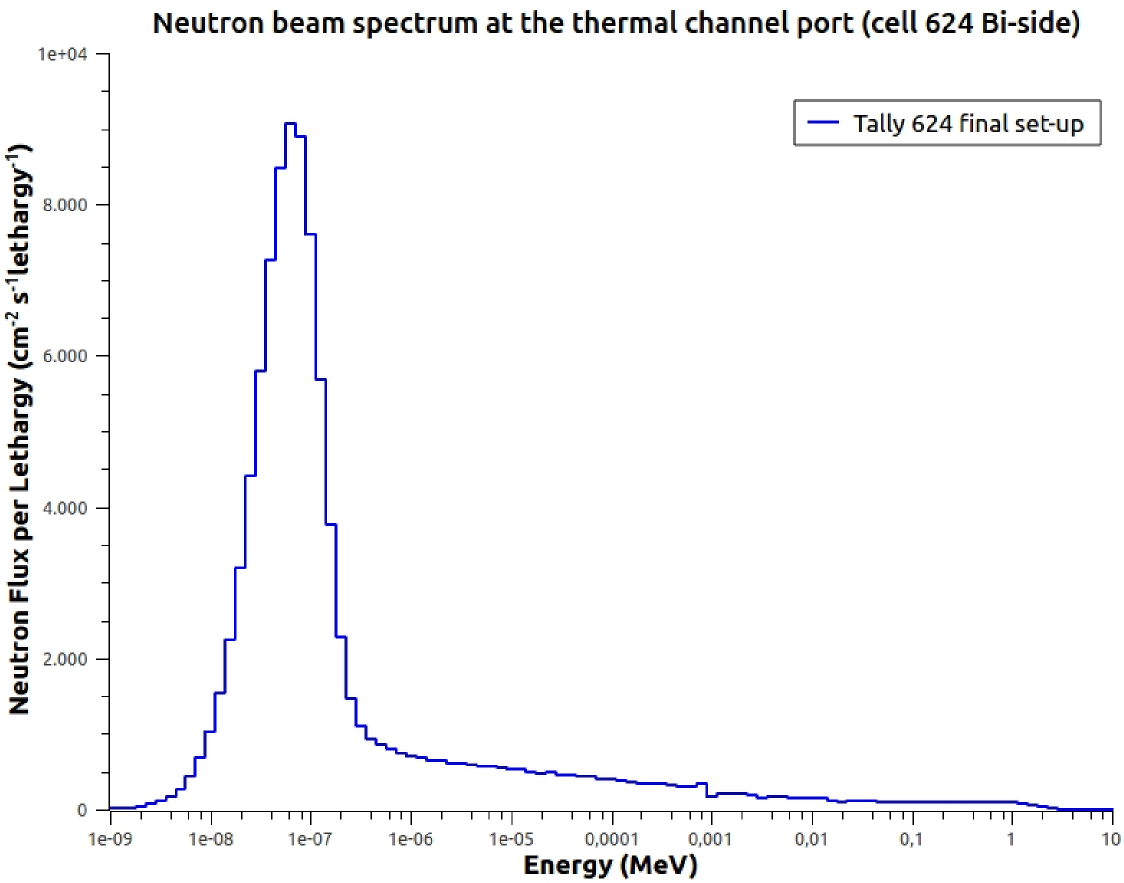

Figure 3.9: Spectrum of neutrons emerging in the sideward direction with the final set-up with teflon, graphite and bismuth. Neutron flux Tally in cell 624.

In general, a good neutrons beam is characterized by a low gamma component because it is a source of non-selective background dose delivered to the target, so, in addition to the parameter ($\dot{D}_\gamma/ThermalFlux$), the γ-rays spectrum has been evaluated at the thermal neutrons beam port (tally cell 624). The spectrum shows the characteristic peaks of the materials used as moderator present in the set-up (Fig. 3.10), we can recognize:

- Hydrogen (lithiated polyethylene) at 2223 eV;
- Carbon (graphite and graphite) at 2881 and 4945 eV;
- Fluorine (teflon) at 580 eV, and 660 eV;
- Bismuth at 4054 eV and 4171 eV.

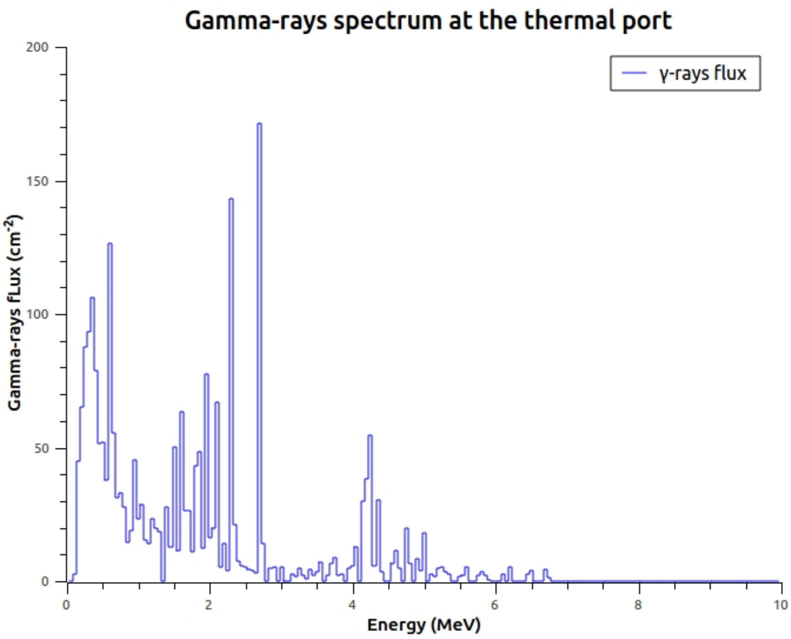

Figure 3.10: Gamma-rays spectrum at the sideward direction with the final set-up with teflon, graphite and bismuth. Photons flux Tally in cell 624.

Chapter 4

Tailoring of an epithermal neutron beam

This chapter is dedicated to the optimization of the epithermal neutron irradiation port. The beam should have the same characteristics required for a clinical BNCT beam dedicated to the treatment of deep-seated tumors, without damaging the shallow tissues. The spectrum of neutrons should be epithermal with low thermal, fast and gamma contaminations. Different set-ups and materials have been used as moderator to obtain a suitable epithermal neutron beam. In particular, it has been demonstrated that a suitable epithermal neutron beam to treat pulmonary tumours has a peak towards 1 keV, slightly lower than the traditional 10 keV beams employed for brain tumours [35].
IAEA has provided some guidelines to evaluate the suitability of an epithermal neutron beam employed for clinical BNCT. The requirements to be fulfilled are indicated in Table 4.1 [34].

Table 4.1: IAEA's recommendations on beam quality.

Beam parameter	IAEA guidelines values
Beam intensity	$10^9\ (cm^{-2}s^{-1})$
$\dot{D}_{fast}/\phi_{epi}$	$2.5 \cdot 10^{-13}\ (Gy\ cm^{-2})$
$\dot{D}_{\gamma}/\phi_{epi}$	$2.0 \cdot 10^{-13}\ (Gy\ cm^{-2})$

4.1 Epithermal Neutron Filter

As mentioned in Section 1.1 the epithermal neutrons energies range is from 0.5 eV to 10 keV. Tailoring a good moderator for an epithermal neutrons beam is more complex than the case of a thermal one due to the presence of resonances in the cross sections of the materials in the energy range between 10 keV and 5 MeV. The neutron filter/moderator should have a high scattering cross section in the high energy range (fast neutrons) and low scattering cross section for the epithermal neutrons [36]. The adopted approach consisted in simulating different sequences of layers, assembled to exploit the overlapping resonances of the selected materials. This also allows for an easy beam shaping assembly construction because the layers are thin and handling (Appendix A). Most of the fast neutrons are moderated to epithermal and thermal energies as they scatter through the plates of different materials. Thermal neutrons are not desired at the exit port: a material that absorbs thermal neutrons is also required in the filter. Effective shaping materials for epithermal neutron beams, capable of reducing the fast component without removing neutrons in the energy range of interest are:

Fluental$^{\mathbf{TM}}$ is a patented material (i.e. metal and ceramic) for neutron moderation. It consists of a mixture of aluminium, aluminium fluoride and lithium fluoride (Appendix B.8). It is used as moderator in some BNCT facilities and this material turned out to be an excellent fast neutrons filter for accelerator-based neutron sources, its high density allows the realization of compact devices. It was developed in Finland. Its main drawback is the expensive price due to the patent.

Aluminium, fluorine, magnesium and silicon compounds are interesting materials due to their resonances above 10 keV. Al and AlF_3 are the most common moderator materials in beam-shaping assemblies for accelerator-based BNCT. However, their low density compared to Fluental$^{\mathrm{TM}}$ is one of their main drawbacks- relatively thick Al and AlF_3, are required for the same neutron attenuation. Furthermore it is difficult, for some compounds such as AlF_3 and MgF_2, to achieve an homogeneous, proof and wieldy material. On the other hand, alluminated materials are cheaper than the Fluental$^{\mathrm{TM}}$. The aluminium- teflon combination produces good beam characteristics and it is easily available. Teflon, which has a significantly resistance to radiation damage, is inexpensive, readily avaible and chemically stable.

Titanium shows a large resonance at 10 keV and a $1/v$ behaviour at low energies (Appendix A.12). It has been suggested as a good chopper for upper epithermal energies range. Its drawback is a strong γ-rays emission due to the thermal neutrons absorption so it is necessary to remove the gamma contamination adding a thermal neutrons absorber and/or a lead shield.

Lithium and compounds are the best thermal neutron absorbers because no γ-rays are released in the process (neutron capture in ^6Li). The high thermal absorption cross section of the ^6Li isotope (Appendix A.2), helps to remove thermal neutrons from clinical neutron beams. The result is lower thermal neutrons and gamma contamination due to thermal neutron absorption. The drawback associated to the use of lithium is that the neutron capture occurs in ^6Li, that is only 7.5% in natural lithium. Materials as lithium carbonate or lithium fluoride are very expensive if high enrichments in ^6Li are required. On the other hand, using natural lithium implies higher thicknesses that sometimes may be a problem (i.e. at the beam port, for penumbra effects). Another strategy to remove thermal component is to use boronated materials, with the same problem connected to enrichment (10B is 20% of natural abundance) and with the creation of a gamma ray of 487 keV.

4.2 Water Tank

The optimization work started from the evaluation of a possible epithermal facility exploiting the existing set-up, comprising the heavy water tank. The tallies calculated are the same described in the previous chapter, and the results are reported in Table 4.2.

Table 4.2: Neutron flux for the three energy ranges calculated at the three positions. Set-up characterized by the heavy water tank.

Energy Range	Tally 525 Neutron Flux ($cm^{-2}s^{-1}$)	Tally 624 Neutron Flux ($cm^{-2}s^{-1}$)	Tally 724 Neutron Flux ($cm^{-2}s^{-1}$)
0 eV < E < 0.5 eV	$2.08 \cdot 10^5$	$1.14 \cdot 10^5$	$1.14 \cdot 10^5$
0.5 eV < E < 10 keV	$3.51 \cdot 10^4$	$5.12 \cdot 10^3$	$5.12 \cdot 10^3$
E > 10 keV	$5.82 \cdot 10^3$	$1.12 \cdot 10^2$	$1.12 \cdot 10^2$
Total Flux	$2.5 \cdot 10^5$	$1.21 \cdot 10^5$	$1.21 \cdot 10^5$
$\frac{\phi_{epi}}{\phi_{tot}}$	14%	4%	4%

As the double differential spectra measured (see Section 2.4) showed the highest intensity of neutrons in the forward direction, the aim was to degrade the energy of these neutrons down to the range of interest. The results of these preliminary calculations, however, show that the epithermal neutron flux is too low due to the high thermalization power of heavy water. Fig. 4.1 displays the distribution of the epithermal neutron flux superimposed to the geometry of the existing set-up.

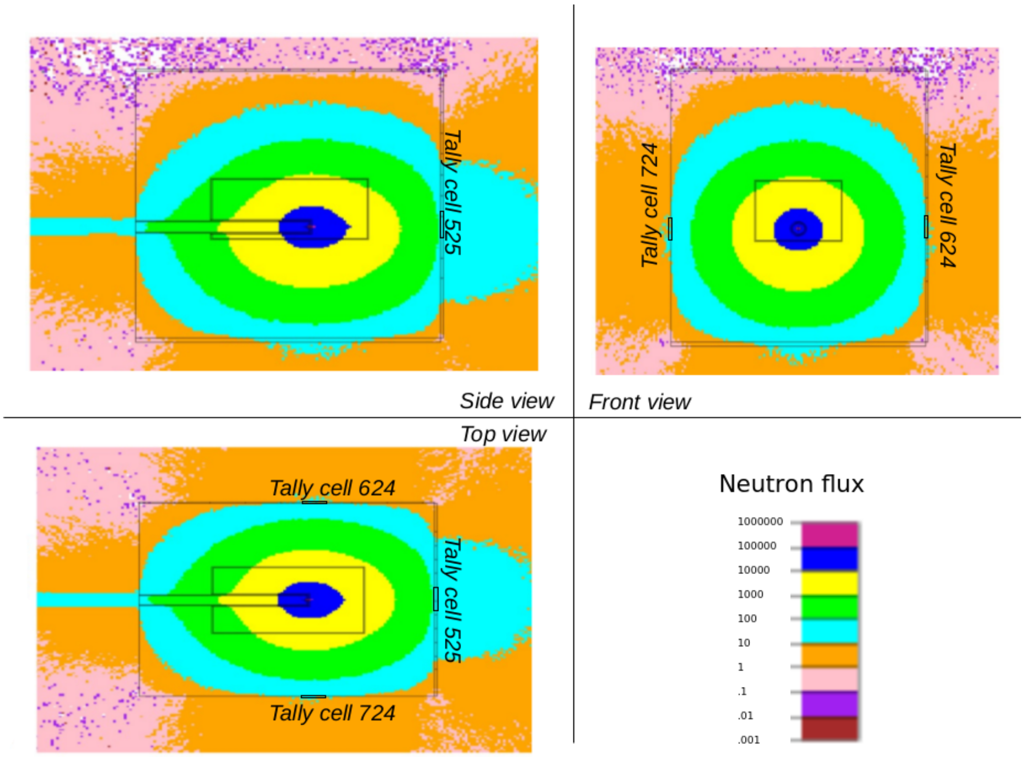

Figure 4.1: Distribution of epithermal neutron flux in the existing set-up (with heavy water tank) superimposed to the planes perpendicular to the neutron source. Results were obtained with mesh tallies calculation.

Also the rotated heavy water tank set-up has not resulted in a satisfactory outcome for the epithermal neutrons flux intensity (Fig. 4.2). the neutron spectrum in Fig.4.3 shows that the neutron flux is centered at 0.07 eV. The statistical error for each bin is lower than 7.5%.

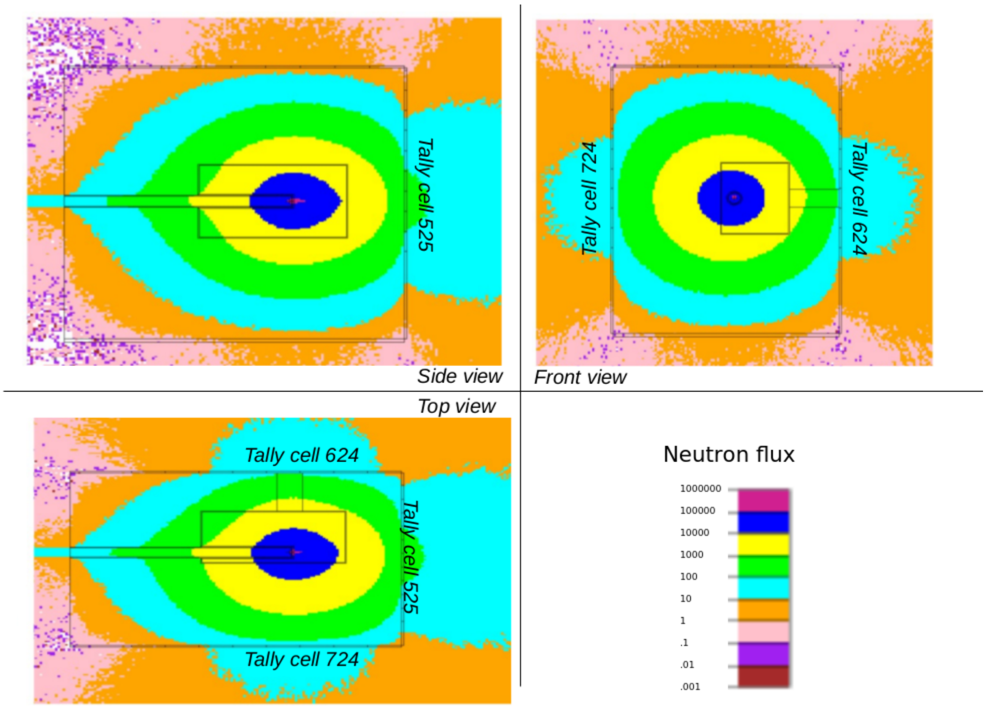

Figure 4.2: Distribution of epithermal neutron flux in the set-up with rotated heavy water tank, superimposed to the planes perpendicular to the neutron source. Results were obtained with mesh tallies calculation.

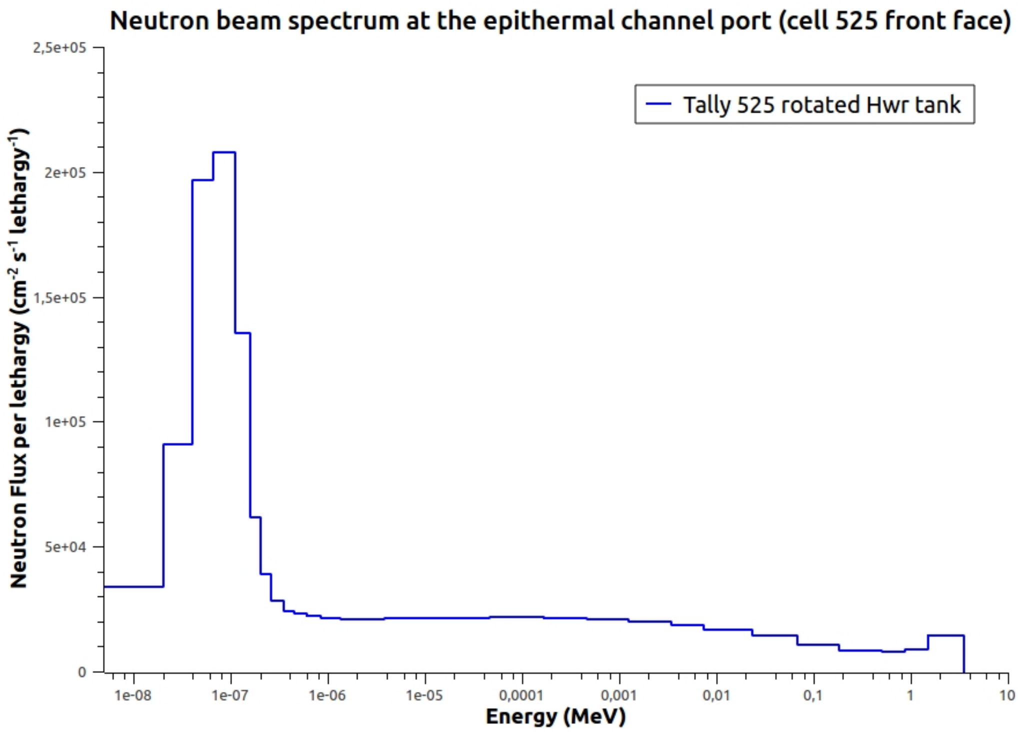

Figure 4.3: Spectrum of neutrons emerging in the forward direction (cell 525) with the set-up characterized by the rotated heavy water tank. Neutron flux Tally in cell 525.

4.3 Replacing the Water Tank with Graphite

At this step the heavy water tank, which worked well on the thermal irradiation position, was discarded and replaced by graphite. This choice allowed a higher freedom because the thickness of graphite or other materials could be modulated according to the required spectral characteristics. The geometry configuration of this set-up is shown in Fig. 4.4.

The results of this simulation are reported in Tab. 4.3 and in Fig. 4.5 and they were assumed as the starting point for the further optimization of the epithermal beam. In fact in this case the epithermal component is the most intense, even if a further tailoring is necessary. In particular the thermal and fast component must be strongly suppressed. The statistical error for each bin is lower than 6.9%. From now on, the neutron flux corresponds to the maximum proton current available at CN accelerator: 3 μA.

Table 4.3: Neutron flux in the three energy rages plus total neutron flux in the forward direction (cell 525), when the heavy water has been replaced with graphite.

Energy Range	Tally 525 Neutron Flux ($cm^{-2}s^{-1}$)
0 eV < E < 0.5 eV	$6.04 \cdot 10^5$
0.5 eV < E < 10 keV	$2.07 \cdot 10^6$
E > 10 keV	$9.3 \cdot 10^5$
Total Flux	$3.5 \cdot 10^6$
$\frac{\phi_{epi}}{\phi_{tot}}$	59%

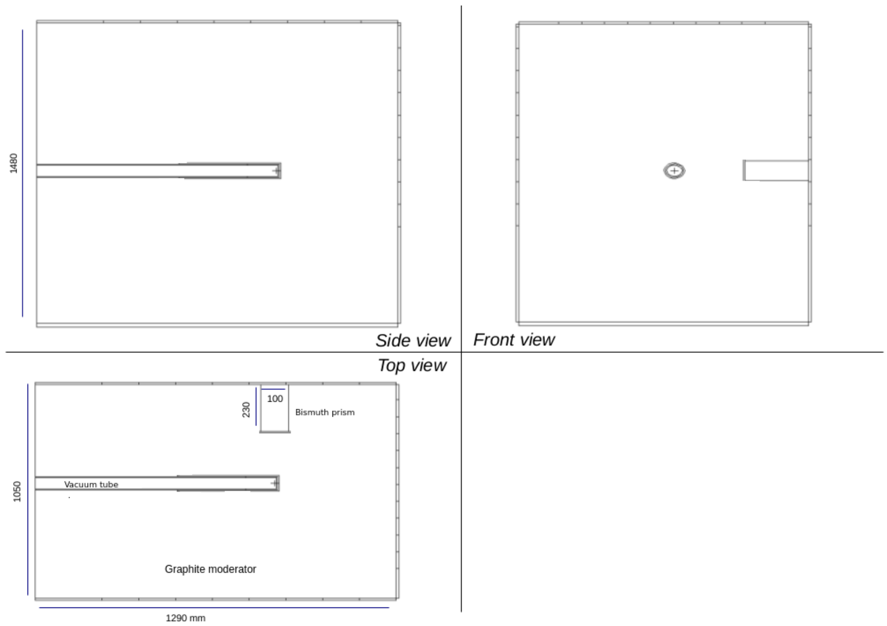

Figure 4.4: Geometries of replaced heavy water tank with graphite block set-up.

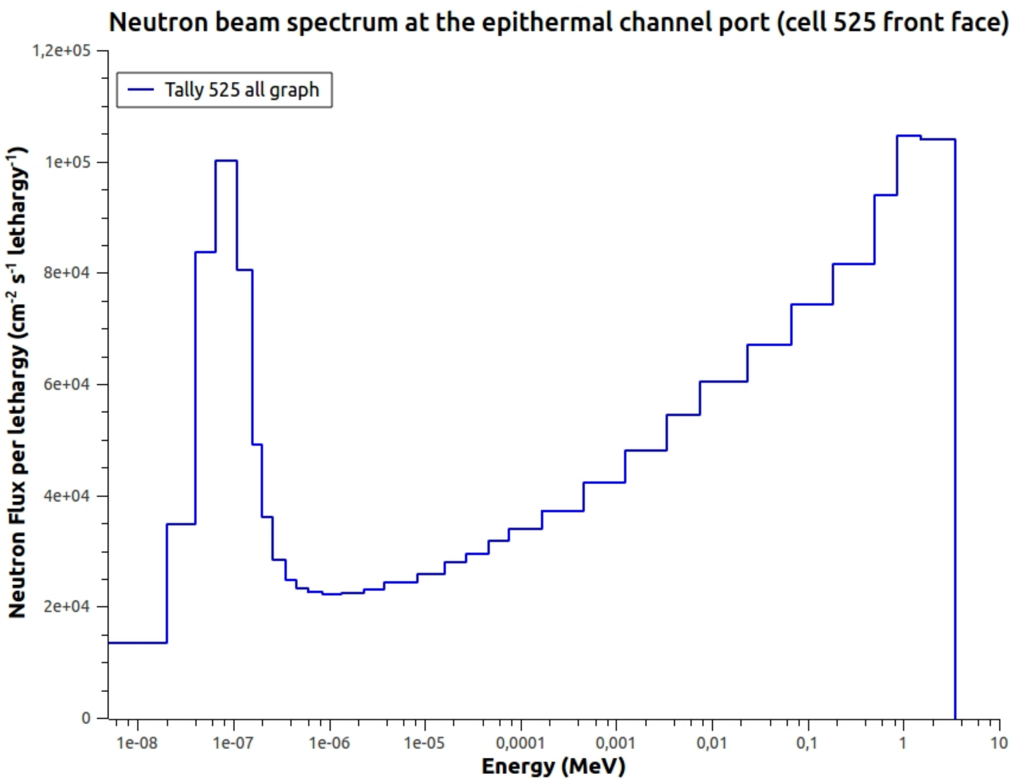

Figure 4.5: Spectrum of neutrons emerging in the forward direction (cell 525) with the set-up characterized when the heavy water has been replaced with graphite. Neutron flux Tally in cell 525.

4.4 Shaping the Epithermal Beam

To improve the epithermal neutrons flux intensity a channel has been obtained into the graphite moderator, replacing a graphite slab with air along the forward direction maintaining the tally cell 525 in the same position (Fig. 4.6). Two solutions have been considered with different channel width: channel A (Fig. 4.6a) and channel B (Fig. 4.6b). The dimensions of channel A are: length 210 mm, thickness 75 mm and height 75 mm (Fig. 4.6a). The dimensions of channel B are: length 210 mm, thickness 225 mm and height 225 mm (Fig. 4.6b).

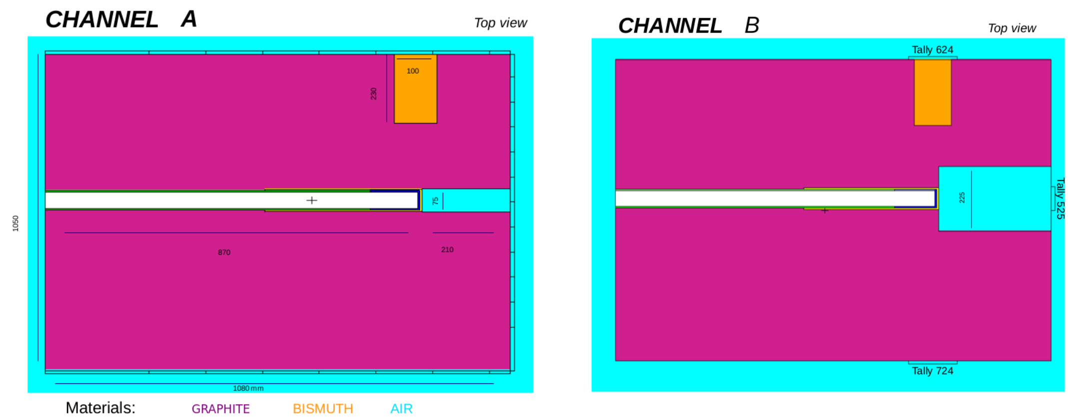

(a) Channel A set-up.

(b) Channel B set-up.

Figure 4.6: Geometries of two different channel solutions: channel A and channel B set-ups. Where a channel has been obtained into the graphite moderator replacing a graphite slab with air along the forward direction.

Fig. 4.7 shows the neutron spectra in the forward direction (cell 545) with the open and the triple open channel. In both cases the flux intensity above the epithermal energies has increased. It is particularly considerable the channel B case, where the increase of the flux is higher than the single case on the whole energies range interest, thus this second configuration has been selected for a further shaping of the spectrum. The statistical error for each bin is lower than 6.2%.

The second step was to slow down the fast component to the epithermal range reducing the fast contamination as much as possible.

As third step air could be replaced by Fluental^{TM}, but this material is too expensive. The Fluental^{TM}composition has been thus reproduced with a series of Aluminium and LiF layers, called sandwich filter/moderator [19, 22, 30]. The thickness of each layer is 10 mm. Moreover, two blocks of graphite and teflon have been placed between the vacuum tube and the sandwich filter for a first slow down of fast neutrons (Fig. 4.8). LiF was chosen because it is often used in the design of an epithermal neutron beam but it is difficult to realize a high density and homogeneous layer of this material, and when it is possible to purchase it, its cost is prohibitive. Therefore, the next step has been replacing LiF with teflon.

The outcomes obtained by the Al and LiF sandwich are reported in Fig. 4.9, showing a low thermal neutron contamination (due to neutron capture in lithium) and the reduction of the fast component of the spectrum. The flux has low thermal neutrons contamination and the maximum at high energies has been reduced (green line in Fig. 4.9). The result obtained by replacing LiF with teflon is positive (red and blue lines in Fig. 4.9) in the epithermal energies range, unfortunatly it shows a maximum at 0.05 eV, but this can be easly solved by adding a layer of thermal neutrons absorber, such as Li_2CO_3 (Appendix B.1). The statistical error for each bin is lower than 7.2%.

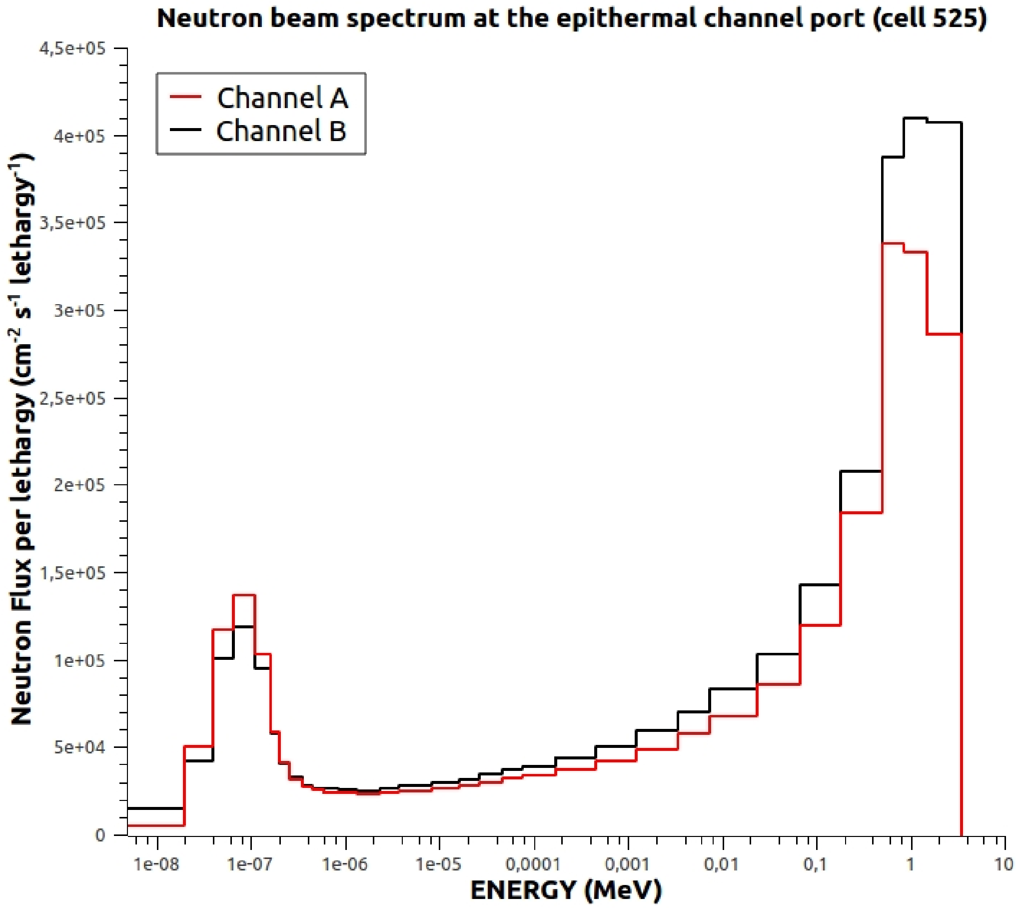

Figure 4.7: Spectra of neutrons emerging in the forward direction (cell 525) with channel A (red line) and channel B (black line)set-ups characterized with different width. Neutron flux Tally in cell 525.

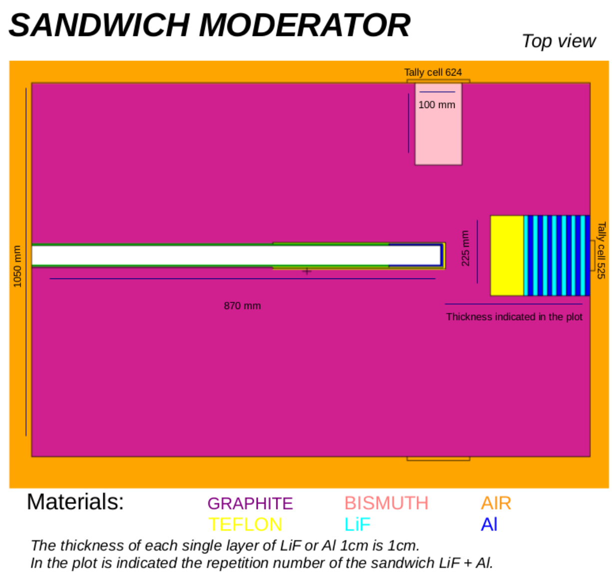

Figure 4.8: Channel B solution with sandwich moderator set-up.

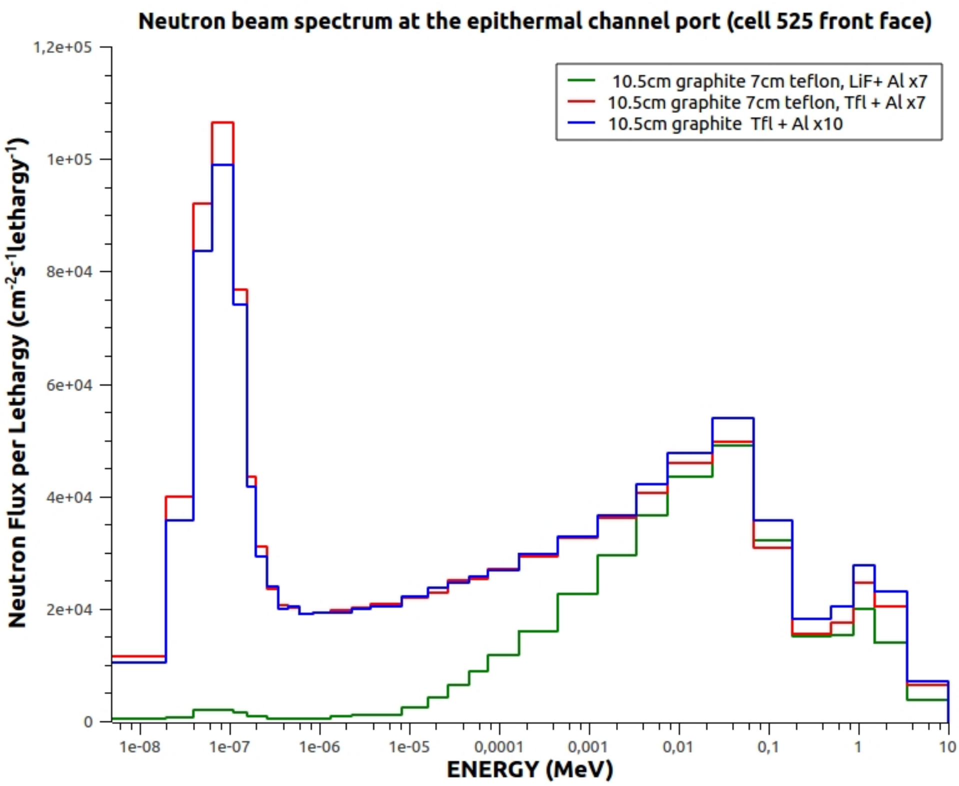

Figure 4.9: Neutron spectrum of neutrons in the forward direction (cell 525) with the triple open channel and the sandwich moderator in the three cases of:105 mm of graphite, 70 mm of teflon and 7x(10 mm teflon / 10 mm aluminium)(red line), 105 mm of graphite and 10x(10 mm teflon / 10 mm aluminium)(blue line) and 105 mm of graphite, 70 mm of teflon and 7x(10 mm LiF / 10 mm aluminium) (green line).

4.5 Titanium Filter

The results obtained in the previus with Teflon and Al satisfactory, but the flux has still an intense component between 10 and 100 keV, while the optimal range goes from 0.5 eV to 10 keV. Therefore it has been required a material wich is able to cut the neutrons flux above 10 keV. Different materials have been analized and only the titanium shows a large resonance in the scattering cross section of about 100 barns between 10 keV and 40 keV (Appendix A.12). A single layer of titanium has been added at the end of the sandwich filter (Fig. 4.10).

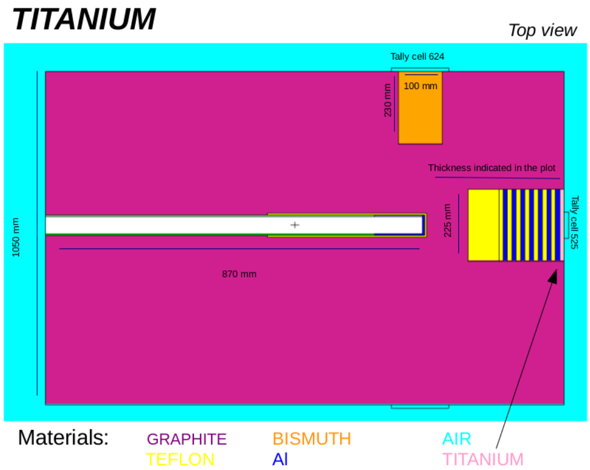

Figure 4.10: Geometries of titanium layer set-up.

This Ti layer had a remarkable effect in the fast range (blue line in Fig.4.11). This pushed to test another configuration where all the Al layers were replaced with Ti (green line Fig.4.11). The result was a decrease of the flux in the desired range, however, the fast contamination above 100 keV is still too high. The statistical. Still, the fast contamination above 100 keV is too high. The statistical error for each bin is lower than 7.3%.

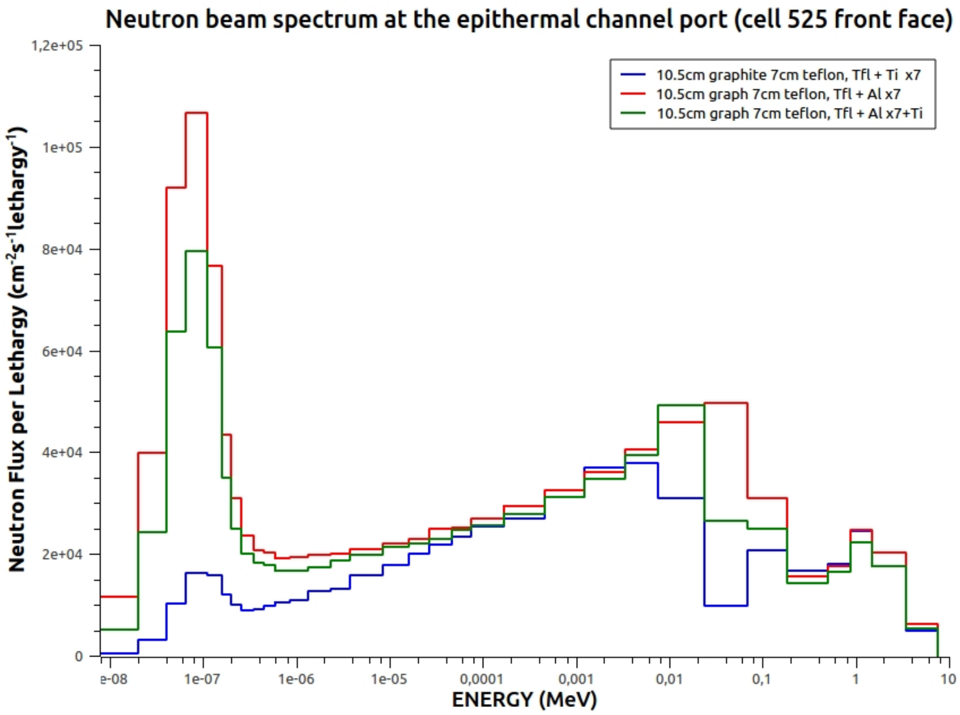

Figure 4.11: Neutron spectrum of neutrons in the forward direction (cell 525) with the channel B configuration and the sandwich moderator in the three cases of: 105 mm of graphite, 70 mm of teflon and 7x(10 mm teflon / 10 mm aluminium)(red line), 105 mm of graphite and 10x(10 mm teflon / 10 mm titanium)(blue line) and 105 mm of graphite, 70 mm of teflon, 7x(10 mm teflon / 10 mm titanium), and 10 mm of titanium (green line).

4.6 Epithermal Channel at 60, 90 and 120 Degrees

In order to reduce the fast neutrons, the beam port has been rotated at 60^o, 90^o and 120^o degrees keeping the same materials assembly of the last described set up: 105 mm graphite, 70 mm teflon and 140 mm teflon/titanium sandwich (Fig. 4.12 and Fig. 4.13). The rationale of this choice is that in the Be(p,n) reaction the fast neutrons emission shows a maximum along the forward direction (Chapter 2.2), so the aim is finding the best compromise between flux intensity and fast contamination at different angles.

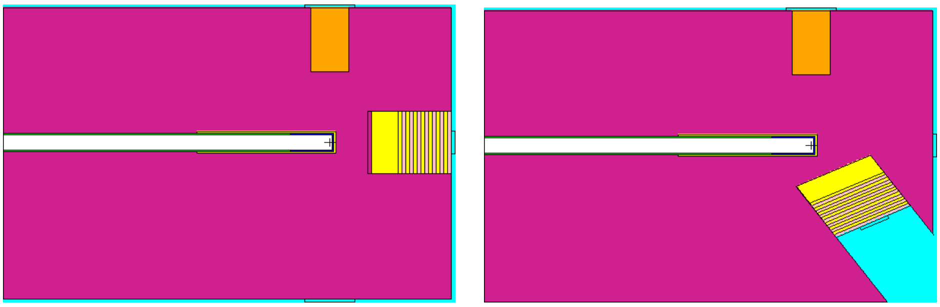

(a) 0^o degrees channel set-up. **(b)** 60^o degrees channel set-up.

Figure 4.12: 0^o and 60^o degrees channel set-up.

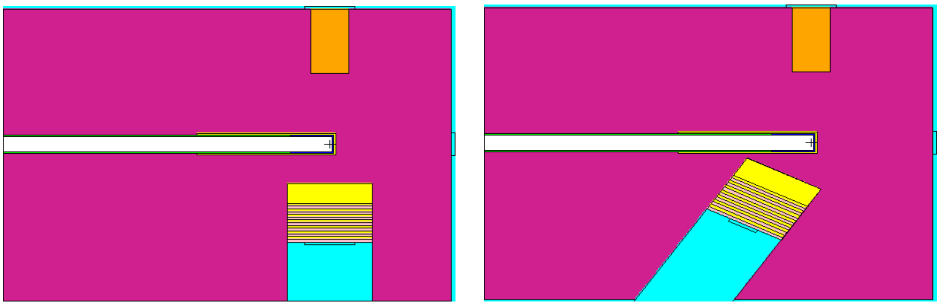

(a) 90^o degrees channel set-up. **(b)** 120^o degrees channel set-up.

Figure 4.13: 90^o and 120^o degrees channel set-up.

The results show that at 90^o and 120^o the neutrons flux have a lower fast neutrons contamination than in the forward direction (Fig. 4.14). The higher neutrons thermal component in the beams at angles different than 0^o is due to the graphite which surrounds the empty bottom of the channel.

The solution at 90^o has been chosen instead of the 120^o for its easier implementation.

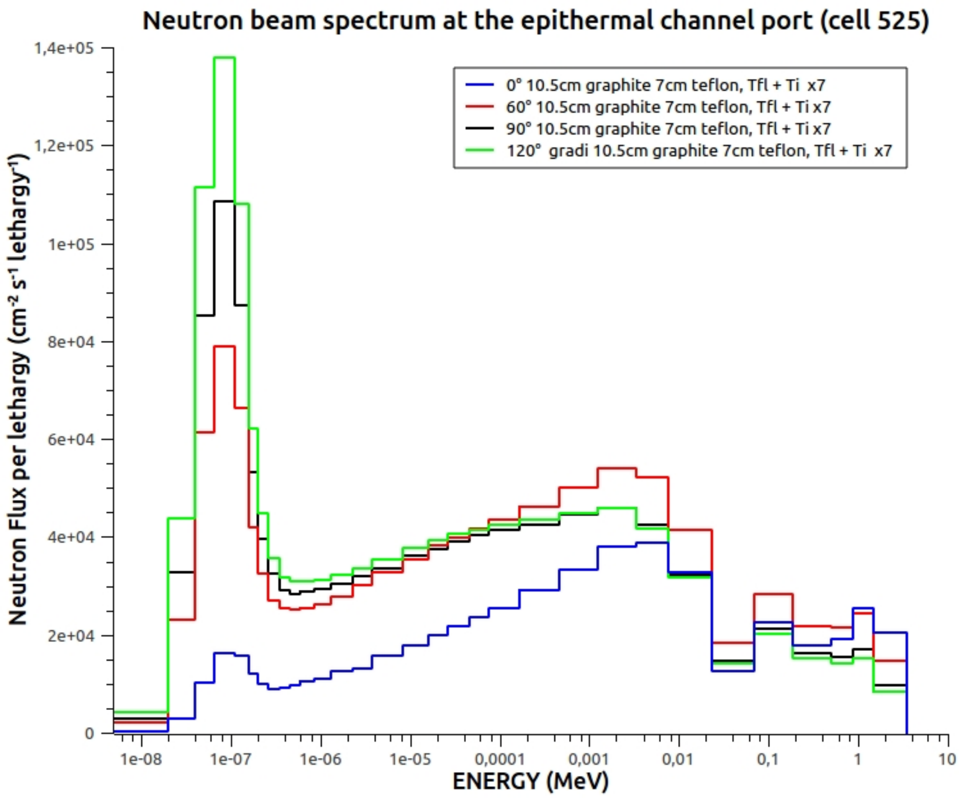

Figure 4.14: Neutron spectrum of neutrons at different angles with the triple open channel and the sandwich moderator (105 mm of graphite, 70 mm of teflon and 7x(10 mm teflon / 10 mm titanium)): 0^o (blue line), 60^o (red line), 90^o (black line), and 120^o (green line).

4.7 Optimization of the 90^o Channel Solution

As first the channel was shortened removing graphite excess for decreasing the thermal component. The beam at 90^o was further optimized by testing different materials to better filter the unwanted components: lithium fluoride, teflon, graphite, magnesium fluoride, magnesium alloy, silicium, calcium fluoride, titanium, aluminium fluoride, lithium carbonate, iron and lead.
Moreover, the sequence and the thickness of the sandwiches were modified according to these schemes:

All sandwich set-up 15x(10 mm titanium / 10 mm aluminium / 10 mm teflon), and 2X(10 mm titanium / 10 mm aluminium) (Fig. 4.15a).

Teflon and sandwich channel set-up 180 mm of teflon, 8x(10 mm titanium / 10 mm aluminium / 10 mm teflon), and 35 mm of Li_2CO_3 (Fig 4.16a).

Clad channel and lead filter set-up 200 mm of teflon, 8x(10 mm titanium / 5 mm teflon / 15 mm aluminium), 30 mm of lead, and 20 mm of Li_2CO_3, cladded by 10 mm of Li_2CO_3 (Fig. 4.17a).

Thermal shield channel set-up 200 mm of teflon, and 5x(10 mm titanium / 5 mm teflon / 15 mm magnesium alloy / 5 mm teflon / 15 mm aluminium), cladded by 40 mm of Li_2CO_3 (Fig.4.18a).

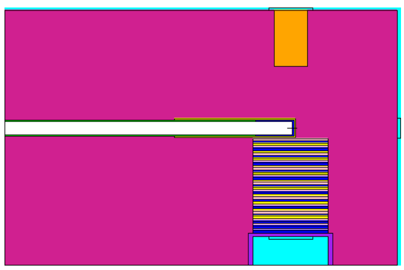

(a) All sandwich channel set-up.

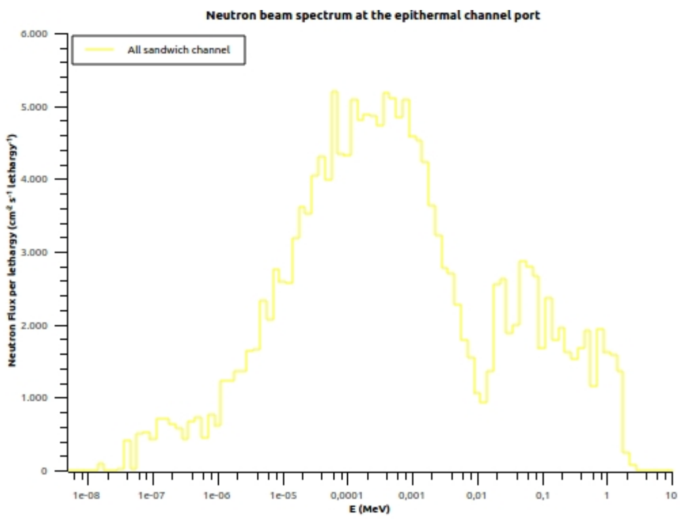

(b) Spectra of neutrons emerging in the sideward direction (cell 724) with all sandwich channel set-up.

Figure 4.15: Geometry configuration and spectrum of neutrons emerging in the sideward direction (cell 724) with all sandwich channel set-up.

An initial series of simulation was performed with the epithermal channel completely filled by the sandwich (Fig. 4.15a), but the contamination of fast neutrons is too high and epithermal flux is too low (Fig. 4.15b). The fast neutrons contamination was lowered including a teflon block before the sandwich and a lead filter after the sandwich, wich shields the γ-rays emissions (Fig. 4.16a). The epithermal intensity is still too low for our purposes (Fig. 4.16b). To increase the epithermal flux without exceeding in gamma contamination produced by radiative neutron capture in titanium and aluminium layers, the channel was cladded by a lithium carbonate film, wich is a good thermal neutron absorber (Fig. 4.17).

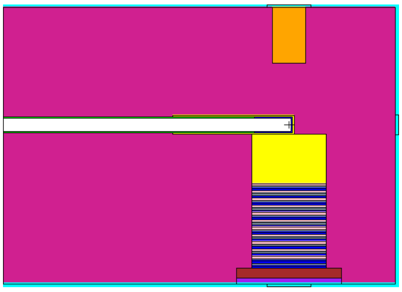

(a) Teflon and sandwich channel set-up.

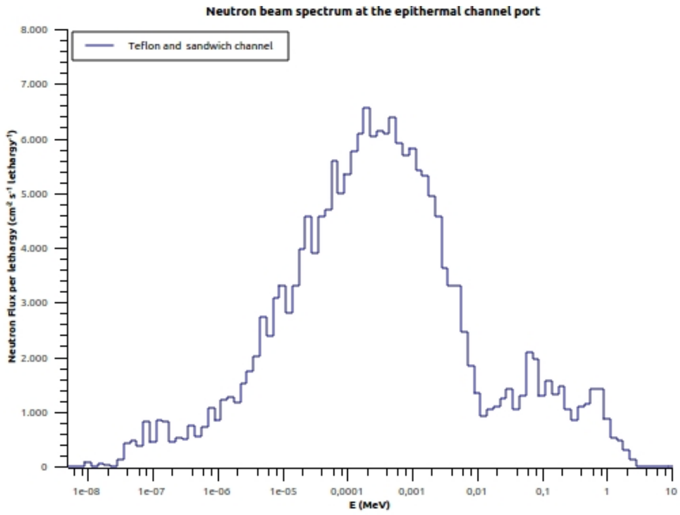

(b) Spectra of neutrons emerging in the sideward direction (cell 724) with teflon and sandwich channel set-up.

Figure 4.16: Geometry configuration and spectrum of neutrons emerging in the sideward direction (cell 724) with teflon and sandwich set-up.

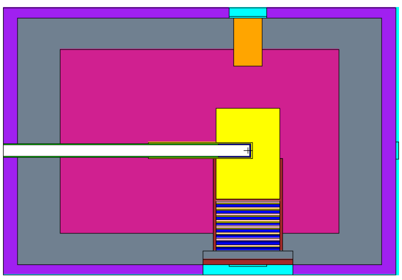

(a) Clad channel and lead filter set-up.

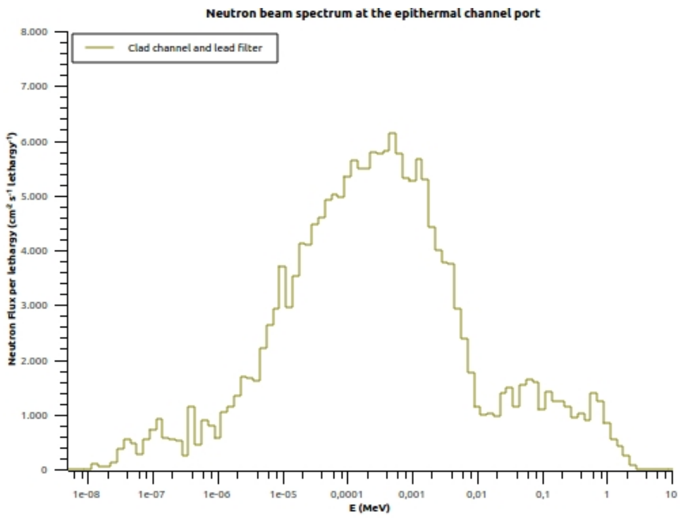

(b) Spectra of neutrons emerging in the sideward direction (cell 724) with clad channel and lead filter set-up.

Figure 4.17: Geometry configuration and spectrum of neutrons emerging in the sideward direction (cell 724) with clad channel and lead filter set-up.

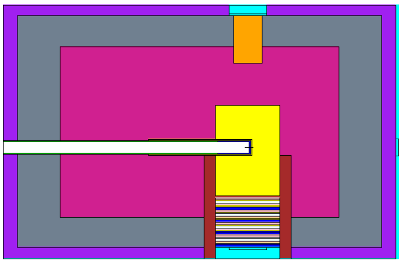

(a) Thermal shield channel set-up.

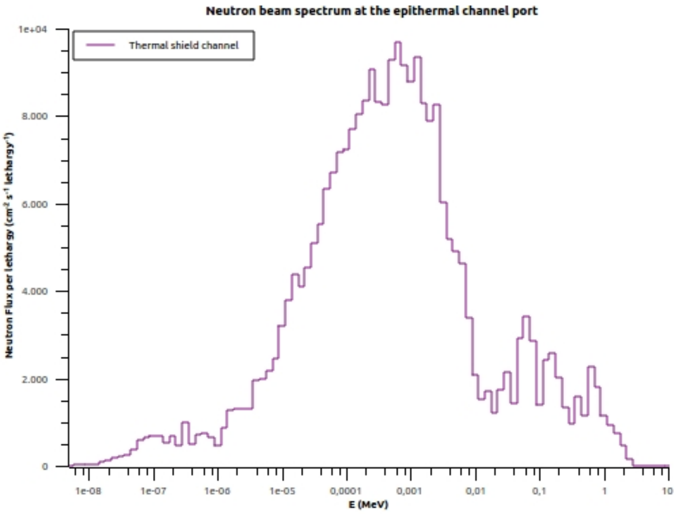

(b) Spectra of neutrons emerging in the sideward direction (cell 724) with thermal shield channel set-up.

Figure 4.18: Geometry configuration and spectrum of neutrons emerging in the sideward direction (cell 724) with thermal shield channel set-up.

The best solution was obtained with a first teflon block which decreases the high fast neutron flux, then a sanwich of different thicknesses of magnesium alloy, teflon, aluminium, and titatium as a fine filter moderator lowering the fast dose contamination (Fig. 4.18 and Fig. 4.19). In Table 4.4 neutron fluxes are reported

Table 4.4: Comparison of the neutron fluxes obtained with the configurations shown in Fig. 4.15, Fig. 4.16, Fig. 4.17, and Fig. 4.18: all sandwich channel, teflon and sandwich cannel, clad channel and lead filter, and thermal shield channel. The highest neutron flux in the range of interest is obtained with the thermal shield set-up.

Set-up	ϕ_{therm}	ϕ_{epi}	ϕ_{fast}
	$(cm^{-2}s^{-1})$	$(cm^{-2}s^{-1})$	$(cm^{-2}s^{-1})$
All sandwich	$1.47 \cdot 10^3$	$9.57 \cdot 10^4$	$6.37 \cdot 10^4$
Teflon and sandwich	$3.4 \cdot 10^3$	$1.19 \cdot 10^5$	$3.04 \cdot 10^4$
Clad channel and lead	$1.97 \cdot 10^3$	$1.13 \cdot 10^5$	$3.72 \cdot 10^4$
Thermal shield	$2.78 \cdot 10^3$	$3.01 \cdot 10^5$	$5.86 \cdot 10^4$

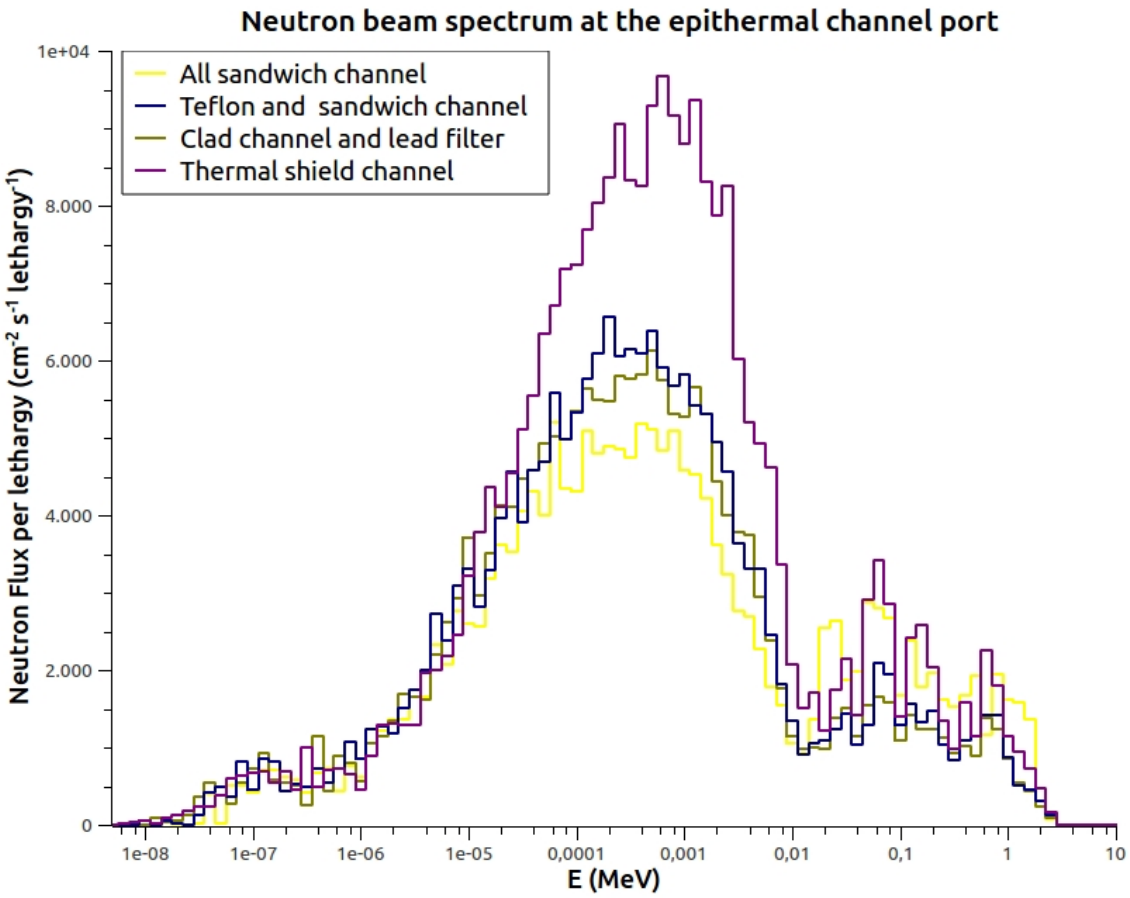

Figure 4.19: Comparison of the neutron spectra obtained with the configurations shown in Fig. 4.15, Fig. 4.16, Fig. 4.17, and Fig. 4.18: all sandwich channel (yellow line), teflon and sandwich cannel (blue line), clad channel and lead filter (brown line), and thermal shield channel (violet line). The highest neutron flux in the range of interest is obtained with the thermal shield set-up.

4.8 Final set-up

By looking at the responses within the epithermal region, the best configuration of the channel is: 200 mm teflon, 10 mm magnesium alloy, 5 mm teflon, 10 mm magnesium alloy, 5x(10 mm aluminium / 5 mm teflon / 15 mm magnesium alloy), 5 mm teflon, 2x(5 mm magnesium alloy / 5 mm aluminium), 2x(5 mm magnesium alloy / 5 mm titanium), and 5 mm magnesium alloy; for a total thickness of 420 mm (Fig. 4.20 and Fig. 4.21).

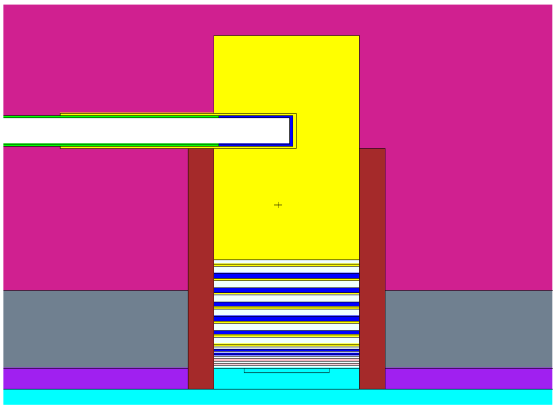

Figure 4.20: Final set-up, this figure focuses on the epithermal neutron beam port, composed of: 200 mm teflon, 10 mm magnesium alloy, 5 mm teflon, 10 mm magnesium alloy, 5x(10 mm aluminium / 5 mm teflon / 15 mm magnesium alloy), 5 mm teflon, 2x(5 mm magnesium alloy / 5 mm aluminium), 2x(5 mm magnesium alloy / 5 mm titanium), and 5 mm magnesium alloy.

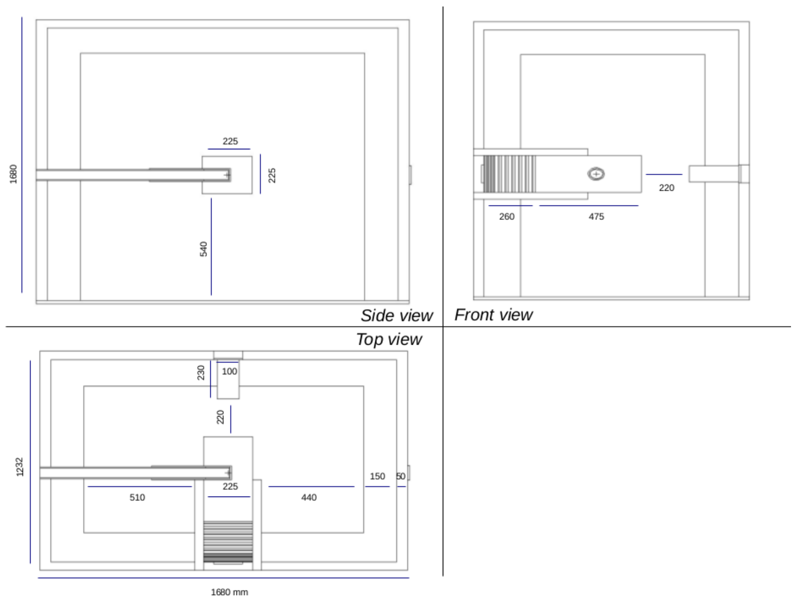

Figure 4.21: Final set-up, the epithermal neutron beam port is on the left in the fron view and on the bottom of the top view. These figures show also the thermal beam port that was described in the previous Chapter 3.

The results obtained comply with the requirements for a suitable BNCT neutron beam: the neutron flux shows a maximum between 1 keV and 10 keV, and it rapidly decreases above 15 keV (Fig. 4.23). If the current would be 30 mA, as achieved by the RFQ accelerator, this BSA would provide an epithermal neutron flux of $2.2 \cdot 10^9$ ($cm^{-2}s^{-1}$), that would allow for short treatment times in according to IAEA's guidelines (Table 4.5). The ratio of the gamma dose and the epithermal neutron flux ($\dot{D}_\gamma/EpithermalFlux$), the ratio of the dose due to fast neutrons and the epithermal neutron flux ($\dot{D}_{fast}/EpithermalFlux$) and the ratio of the dose due to thermal neutrons are reported in Table 4.5. These three beam quality parameters derived from the BSA design are satisfactory for the gamma and thermal contaminations, while the fast neutrons dose ratio is higher than IAEA's recommendation. However, it should be noted that the obtained value lies in the range of the contamination present in some reactor-based facilities already employed for clinical BNCT (Table 4.6).

Table 4.5: Neutron flux in the three energy ranges of interest, total neutron flux and beam quality parameters obtained with the final set-up shown in Fig. 4.20 and Fig. 4.21 , compared with IAEA recommendations.

Energy Range	Tally 724 Neutron Flux ($cm^{-2}s^{-1}$)	IAEA guidelines values
0 eV < E < 0.5 eV	$1.51 \cdot 10^3$	
0.5 eV < E < 10 keV	$2.2 \cdot 10^5$	10^9
E > 10 keV	$3.4 \cdot 10^4$	
Total Flux	$2.6 \cdot 10^5$	
$\frac{EpithermalFlux}{TotalFlux}$	84%	
$\frac{\dot{D}_{thermal}}{EpithermalFlux}$	$1.1 \cdot 10^{-15}$	$2.5 \cdot 10^{-13}$
$\frac{\dot{D}_{fast}}{EpithermalFlux}$	$8.7 \cdot 10^{-13}$	$2.5 \cdot 10^{-13}$
$\frac{\dot{D}_\gamma}{EpithermalFlux}$	$2.4 \cdot 10^{-13}$	$2.0 \cdot 10^{-13}$

Table 4.6: In air beam quality parameters derived from the accelerator-based facility and some examples of measured in-air parameters for epithermal facilities.

Neutron source	ϕ_{epi} ($10^{-9} cm^{-2}s^{-1}$)	$\frac{\dot{D}_{fast}}{\phi_{epi}}$ ($10^{-13} Gy\ cm^{-2}s^{-1}$)	$\frac{\dot{D}_\gamma}{\phi_{epi}}$ ($10^{-13} Gy\ cm^{-2}s^{-1}$)
FCB [37] (5 MW)	4.3	1.4	3.6
JRR-4 (3.5 MW) [38]	2.2	3.1	1.5
THOR (1.2 MW) [16,39]	1.1	3.4	1.3
Fir (0.25 MW) [40,41]	1.1	2.1	0.5
KURR (5 MW) [42]	0.46	6.2	2.8
HFR (45 MW) [43]	0.33	12.1	3.8
Li ABNS 30 mA [22]	0.95	5.2	4.9
Be ABNS 30 mA	**2.2**	**8.7**	**2.4**

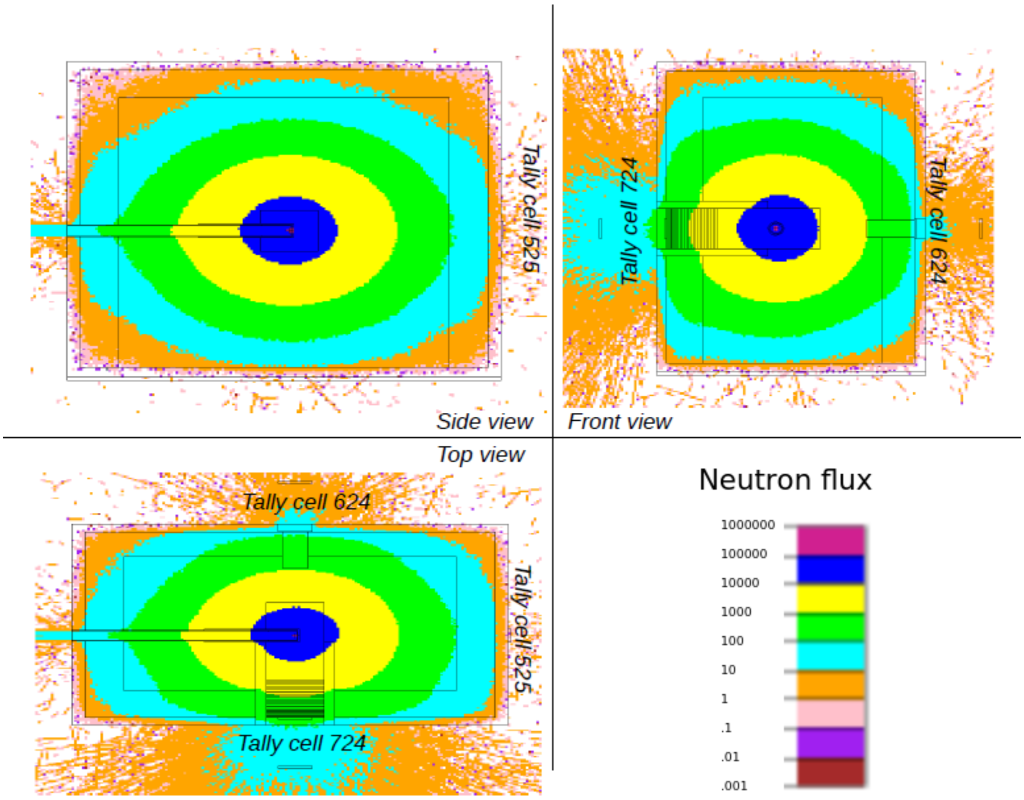

Figure 4.22: Epithermal neutron flux distribution obtained with the final set-up in three planes perpendicular to the neutron source. Values obtained by mesh tally calculations.

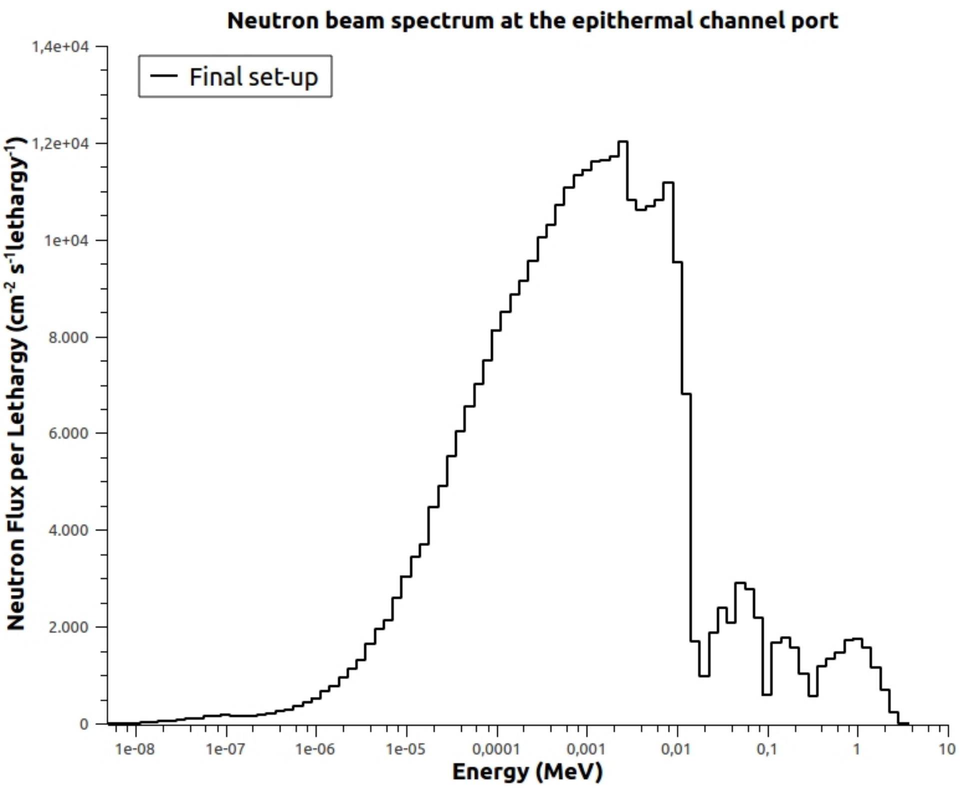

Figure 4.23: Neutron Spectrum emerging in the sideward direction (cell 724) obtained with the final set-up shown in Fig. 4.20 and Fig. 4.21.

As for the thermal beam, also for epithermal beam it is desirable to remove as much gamma radiation as possible from the beam. It is important to note, however, that even removing the gamma component of the beam, there is always a background gamma dose in the patient due to the thermal neutron capture in H, emitting a 2.2 MeV gamma-ray. As mentioned before an important beam quality parameter is the ratio of the gamma dose and the epithermal neutron flux to evaluate the performance of the epithermal and thermal facility respectively. These ratio has a threshold set by IAEA, above which the beam is considered not suitable for an effective and safe BNCT. In order to study the gamma ray component, the spectrum at the beam port has been calculated, the result is plotted in Fig 4.24. The tally has been requested in the cell 724 highlighted in Fig 4.22. The spectrum shows the characteristic peaks of the materials present in the set-up, we can recognize:

- Aluminium at 7724 eV;
- Titanium at 1380 eV, 6418 eV and 6760 eV;
- Carbon (graphite and teflon) at 2881 and 4945 eV.

It has been difficult discriminatig the γ-rays emitted by magnesium at 2881 eV and 3561 eV due to its low absorption cross section, of about 0.063 barns (Appendix A.9), and to the high background.

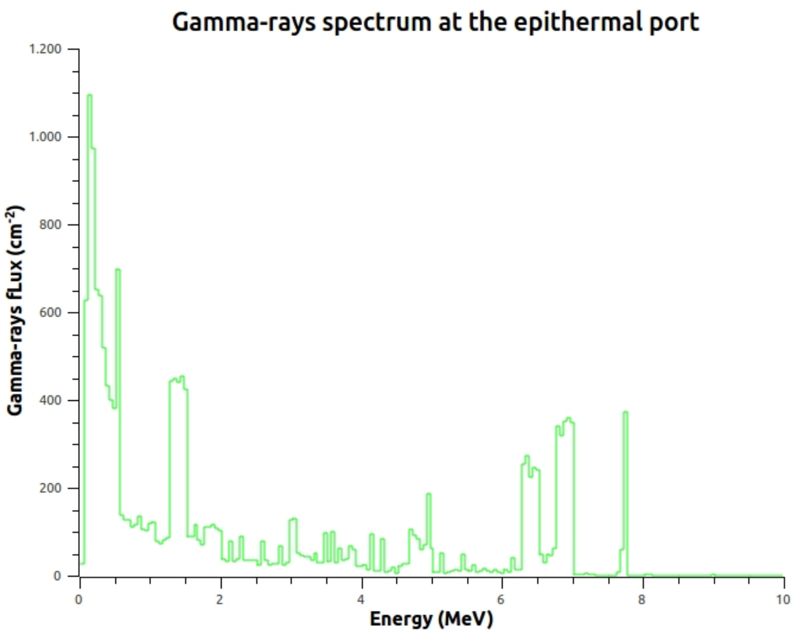

Figure 4.24: Gamma-rays spectrum at the sideward direction (cell 724) obtained with the final set-up shown in Fig. 4.20 and Fig. 4.21.

Chapter 5

Calculation of dose around the facility

This chapter evaluates the total dose due to the thermal neutrons, epithermal neutrons, fast neutrons and gamma-rays contributions in the environment, focusing on the distance-dependence, for radioprotection issues.

5.1 Dose Calculation in MCNP

To evaluate the equivalent dose due to neutrons, for radioprotection issues, it is necessary multiplied the dose by a radiation weighting factor, w_R. It is a dimensionless factor by which the organ or tissue absorbed dose is multiplied to reflect the relative biological effectiveness of high-LET radiations compared with photon radiations.

$$H_t = w_R D_T. \tag{5.1}$$

Where the dose is expressed in gray unit and the equivalent dose in sievert unit (1 Sv = 1 Gy). The neutrons weighting factor energy distribution, ICRP 60 and ICRP 103, is shown in FIg. 5.1 [33].

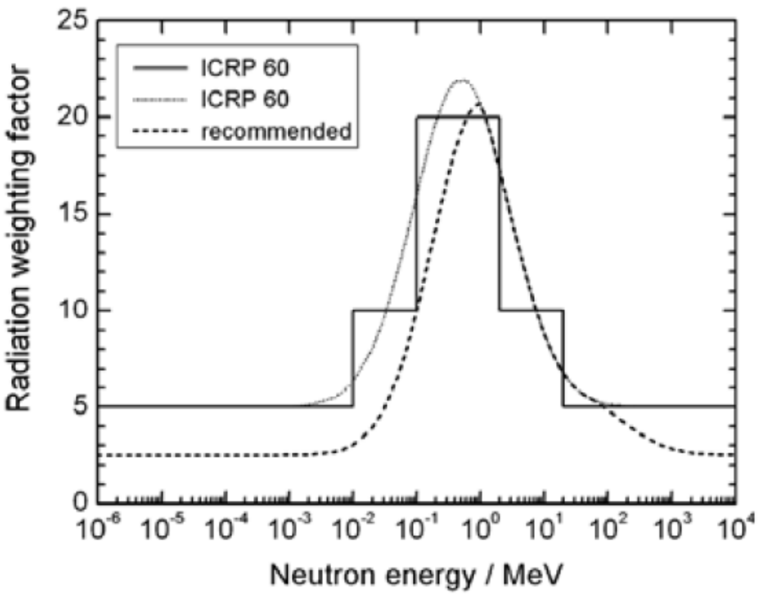

Figure 5.1: Neutrons weighting factor energy distribution from ICRP 60 and ICRP 103.

5.2 Evaluation of the Radiation Dose in the Environment

After developing the thermal and epithermal beams (Chapter 3 and Chapter 4) it was necessary to clad the whole structure by a gamma-ray and a thermal neutron absorber for radioprotection purposes. The facility was covered with a 150 mm thick lead layer (Fig 3.7), which is a good gamma-rays filter due to its high density and Z (Section A.15). Moreover, the graphite box was surrounded by a 50 mm thick lithiated polyethylene layer, that serves as a thermal neutron absorber due to the presence of ^{6}Li (Section B.2). To evaluate the dose radiation in the surrounding environment, six F4 tallies, suitably weighted as explained in Section 5.1, at different distances from the outer surface (0.3 m, 0.6 m, 1 m, 1.5 m, 2 m, and 3 m) of each side of the structure (top, front, thermal channel side and epithermal channel side) have been requested (Fig. 5.2). Two inquiries were investigated: the dose distance-dependence along the beams axes and the dose distribution in the environment outside of the lead shield and the lithiated polyethylene layer.

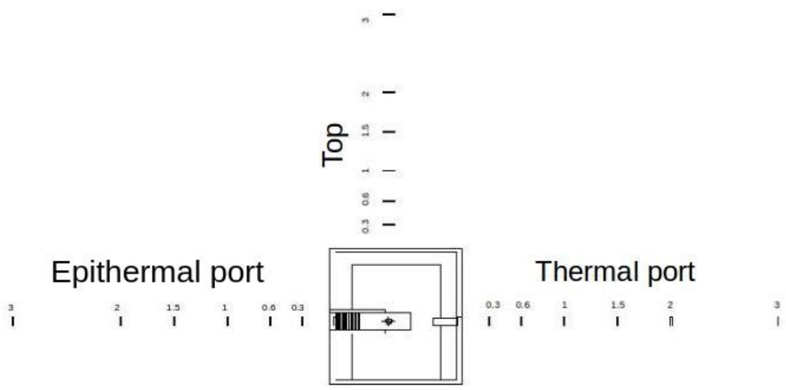

(a) Frontal view of tally positions.

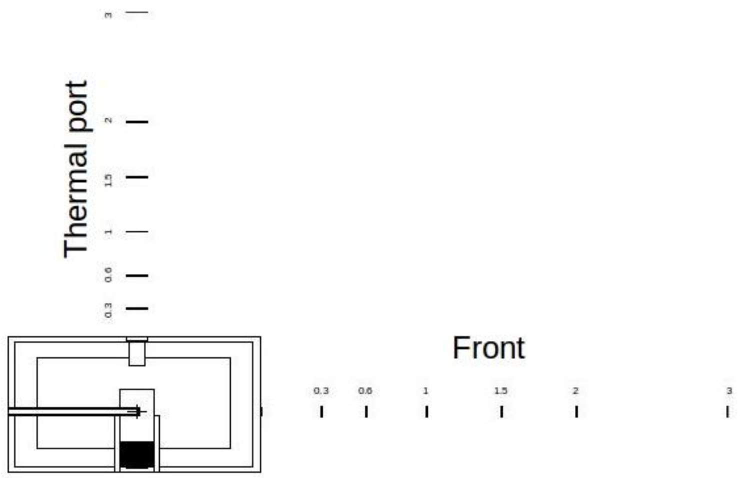

(b) Top view of tally positions.

Figure 5.2: Position of the tallies for dose calculation in the surrounding environment.

The limit value assumed for the absorbed dose is 10 $\mu Sv/h$, calculated from the annual limite value 20 $mSv/year$ considering 2000 working hours. The equivalent thermal neutrons, epithermal neutrons, fast neutrons and gamma-rays dose were calculated, as mentioned in Section 5.1, and added obtaining the total dose to compare with the limite value.

$$H = w_{the}D_{the} + w_{epi}D_{epi} + w_{fast}D_{fast} + D_{\gamma}. \tag{5.2}$$

The results obtained along the beams directions show high values above the limit value at

distances lower than 1 m and 1.5 m, respectively for the thermal (Fig. 5.3b) and epithermal (Fig. 5.3a) beams. However, a beam stopper behind the irradiation position would solve this problem relatively easily.
The values obtained in the case of dose distribution outside of the lead shield comply with the limite value already at close distance (Fig. 5.3 and Fig. 5.4).

For the CN irradiation facility, the dimensions of the graphite moderator box are calculated to slow down the fast neutrons to thermal energies, to be then absorbed by a lithiated polyethylene layer, which covers the facility. The mesh (Fig 5.5) shows how the fast neutron flux distribution is confined into the whole structure, except the beams port.

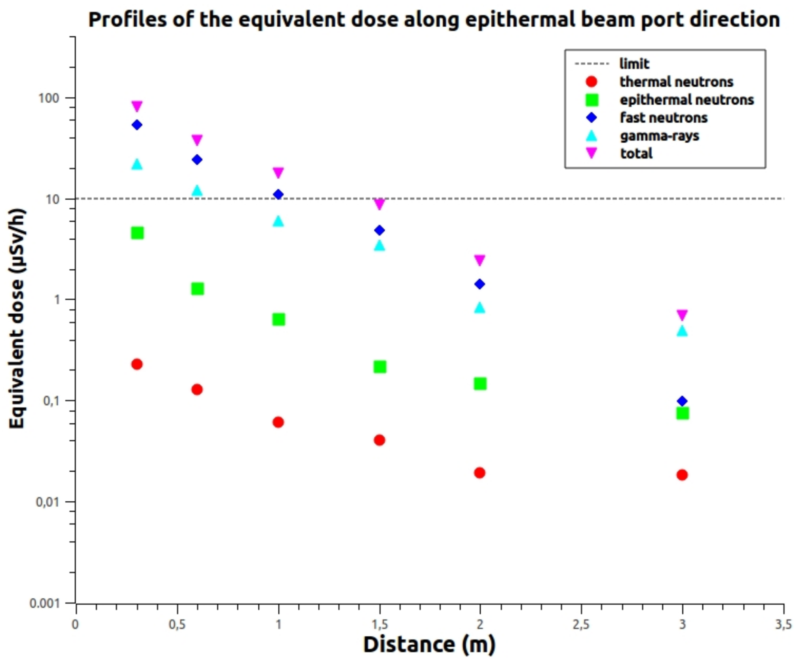

(a) Profile along epithermal beam port direction.

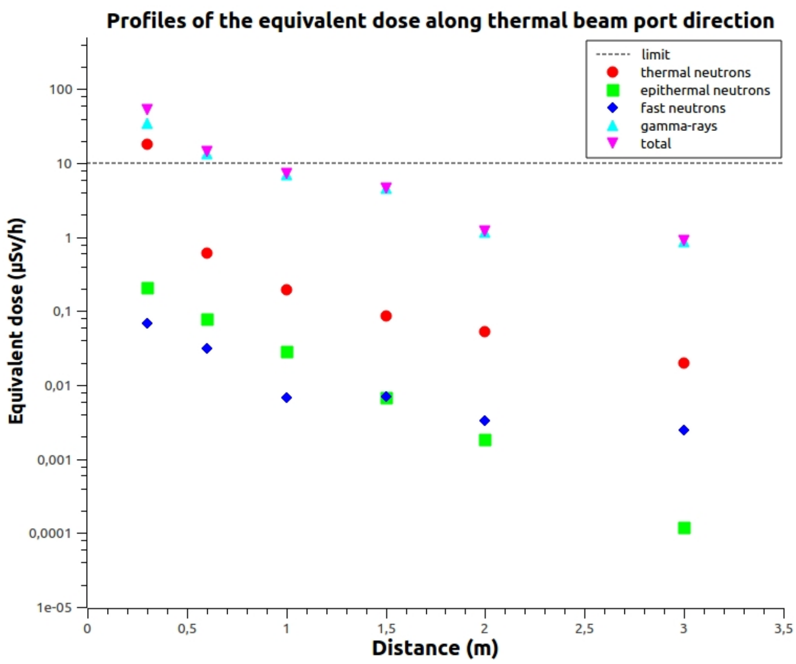

(b) Profile along thermal beam port direction.

Figure 5.3: Profiles of the equivalent total, thermal neutrons, epithermal neutrons, fast neutrons and gamma-rays dose along epithermal and thermal beams side directions.

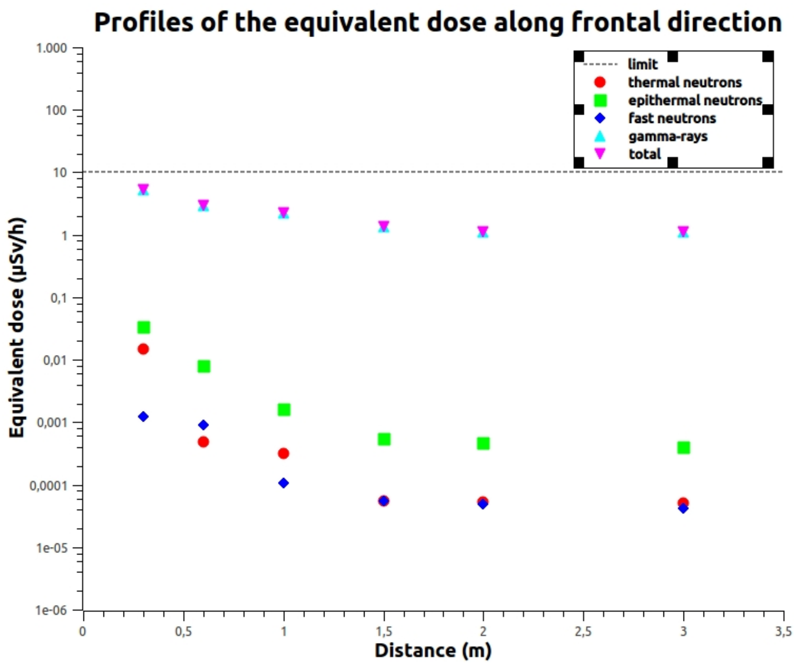

(a) Profile along frontal direction.

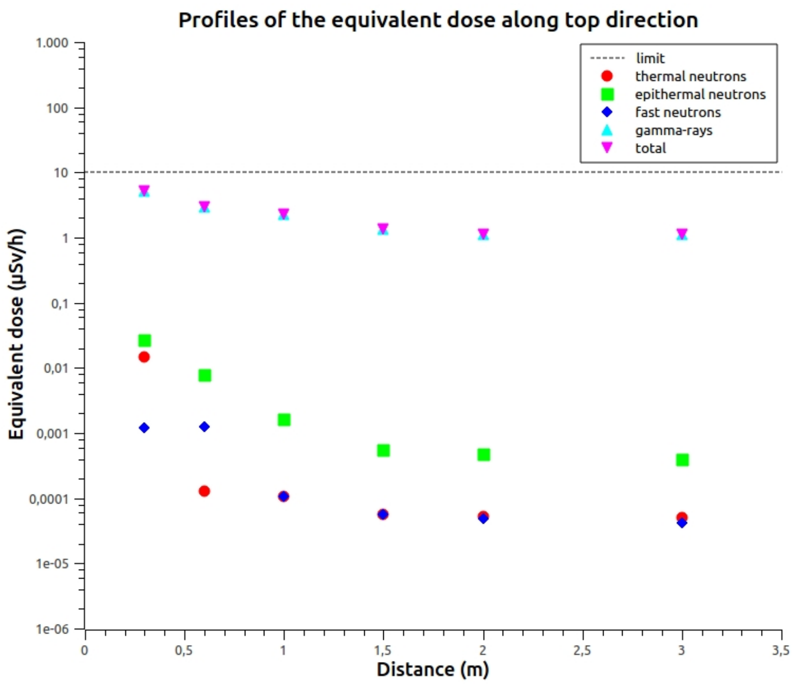

(b) Profiles along top direction.

Figure 5.4: Profiles of the equivalent total, thermal neutrons, epithermal neutrons, fast neutrons and gamma-rays dose along frontal and top directions.

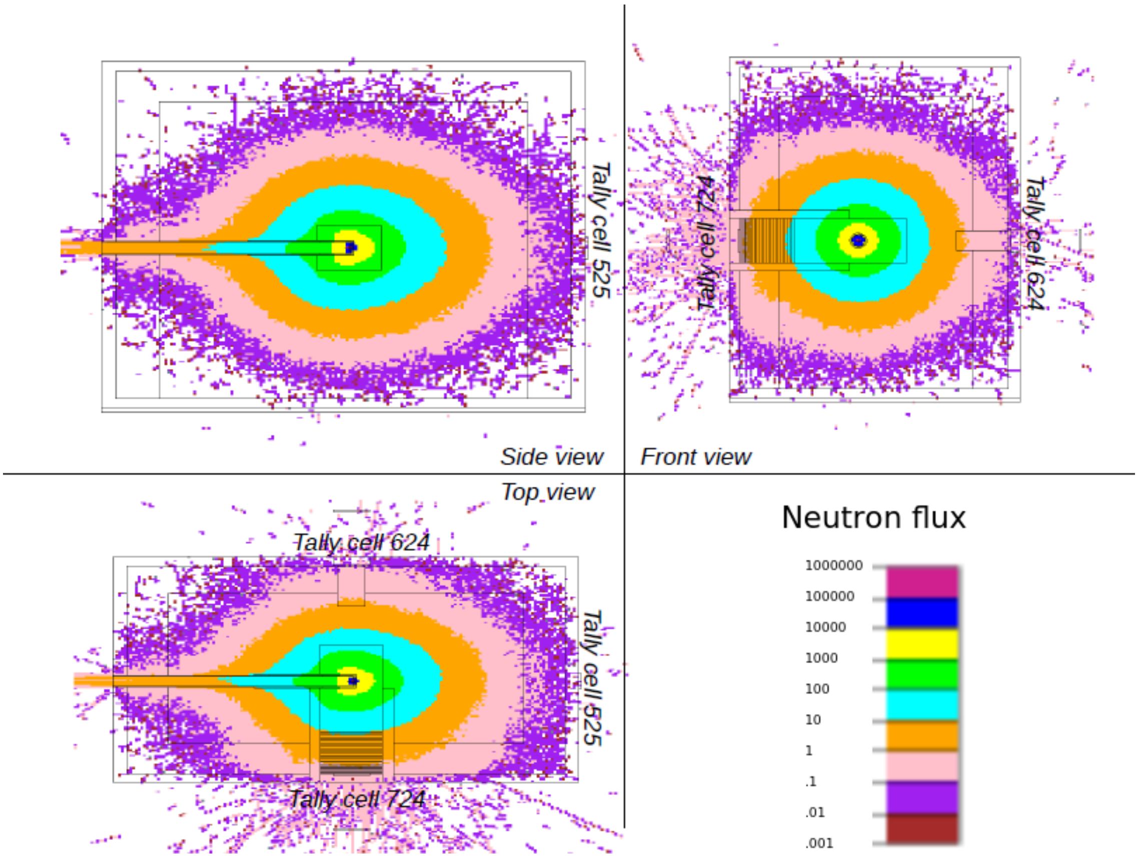

Figure 5.5: Distribution of fast neutron flux in the final set-up with teflon, graphite, bismuth, sandwich filter, and shield superimposed to the planes perpendicular to the neutron source. Results were obtained with mesh tallies calculation.

Chapter 6

Conclusions

The aim of this thesis was to design a BSA for two neutron beams at the CN accelerator in Legnaro National Laboratories. This accelerator provides a proton beam which is coupled with a beryllium target surrounded by a moderator. Neutrons are produced by $^{9}Be(p,n)^{9}B$ reaction with a threshold of 2.5 MeV. To plan the design of the BSA, first of all a neutron source was simulated emerging from the target, on the basis of double differential experimental spectra. The optimization work started from the evaluation of a possible facility exploiting the existing set-up at the CN accelerator, characterized by a heavy water tank used as moderator. The results achieved with this set-up show a high intensity of thermal neutron flux of about 10^5 $cm^{-2}s^{-1}$ at 90^o respect to the proton beam direction, but an epithermal neutron flux of about 10^4 $cm^{-2}s^{-1}$ in the forward direction: this value was too low for our purposes. To increase the neutron flux intensity the heavy water tank was replaced by graphite, gaining further freedom in the design of the BSA because the structural constraint of the tank was thus removed. The fact that two beams had to be designed at the same facility, required careful checks to verify that a change in the confguration of one beam did not change the results obtained for the other. It was demonstrated that changing the configuration towards the epithermal beam port did not change significantly the quality of the thermal beam. The best configuration for the thermal beam, compatible to the assembly of materials simulated for a good epithermal beam, comprised: 170 mm of teflon, 220 mm of graphite and then other 220 mm of bismuth due to absorb γ-rays. With this set-up the obtained thermal neutron flux had the characteristics reported in Table 6.1. The results show that the obtained thermal neutron irradiation facility compies with IAEA requirements for a suitable BNCT beam for shallow tumour treatment.

The tailoring of the epithermal neutron beam can be summarized into these steps:

- Replacing the heavy water tank with graphite;
- Removing of a graphite block and creation of an air channel;
- Evaluation of different materials as moderators for fast energies;
- Ploy of titanium to further reduce fast neutron flux peaks;
- Rotating of the beam port at 90^o degrees;
- Optimization of the 90^o channel solution.

The best solution designed for the epithermal facility is composed by: 200 mm teflon, 10 mm magnesium alloy, 5 mm teflon, 10 mm magnesium alloy, 5x(10 mm aluminium / 5 mm teflon / 15 mm magnesium alloy), 5 mm teflon, 2x(5 mm magnesium alloy / 5 mm

Table 6.1: Neutron flux in the three energy ranges of interest, total neutron flux and beam quality parameters obtained with the final set-up, compared with IAEA recommendations.

Energy Range	Tally 624 Neutron Flux $(cm^{-2}s^{-1})$	IAEA guidelines values
0 eV $<$ E $<$ 0.5 eV	$0.9 \cdot 10^{5}$	
0.5 eV $<$ E $<$ 10 keV	$1.7 \cdot 10^{4}$	
E $>$ 10 keV	$2.03 \cdot 10^{3}$	
Total Flux	$1.07 \cdot 10^{5}$	
$\frac{\phi_{the}}{\phi_{total}}$	84%	
$\frac{\dot{D}_{epi}}{\phi_{the}}$	$1.2 \cdot 10^{-14}$	$2.5 \cdot 10^{-13}$
$\frac{\dot{D}_{fast}}{\phi_{the}}$	$2.1 \cdot 10^{-13}$	$2.5 \cdot 10^{-13}$
$\frac{\dot{D}_{\gamma}}{\phi_{the}}$	$2.0 \cdot 10^{-13}$	$2.0 \cdot 10^{-13}$

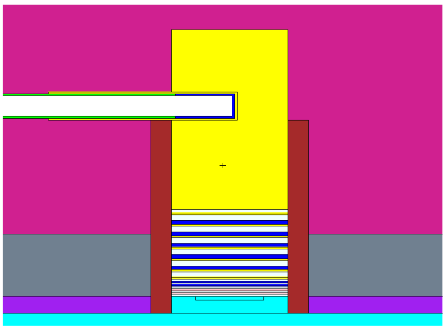

Figure 6.1: Final set-up of the epithermal neutron beam port.

aluminium), 2x(5 mm magnesium alloy / 5 mm titanium), and 5 mm magnesium alloy; for a total thickness of 420 mm of moderator (Fig. 6.1).

The results achieved are shown in Table 6.2. The epithermal neutron beam meets the requirements indicated by IAEA for a safe and effective BNCT except for a higher fast neutron dose contamination. However the value of the contamination is similar to the one present in some neutron beams used in clinical BNCT. If the current would be 30 mA, as achieved by the RFQ accelerator, this BSA would provide a epithermal neutron flux of $2.2 \cdot 10^9$ $cm^{-2}s^{-1}$, that would allow for short treatment times in according to IAEA's guidelines.

Table 6.2: Neutron flux in the three energy ranges of interest, total neutron flux and beam quality parameters obtained with the final set-up shown in Fig. 6.1, compared with IAEA recommendations.

Energy Range	Tally 724 Neutron Flux ($cm^{-2}s^{-1}$)	IAEA guidelines values
0 eV < E < 0.5 eV	$1.51 \cdot 10^3$	
0.5 eV < E < 10 keV	$2.2 \cdot 10^5$	10^9
E > 10 keV	$3.4 \cdot 10^4$	
Total Flux	$2.6 \cdot 10^5$	
$\frac{\phi_{epi}}{\phi_{total}}$	84%	
$\frac{\dot{D}_{the}}{\phi_{epi}}$	$1.1 \cdot 10^{-15}$	$2.5 \cdot 10^{-13}$
$\frac{\dot{D}_{fast}}{\phi_{epi}}$	$8.7 \cdot 10^{-13}$	$2.5 \cdot 10^{-13}$
$\frac{\dot{D}_{\gamma}}{\phi_{epi}}$	$2.4 \cdot 10^{-13}$	$2.0 \cdot 10^{-13}$

Finally, some preliminary radioprotection calculations have been performed, in particular the dose around the facility was simulated. The results outside the lead shield and lithiated polyethylene surrounding the graphite box moderator are below the limit value of 10 $\mu Sv/h$ valid for controlled areas. A beam stopper behind the irradiation position will solve the problem of the radioprotection along the beams direction.

The designed facility in this thesis provides two neutron beams which complies the IAEA recommendations. The tailoring has been performed taking into account that the final project should be easy to implement and not excessively expensive. The assembly of materials and the geometry of the facility have been thus selected to satisfy these criteria, enabling the construction of the set-up in the immediate future.

Appendix A

Cross Section and Thermal Neutron Capture

The Cross Section, the γ's Spectrum due to the neutron radiative capture and the X-Ray mass attenuation coefficients of each element are summarized in this Appendix. Data and images from [2], [44] and [45].

A.1 Hydrogen

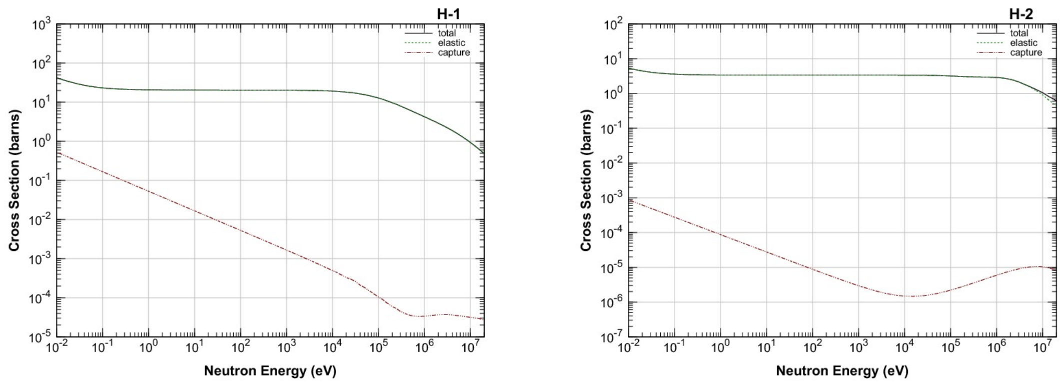

(a) ^1H natural abundance: 99.9885%.   **(b)** ^2H natural abundance: 0.0115%.

Figure A.1: Hydrogen Cross Sections.

Table A.1: Thermal Neutron Capture Gammas, Target Nucleus ^1H.

$E\gamma$ (keV)	$\Delta Ep\gamma$ (keV)	$\frac{I\gamma}{I\gamma_{max}}$	$\Delta\frac{I\gamma}{I\gamma_{max}}$
2223.25	0.00	100.00	0.00

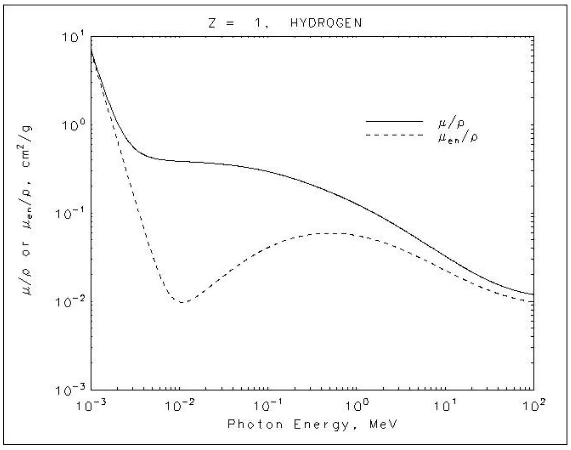

Figure A.2: Hydrogen X-Ray mass attenuation coefficients.

Table A.2: Thermal Neutron Capture Gammas, Target Nucleus ^{2}H.

$E\gamma$ (keV)	$\Delta Ep\gamma$ (keV)	$\frac{I\gamma}{I\gamma_{max}}$	$\Delta\frac{I\gamma}{I\gamma_{max}}$
6250.26	0.00	100.00	0.00

A.2 Lithium

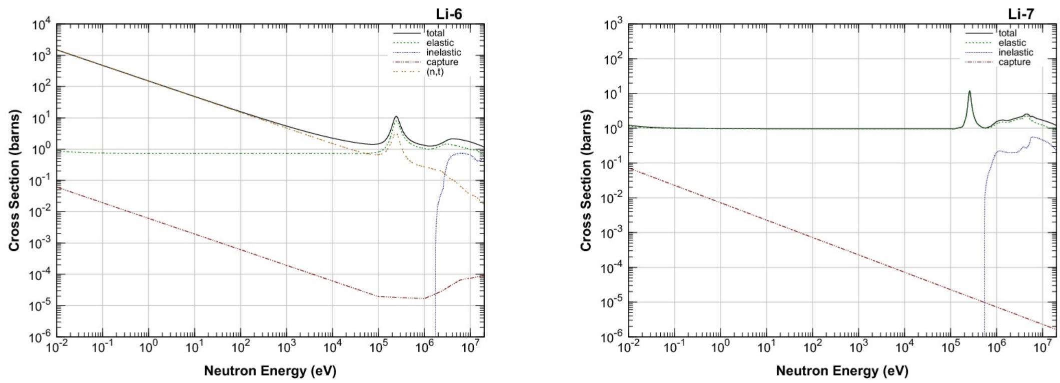

(a) ^{6}Li natural abundance: 7.5%.

(b) ^{7}Li natural abundance: 92.5%.

Figure A.3: Lithium Cross Sections.

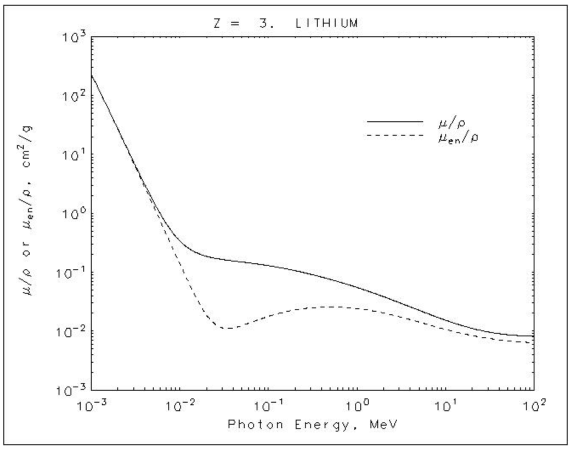

Figure A.4: Lithium X-Ray mass attenuation coefficients.

Table A.3: Thermal Neutron Capture Gammas, Target Nucleus ^{6}Li.

$E\gamma$ (keV)	$\Delta Ep\gamma$ (keV)	$\frac{I\gamma}{I\gamma_{max}}$	$\Delta\frac{I\gamma}{I\gamma_{max}}$
477.60	0.00	61.29	3.78
6768.81	0.05	61.29	3.78
7245.91	0.05	100.00	4.56

Table A.4: Thermal Neutron Capture Gammas, Target Nucleus ^{7}Li.

$E\gamma$ (keV)	$\Delta Ep\gamma$ (keV)	$\frac{I\gamma}{I\gamma_{max}}$	$\Delta\frac{I\gamma}{I\gamma_{max}}$
980.70	0.20	11.86	1.13
1052.00	0.20	11.86	1.13
2032.50	0.30	100.00	1.58

A.3 Beryllium

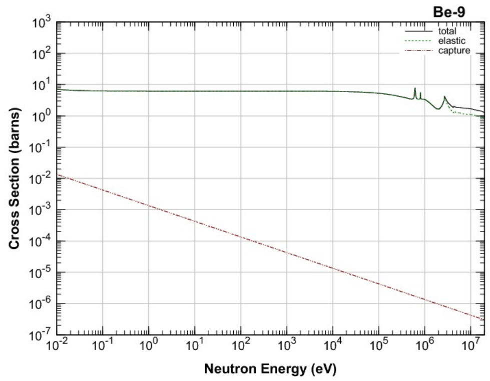

(a) Beryllium Cross Sections.

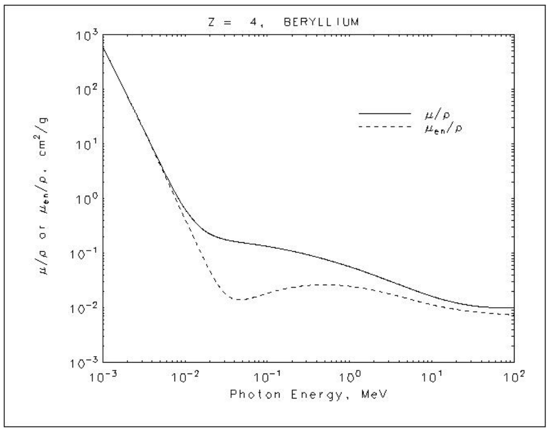

(b) Beryllium X-Ray mass attenuation coefficients.

Figure A.5: Beryllium Cross Sections and X-Ray mass attenuation coefficients.

Table A.5: Thermal Neutron Capture Gammas, Target Nucleus ^{9}Be.

$E\gamma$ (keV)	$\Delta Ep\gamma$ (keV)	$\frac{I\gamma}{I\gamma_{max}}$	$\Delta\frac{I\gamma}{I\gamma_{max}}$
853.63	0.01	35.81	6.24
2590.01	0.02	32.93	5.01
3367.45	0.03	49.17	7.34
6809.61	0.03	100.00	15.45

A.4 Boron

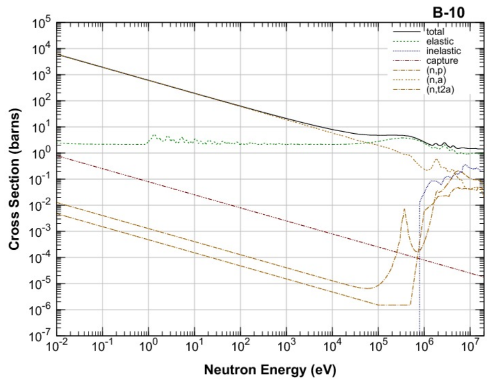

(a) ^{10}B natural abundance: 19.9%.

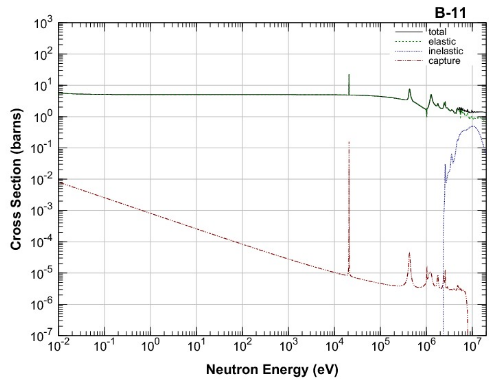

(b) ^{11}B natural abundance: 80.1%.

Figure A.6: Boron Cross Sections.

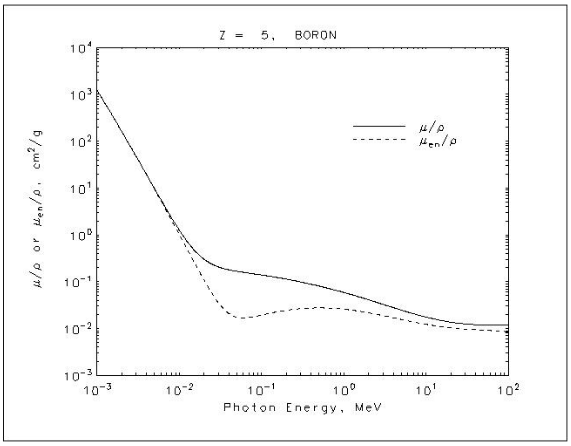

Figure A.7: Boron X-Ray mass attenuation coefficients.

Table A.6: Thermal Neutron Capture Gammas, Target Nucleus ^{10}B.

$E\gamma$ (keV)	$\Delta Ep\gamma$ (keV)	$\frac{I\gamma}{I\gamma_{max}}$	$\Delta\frac{I\gamma}{I\gamma_{max}}$
4444.03	0.08	100.00	4.96
4711.18	0.07	39.02	1.94
7006.75	0.07	84.30	3.83

A.5 Carbon

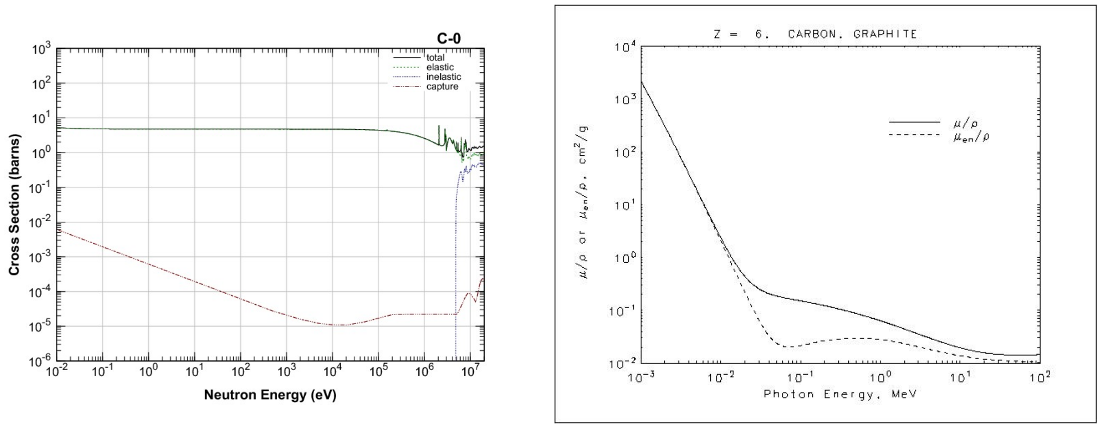

(a) Carbon Cross Sections. **(b)** Carbon X-Ray mass attenuation coefficients.

Figure A.8: Carbon Cross Sections and X-Ray mass attenuation coefficients.

Table A.7: Thermal Neutron Capture Gammas, Target Nucleus ^{12}C and ^{13}C.

$E\gamma$ (keV)	$\Delta Ep\gamma$ (keV)	$\frac{I\gamma}{I\gamma_{max}}$	$\Delta\frac{I\gamma}{I\gamma_{max}}$
1860.00	0.00	57.00	0.00
3090.00	0.00	100.00	0.00
4945.30	0.00	67.47	0.92
8174.00	0.30	100.00	3.87

A.6 Nitrogen

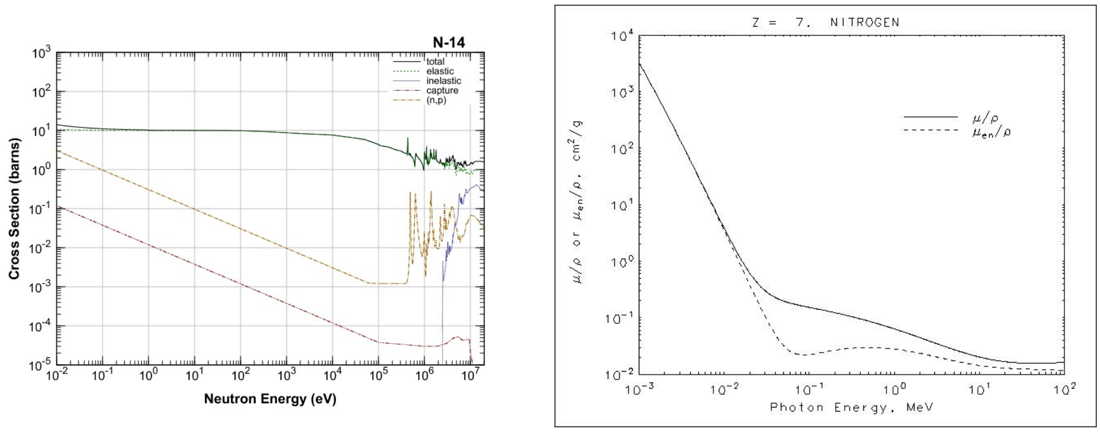

(a) Nitrogen Cross Sections. **(b)** Nitrogen X-Ray mass attenuation coefficients.

Figure A.9: Nitrogen Cross Sections and X-Ray mass attenuation coefficients.

Table A.8: Thermal Neutron Capture Gammas, Target Nucleus ^{14}N.

$E\gamma$ (keV)	$\Delta Ep\gamma$ (keV)	$\frac{I\gamma}{I\gamma_{max}}$	$\Delta\frac{I\gamma}{I\gamma_{max}}$
1884.78	0.02	62.86	0.92
3677.74	0.02	48.63	0.73
4508.73	0.02	55.96	0.80
5269.16	0.02	100.00	1.42
5297.83	0.02	71.10	1.03
5533.39	0.02	65.57	0.96
6322.43	0.02	61.05	0.96
10829.11	0.06	47.89	2.07

A.7 Oxygen

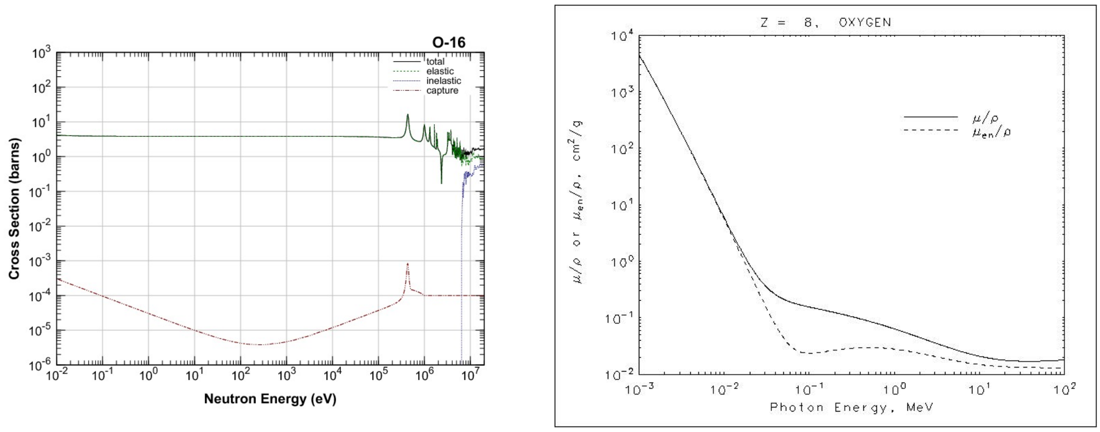

(a) Oxygen Cross Sections.

(b) Oxygen X-Ray mass attenuation coefficients.

Figure A.10: Oxygen Cross Sections and X-Ray mass attenuation coefficients.

Table A.9: Thermal Neutron Capture Gammas, Target Nucleus ^{16}O.

$E\gamma$ (keV)	$\Delta Ep\gamma$ (keV)	$\frac{I\gamma}{I\gamma_{max}}$	$\Delta\frac{I\gamma}{I\gamma_{max}}$
870.71	0.12	100.00	0.00
1087.93	0.11	82.00	3.00
2184.48	0.20	82.00	3.00
3320.00	0.00	76.00	0.00

A.8 Fluorine

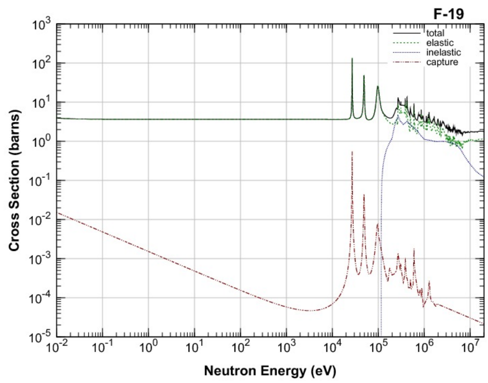

(a) Fluorine Cross Sections.

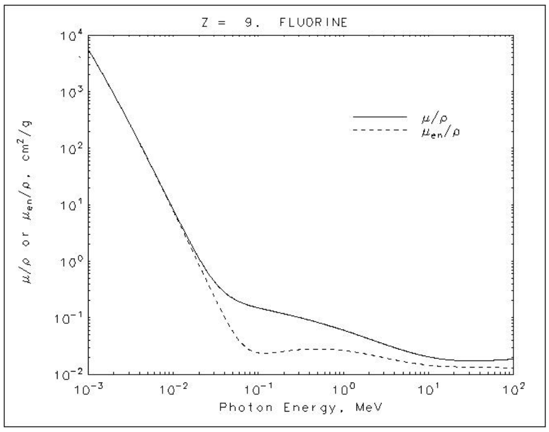

(b) Fluorine X-Ray mass attenuation coefficients.

Figure A.11: Fluorine Cross Sections and X-Ray mass attenuation coefficients.

Table A.10: Thermal Neutron Capture Gammas, Target Nucleus ^{19}F.

$E\gamma$ (keV)	$\Delta Ep\gamma$ (keV)	$\frac{I\gamma}{I\gamma_{max}}$	$\Delta\frac{I\gamma}{I\gamma_{max}}$
583.55	0.03	100.00	5.90
656.00	0.03	55.01	3.60
665.20	0.03	41.40	2.81

A.9 Magnesium

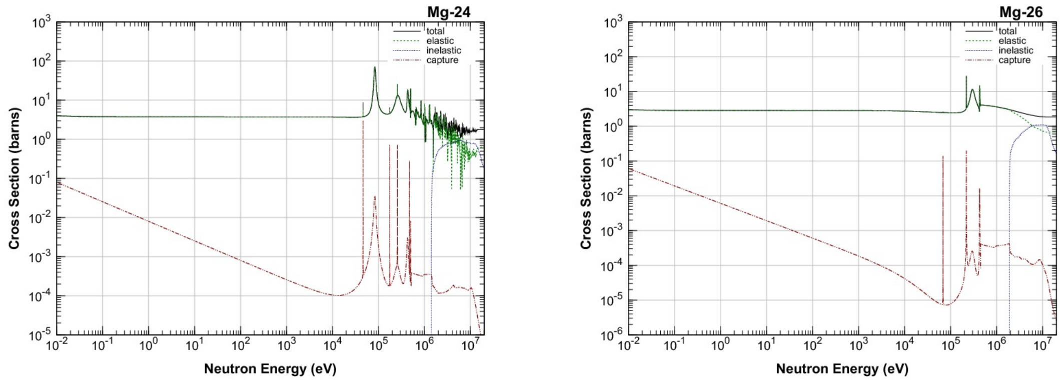

(a) ^{24}Mg natural abundance: 78.99%. **(b)** ^{26}Mg natural abundance: 11.01%.

Figure A.12: Magnesium Cross Sections.

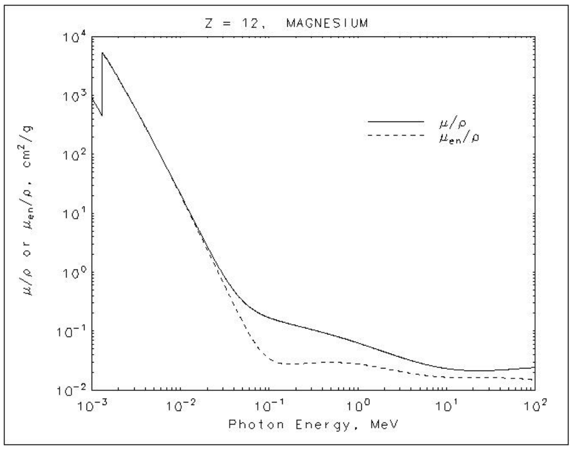

Figure A.13: Magnesium X-Ray mass attenuation coefficients.

Table A.11: Thermal Neutron Capture Gammas, Target Nucleus ^{24}Mg.

$E\gamma$ (keV)	$\Delta Ep\gamma$ (keV)	$\frac{I\gamma}{I\gamma_{max}}$	$\Delta\frac{I\gamma}{I\gamma_{max}}$
585.06	0.03	100.00	8.55
2828.21	0.20	75.75	6.42
3916.85	0.05	99.51	8.52

Table A.12: Thermal Neutron Capture Gammas, Target Nucleus ^{26}Mg.

$E\gamma$ (keV)	$\Delta Ep\gamma$ (keV)	$\frac{I\gamma}{I\gamma_{max}}$	$\Delta\frac{I\gamma}{I\gamma_{max}}$
2881.67	0.04	100.00	5.50
3561.31	0.04	91.79	4.98

A.10 Aluminium

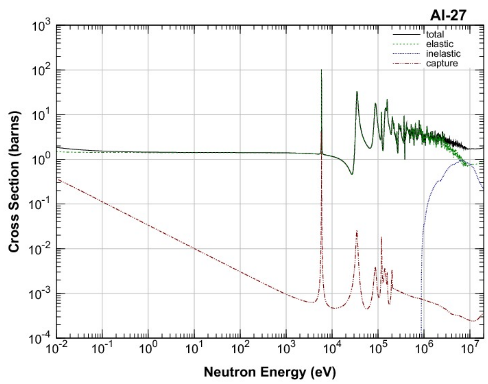

(a) Aluminium Cross Sections.

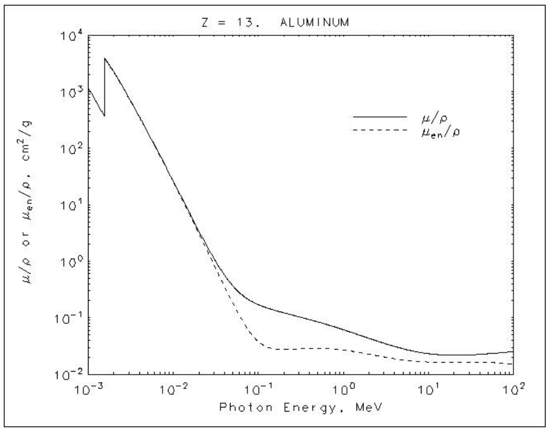

(b) Aluminium X-Ray mass attenuation coefficients.

Figure A.14: Aluminium Cross Sections and X-Ray mass attenuation coefficients.

Table A.13: Thermal Neutron Capture Gammas, Target Nucleus ^{27}Al.

$E\gamma$ (keV)	$\Delta Ep\gamma$ (keV)	$\frac{I\gamma}{I\gamma_{max}}$	$\Delta\frac{I\gamma}{I\gamma_{max}}$
30.64	0.00	100.00	0.00
7724.03	0.01	96.06	0.36

A.11 Silicon

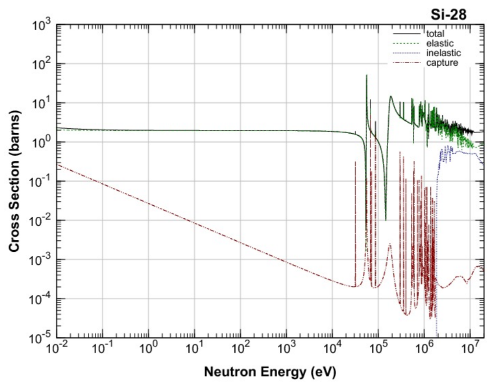

(a) Silicon Cross Sections.

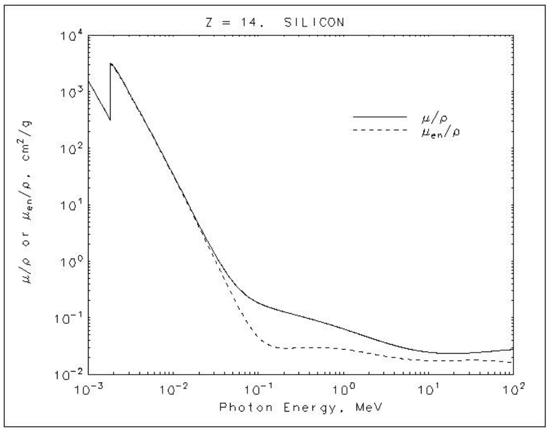

(b) Silicon X-Ray mass attenuation coefficients.

Figure A.15: Silicon Cross Sections and X-Ray mass attenuation coefficients.

Table A.14: Thermal Neutron Capture Gammas, Target Nucleus ^{28}Si.

$E\gamma$ (keV)	$\Delta Ep\gamma$ (keV)	$\frac{I\gamma}{I\gamma_{max}}$	$\Delta\frac{I\gamma}{I\gamma_{max}}$
3538.98	0.04	100.00	5.81
4933.98	0.03	93.27	5.09

A.12 Titanium

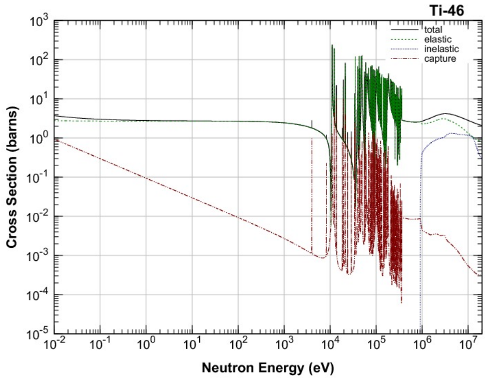

(a) ^{46}Ti natural abundance: 8.0%.

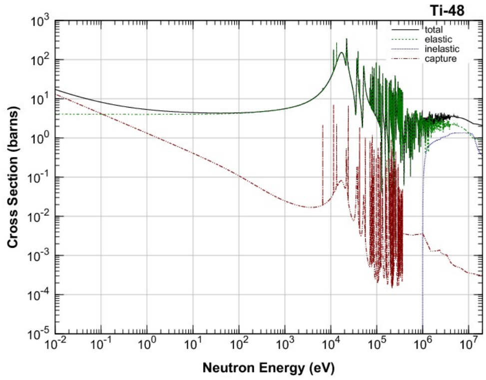

(b) ^{48}Ti natural abundance: 73.8%.

Figure A.16: Titanium Cross Sections.

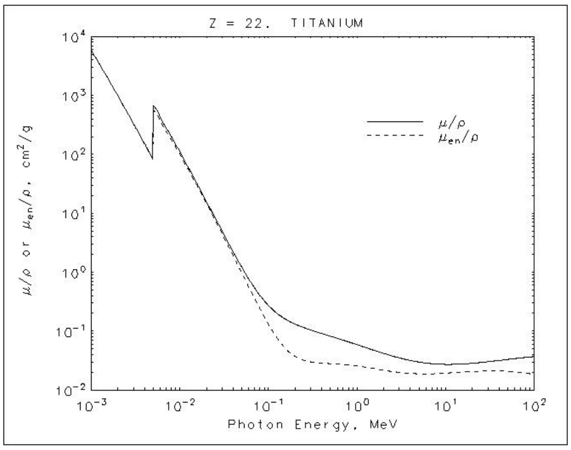

Figure A.17: Titanium X-Ray mass attenuation coefficients.

Table A.15: Thermal Neutron Capture Gammas, Target Nucleus ^{46}Ti.

$E\gamma$ (keV)	$\Delta Ep\gamma$ (keV)	$\frac{I\gamma}{I\gamma_{max}}$	$\Delta\frac{I\gamma}{I\gamma_{max}}$
159.27	0.04	100.00	0.00
1390.33	0.10	50.00	0.00
2556.00	4.00	40.00	0.00
7086.80	0.40	40.00	0.00

Table A.16: Thermal Neutron Capture Gammas, Target Nucleus ^{48}Ti.

$E\gamma$ (keV)	$\Delta Ep\gamma$ (keV)	$\frac{I\gamma}{I\gamma_{max}}$	$\Delta\frac{I\gamma}{I\gamma_{max}}$
1381.74	0.00	100.00	7.87
6418.53	0.06	35.67	2.69
6760.12	0.04	54.15	4.08

A.13 Nichel

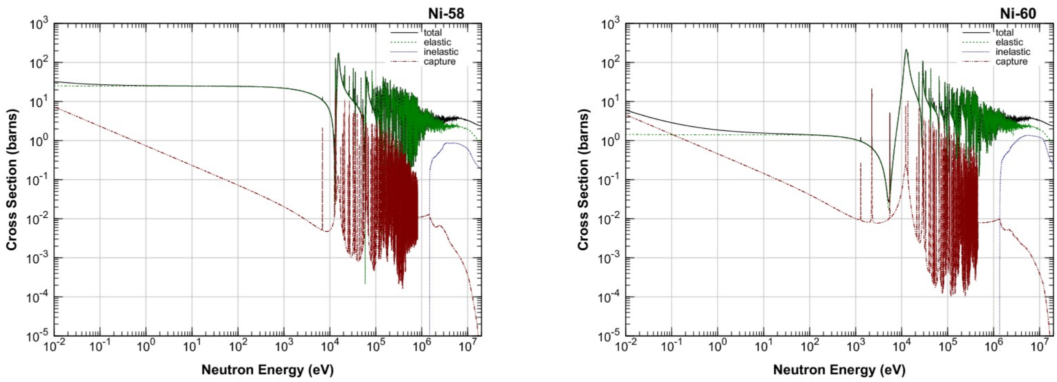

(a) ^{58}Ni natural abundance: 68.08%. **(b)** ^{60}Ni natural abundance: 26.23%.

Figure A.18: Nichel Cross Sections.

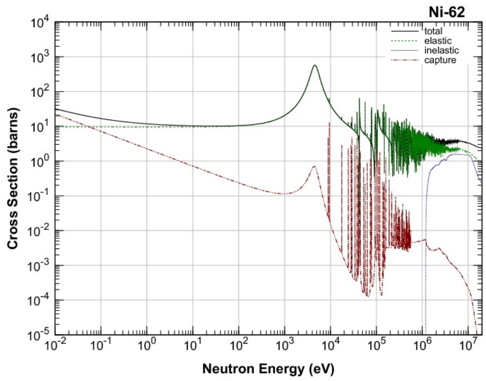

(a) ^{62}Ni natural abundance: 3.6%.

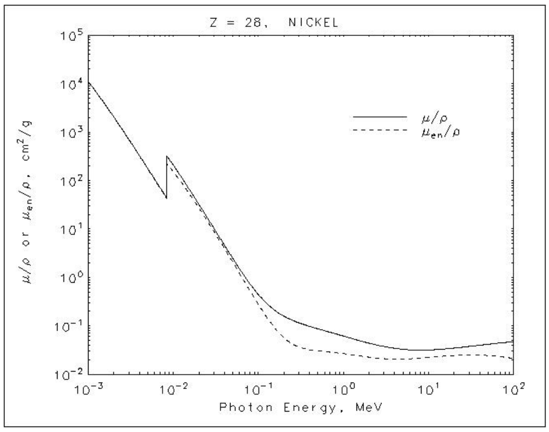

(b) Nichel X-Ray mass attenuation coefficients.

Figure A.19: Nichel Cross Sections and X-Ray mass attenuation coefficients.

Table A.17: Thermal Neutron Capture Gammas, Target Nucleus ^{58}Ni.

$E\gamma$ (keV)	$\Delta Ep\gamma$ (keV)	$\frac{I\gamma}{I\gamma_{max}}$	$\Delta\frac{I\gamma}{I\gamma_{max}}$
464.94	0.03	54.08	1.55
8533.71	0.07	47.84	0.99
8998.63	0.07	100.00	2.04

Table A.18: Thermal Neutron Capture Gammas, Target Nucleus ^{60}Ni.

$E\gamma$ (keV)	$\Delta Ep\gamma$ (keV)	$\frac{I\gamma}{I\gamma_{max}}$	$\Delta\frac{I\gamma}{I\gamma_{max}}$
282.99	0.05	65.69	2.32
7536.62	0.06	57.03	1.00
7819.56	0.06	100.00	1.71

A.14 Iron

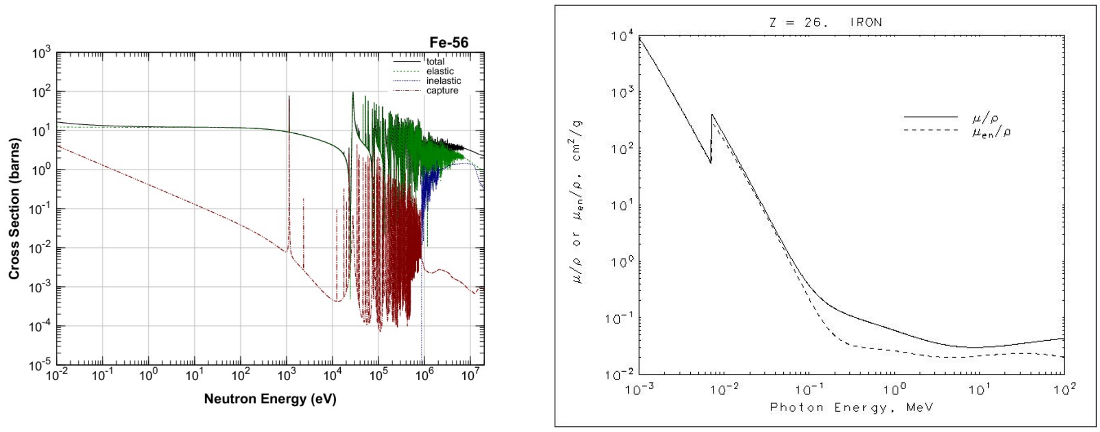

(a) Iron Cross Sections.

(b) Iron X-Ray mass attenuation coefficients.

Figure A.20: Silicon Cross Sections and X-Ray mass attenuation coefficients.

Table A.19: Thermal Neutron Capture Gammas, Target Nucleus ^{56}Fe.

$E\gamma$ (keV)	$\Delta Ep\gamma$ (keV)	$\frac{I\gamma}{I\gamma_{max}}$	$\Delta\frac{I\gamma}{I\gamma_{max}}$
6018.42	0.07	34.14	7.28
7631.18	0.10	100.00	24.09
7645.58	0.10	86.21	19.94

A.15 Lead

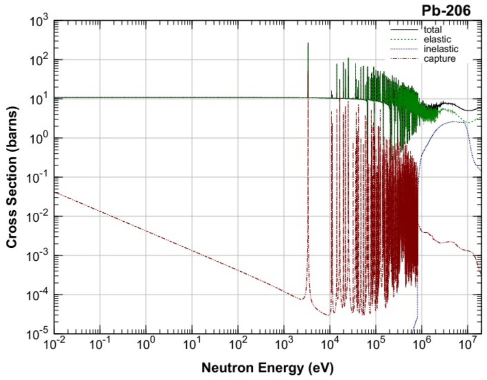

(a) ^{206}Pb natural abundance: 24.1%.

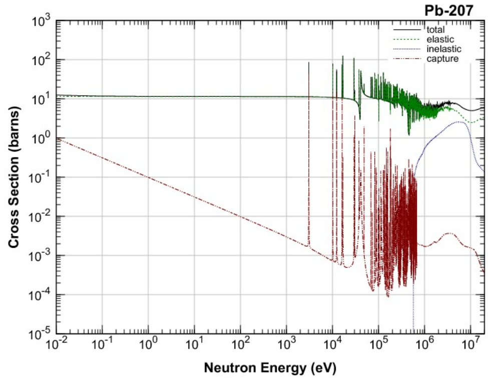

(b) ^{207}Pb natural abundance: 22.1%.

Figure A.21: Lead Cross Sections.

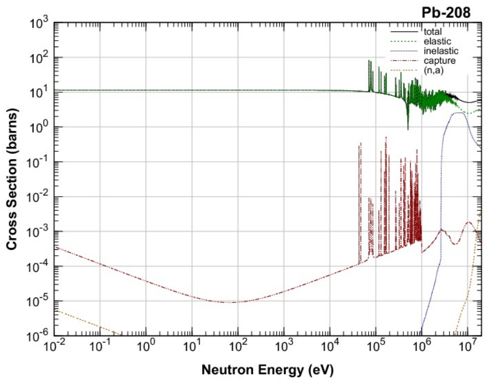

(a) ^{208}Pb natural abundance: 52.4%.

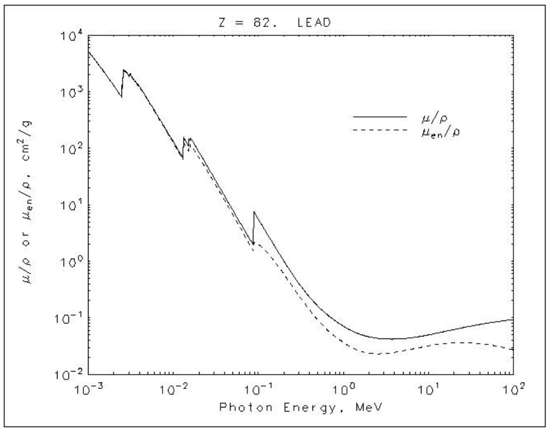

(b) Lead X-Ray mass attenuation coefficients.

Figure A.22: Lead Cross Sections and X-Ray mass attenuation coefficients.

A.16 Bismuth

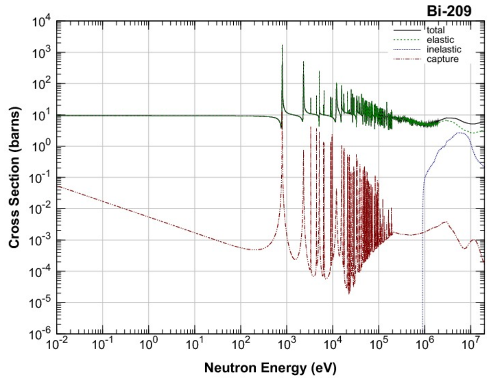

(a) Bismuth Cross Sections.

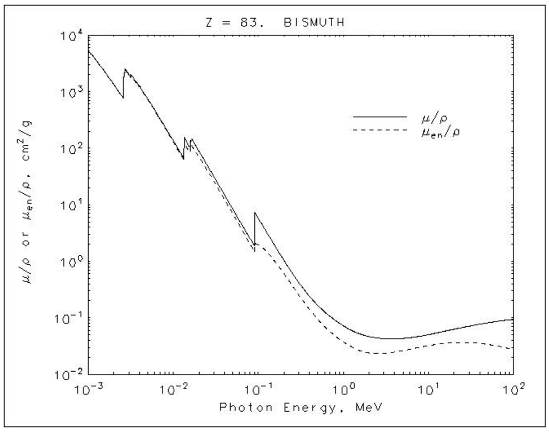

(b) Bismuth X-Ray mass attenuation coefficients.

Figure A.23: Bismuth Cross Sections and X-Ray mass attenuation coefficients.

Table A.20: Thermal Neutron Capture Gammas, Target Nucleus ^{209}Bi.

$E\gamma$ (keV)	$\Delta Ep\gamma$ (keV)	$\frac{I\gamma}{I\gamma_{max}}$	$\Delta\frac{I\gamma}{I\gamma_{max}}$
162.20	0.06	62.79	3.19
319.74	0.06	100.00	4.93
4054.72	0.08	58.14	2.31
4171.27	0.08	71.51	3.04

Appendix B

Composition of Materials

In this section is reported the percentage composition of the main materials used in the MC simulations of this thesis.

B.1 Lithium Carbonate

Table B.1: Composition of natural lithium carbonate, Li_2CO_3 ($\rho = 2.1\,g/cm^3$)

Materials	Percentage by weight
^6Li	1.22%
^7Li	17.57%
C	16.26%
^{16}O	64.95%

B.2 Lithiated Polyethylene

Table B.2: Composition of lithiated polyethylene ($\rho = 1.06\,g/cm^3$)

Materials	Percentage by weight
^6Li	0.55%
^7Li	6.73%
C	84.12%
^1H	8.60%

B.3 Lithium Fluoride

Table B.3: Composition of Lithium Fluoride, LiF ($\rho = 2.63\,g/cm^3$)

Materials	Percentage by weight
C	27%
F	73%

B.4 PTFE (Teflon)

Table B.4: Composition of Polytetrafluoroethylene (Teflon), C_2F_4 ($\rho = 2.2\,g/cm^3$)

Materials	Percentage by weight
C	24%
F	76%

B.5 Titanium Ti6Al4V

Table B.5: Composition of Titanium Ti6Al4V Grade5 ($\rho = 4.4\,g/cm^3$)

Materials	Percentage by weight
Ti	94%
Al	6%

B.6 Magnesium Fluoride

Table B.6: Composition of Magnesium Fluoride MgF_2 ($\rho = 3.2\,g/cm^3$)

Materials	Percentage by weight
Mg	39%
F	61%

B.7 Magnesium Alloy

Table B.7: Composition of Magnesium Alloy AZ61 ($\rho = 1.8\, g/cm^3$)

Materials	Percentage by weight
Mg	93%
Al	7%

B.8 Fluental$^{\mathrm{TM}}$

Table B.8: Composition of Fluental$^{\mathrm{TM}}$($\rho = 4.507\, g/cm^3$)

Materials	Percentage by weight
Al	30%
AlF_3	69%
LiF	1%

Appendix C

MCNP6 CODE

In this section is reported the MCNP6 code used in the simulations of this thesis.

C.1 MCNP6 CODE

SDEF Variables.

```
c*************************************************************
-- Channel
c
c              90 degrees
c
c ---------------------------------------------------------------------------
c
c              CELLS
c
c ---------------------------------------------------------------------------
1 0 117                 imp:n,p =0      $ empty
2 10 -0.001124 7 8 12 14 22  200 201 -117 1444 1445 1446 1447 1448 1449 &
1454 1455 1456 1457 1458 1459 1464 1465 1466 1467 1468 1469 &
 1474 1475 1476 1477 1478 1479  imp:n,p =1      $ environment
999 10 -0.001124 -203 14 imp:n,p =1                     $ air
998 10 -0.001124 -109 22 imp:n,p =1                     $ air
c ---------------------------------------------------------------------------
c              SOURCE TUBE
c ---------------------------------------------------------------------------
3 4 -2.7 1 -3           imp:n,p =1      $  acc. (Al)
4 7 -7.75 1 -2          imp:n,p =1      $  acc. (iron)
5 0 -1                  imp:n,p =1      $  Vacuum tube
6 6 -2.2 2 3 -4         imp:n,p =1      $  teflon cladding
c ---------------------------------------------------------------------------
c              GRAPHITE CUBE
c ---------------------------------------------------------------------------
9 2 -1.7 2 4 20 21  111 50 -7 imp:n,p =4        $ boxgra
c ---------------------------------------------------------------------------
c              CANALE
c ---------------------------------------------------------------------------
7 6 -2.2 -50 4 1 2 3 imp:n,p =4 $ ch teflon
19 60 -1.8 -55 imp:n,p =4       $ ch Mg alloy
20 6 -2.2 -56 imp:n,p =4        $  ch teflon
21 60 -1.8 -57 imp:n,p =4       $ ch Mg alloy
22 4 -2.7 -58 imp:n,p =4        $  ch Al
23 6 -2.2 -59 imp:n,p =4        $  ch teflon
24 60 -1.8 -60 imp:n,p =4       $ ch Mg alloy
25 4 -2.7 -61 imp:n,p =4        $ ch Al
26 6 -2.2 -63 imp:n,p =4        $  ch teflon
27 60 -1.8 -64 imp:n,p =4       $ ch Mg alloy
28 4 -2.7 -65 imp:n,p =4        $ ch Al
29 6 -2.2 -66 imp:n,p =4        $  ch teflon
32 60 -1.8 -67 imp:n,p =4       $ ch Mg alloy
33 4 -2.7 -68 imp:n,p =4        $ ch Al
34 6 -2.2 -69 imp:n,p =4        $  ch teflon
35 60 -1.8 -70 imp:n,p =4       $ ch Mg alloy
```

```
36 4 -2.7 -71 imp:n,p =4        $ ch Al
37 6 -2.2 -72 imp:n,p =4        $  ch teflon
38 60 -1.8 -73 imp:n,p =4       $ ch Mg alloy
39 6 -2.2 -74 imp:n,p =4        $  ch teflon
40 60 -1.8  -75 imp:n,p =4      $ ch Mg alloy
41 4 -2.7 -76 imp:n,p =4        $ ch Al
42  60 -1.8 -77 imp:n,p =4      $ ch Mg alloy
43 4 -2.7 -78 imp:n,p =4        $ ch Al
44 60 -1.8 -79 imp:n,p =4       $ ch Mg alloy
45 9 -4.4 -80 imp:n,p =4        $ ch Ti
46 60 -1.8 -81 imp:n,p =4       $ ch Mg alloy
47 9 -4.4 -82 imp:n,p =4        $ ch Ti
48 60 -1.8 -83 imp:n,p =4       $ ch Mg alloy
1010 14 -2.11 -111 4 50 112 imp:n,p =4  $ shield
c  -----------------------------------------------------------------------------
c  -----------------------------------------------------------------------------
c               BISMUTH BOX
c  -----------------------------------------------------------------------------
12 12 -9.8 -20          imp:n,p =4      $ box bismuto
c  -----------------------------------------------------------------------------
c               Al TABLE
c  -----------------------------------------------------------------------------
10 4 -2.7 -8            imp:n,p =1      $ table Al
c  -----------------------------------------------------------------------------
c -----------------------------------------------------------------------------
c               FRONT TALLY CELLS CLOSE
c  -----------------------------------------------------------------------------
525 10 -0.001124 -12    imp:n,p =4      $  TALLY FRONT CLOSE
c  -----------------------------------------------------------------------------
c               SIDE TALLY CELLS (Bismuth side)
c  -----------------------------------------------------------------------------
624 10 -0.001124 -14    imp:n,p =4      $  TALLY SIDE Bi
c  -----------------------------------------------------------------------------
c               SIDE TALLY CELLS (pieno)
c  -----------------------------------------------------------------------------
724 10 -0.001124 -22    imp:n,p =4      $  TALLY SIDE PIENO
c  -----------------------------------------------------------------------------
c               shield
c  -----------------------------------------------------------------------------
1000 88 -11.35 -200 7 20 203  21 22  111  1 2 3 4 109 imp:n,p =4 $ Pb
1001 50 -1.06 -201 1 2 3 4 20 203 111 21 22  200 109 111  imp:n,p =4 $ Li
c  -----------------------------------------------------------------------------
c               dosimetry Bi_side
c  -----------------------------------------------------------------------------
1444 10 -0.001124 -1444 imp:n,p =4      $   tally biside 30cm
1445 10 -0.001124 -1445 imp:n,p =4      $   tally biside 60cm
1446 10 -0.001124 -1446 imp:n,p =4      $   tally biside 100cm
1447 10 -0.001124 -1447 imp:n,p =4      $   tally biside 150cm
1448 10 -0.001124 -1448 imp:n,p =4      $   tally biside 200cm
1449 10 -0.001124 -1449 imp:n,p =4      $   tally biside 300cm
c  -----------------------------------------------------------------------------
c               dosimetry epi_side
c  -----------------------------------------------------------------------------
1454 10 -0.001124 -1454 imp:n,p =4      $   tally epi 30cm
1455 10 -0.001124 -1455 imp:n,p =4      $   tally epi 60cm
1456 10 -0.001124 -1456 imp:n,p =4      $   tally epi 100cm
1457 10 -0.001124 -1457 imp:n,p =4      $   tally epi 150cm
1458 10 -0.001124 -1458 imp:n,p =4      $   tally epi 200cm
1459 10 -0.001124 -1459 imp:n,p =4      $   tally epi 300cm
c  -----------------------------------------------------------------------------
c               dosimetry top
c  -----------------------------------------------------------------------------
1464 10 -0.001124 -1464 imp:n,p =4      $   tally sup 30cm
1465 10 -0.001124 -1465 imp:n,p =4      $   tally sup 60cm
1466 10 -0.001124 -1466 imp:n,p =4      $   tally sup 100cm
1467 10 -0.001124 -1467 imp:n,p =4      $   tally sup 150cm
1468 10 -0.001124 -1468 imp:n,p =4      $   tally sup 200cm
1469 10 -0.001124 -1469 imp:n,p =4      $   tally sup 300cm
c  -----------------------------------------------------------------------------
c               dosimetry front
c  -----------------------------------------------------------------------------
1474 10 -0.001124 -1474 imp:n,p =4      $   tally front 30cm
1475 10 -0.001124 -1475 imp:n,p =4      $   tally front 60cm
```

```
1476 10 -0.001124 -1476 imp:n,p =4      $   tally front 100cm
1477 10 -0.001124 -1477 imp:n,p =4      $   tally front 150cm
1478 10 -0.001124 -1478 imp:n,p =4      $   tally front 200cm
1479 10 -0.001124 -1479 imp:n,p =4      $   tally front 300cm

c  --------------------------------------------------------------------------
c
c               SURFACE AND MACROBODY
c
c  --------------------------------------------------------------------------
1 rcc 42 27.5 -24 0 0 86.5 2.75         $ cl
2 rcc 42 27.5 -24 0 0 75.5 3.25         $ cl iron
3 rcc 42 27.5 51.5 0 0 11.5 3.25        $ cl (Al)
4 rcc 42 27.5 27 0 0 36.5 3.75          $ cl teflon
7 rpp 8.25 90.5 -47.5 100.5 -4 124      $ grafite box
8 rpp -11.75 110.5 -49.5 -47.5 -24 144  $ table Al
200 rpp -8.25 105.5 -47.5 115.5 -19 139        $ shield pb
201 rpp -12.75 110.5 -47.5 120.5 -24 144       $ shiel poli li
12 rpp 37.85 46.15 22 33 144 145               $ cella tally front close
14 rpp 105.5 106.5 22 33 55.4 68.6      $ cella tally side (Bismuth)
22 rpp -9.25 -8.25 22 33 55.4 68.6      $ cella tally side (pieno)
20 rpp 83.5 105.5 22.5 32.5 57 67       $ box Bi
203 rpp 105.5 110.5 22 33 55.4 68.6     $ vuoto davanti bi
50 rpp 14.75 62.25 16.25 38.75 50.75 73.25      $  teflon triple
52 rpp 16.75 17.75 16.25 38.75 50.75 73.25      $
53 rpp 16.25 16.75 16.25 38.75 50.75 73.25      $
54 rpp 14.75 16.25 16.25 38.75 50.75 73.25      $
55 rpp 13.75 14.75 16.25 38.75 50.75 73.25      $
56 rpp 13.25 13.75 16.25 38.75 50.75 73.25      $
57 rpp 11.75 13.25 16.25 38.75 50.75 73.25      $
58 rpp 10.75 11.75 16.25 38.75 50.75 73.25      $
59 rpp 10.25 10.75 16.25 38.75 50.75 73.25      $
60 rpp 8.75 10.25 16.25 38.75 50.75 73.25       $
61 rpp 7.75 8.75 16.25 38.75 50.75 73.25        $
63 rpp 7.25 7.75 16.25 38.75 50.75 73.25        $
64 rpp 5.75 7.25 16.25 38.75 50.75 73.25        $
65 rpp 4.75 5.75 16.25 38.75 50.75 73.25        $
66 rpp 4.25 4.75 16.25 38.75 50.75 73.25        $
67 rpp 2.75 4.25 16.25 38.75 50.75 73.25        $
68 rpp 1.75 2.75 16.25 38.75 50.75 73.25        $
69 rpp 1.25 1.75 16.25 38.75 50.75 73.25        $
70 rpp -0.25 1.25 16.25 38.75 50.75 73.25       $
71 rpp -1.25 -0.25 16.25 38.75 50.75 73.25      $
72 rpp -1.75 -1.25 16.25 38.75 50.75 73.25      $
73 rpp -3.25 -1.75 16.25 38.75 50.75 73.25      $
74 rpp -3.75 -3.25 16.25 38.75 50.75 73.25      $
75 rpp -4.25 -3.75 16.25 38.75 50.75 73.25      $
76 rpp -4.75 -4.25 16.25 38.75 50.75 73.25      $
77 rpp -5.25 -4.75 16.25 38.75 50.75 73.25      $
78 rpp -5.75 -5.25 16.25 38.75 50.75 73.25      $
79 rpp -6.25 -5.75 16.25 38.75 50.75 73.25      $
80 rpp -6.75 -6.25 16.25 38.75 50.75 73.25      $
81 rpp -7.25 -6.75 16.25 38.75 50.75 73.25      $
82 rpp -7.75 -7.25 16.25 38.75 50.75 73.25      $
83 rpp -8.25 -7.75 16.25 38.75 50.75 73.25      $
c 62 rpp -10.25 -7.25 11.75 43.25 46.25 77.75   $ shield Pb
21 rpp -11.75 38.25 16.25 38.75 50.75 73.25     $ ch
c 100 rpp -9.75 -7.25 12.25 42.75 46.75 77.25   $ Rivest lit
109 rpp -12.75 -8.25 16.25 38.75 50.75 73.25    $ front epi
111 rpp -12.75 38.25 12.25 42.75 46.75 77.25    $ shiel channel
112 rpp -12.75 14.75 16.25 38.75 50.75 73.25    $ ch sandwich
117 rpp -500 584 -212.5 520 -500 532            $ environment
1310 c/x 27.5 62 5                              $   tally
1444 rpp 135.5 136.5 22 33 55.4 68.6            $   tally biside 30cm
1445 rpp 165.5 166.5 22 33 55.4 68.6            $   tally biside 60cm
1446 rpp 205.5 206.5 22 33 55.4 68.6            $   tally biside 100cm
1447 rpp 255.5 256.5 22 33 55.4 68.6            $   tally biside 150cm
1448 rpp 305.5 306.5 22 33 55.4 68.6            $   tally biside 200cm
1449 rpp 405.5 406.5 22 33 55.4 68.6            $   tally biside 300cm
1454 rpp -39.25 -38.25 22 33 55.4 68.6          $   tally epi 30cm
1455 rpp -69.25 -68.25 22 33 55.4 68.6          $   tally epi 60cm
1456 rpp -109.25 -108.25 22 33 55.4 68.6        $   tally epi 100cm
1457 rpp -159.25 -158.25 22 33 55.4 68.6        $   tally epi 150cm
```

```
1458 rpp -209.25 -208.25 22 33 55.4 68.6        $   tally epi 200cm
1459 rpp -309.25 -308.25 22 33 55.4 68.6        $   tally epi 300cm
1463 rpp 37 47 121.5 122.5 57 67                $ tally sup 0
1464 rpp 37 47 150.5 151.5 57 67                $ tally sup 30
1465 rpp 37 47 180.5 181.5 57 67                $ tally sup 60
1466 rpp 37 47 220.5 221.5 57 67                $ tally sup 100
1467 rpp 37 47 270.5 271.5 57 67                $ tally sup 150
1468 rpp 37 47 320.5 321.5 57 67                $ tally sup 200
1469 rpp 37 47 420.5 421.5 57 67                $ tally sup 300
1473 rpp 37 47 22.5 32.5 145 146                $ tally front 0
1474 rpp 37 47 22.5 32.5 184 185                $ tally front 30
1475 rpp 37 47 22.5 32.5 214 215                $ tally front 60
1476 rpp 37 47 22.5 32.5 254 255                $ tally front 100
1477 rpp 37 47 22.5 32.5 304 305                $ tally front 150
1478 rpp 37 47 22.5 32.5 354 355                $ tally front 200
1479 rpp 37 47 22.5 32.5 454 455                $ tally front 300
c    ---------------------

mode  n p
c
c  ----------------------------------------------------------------------------
c      Materials
c  ----------------------------------------------------------------------------
c       Graphite         rho=-1.7
m2      6000.70c    1
mt2     Grph.10t
c        Aluminium       rho=-2.7
m4      13027.70c   1
c       Heavy water
c m5      8016.70c   1   1001.70c 2
c mt5   Lwtr.01t
c       Teflon           rho=-2.2
m6      6000.70c   1   9019.70c 2
c       iron    rho=-7.75
m7      24000.50c   -0.19   28058.70c  -0.09
        6000.70c    -0.0008 25055.70c  -0.02
        14000.60c   -0.01   15031.70c  -0.00045
        16032.70c   -0.0003 26000.55c  -0.68845
c       LiF
c m8    3006.70c   0.03735    $ Li-6
c       3007.70c   0.46265    $ Li-7
c       9019.70c   0.5        $ F-19
c       Aria
m10     6000.70c .000125  7014.70c .6869
        8016.70c .301248  18000.35c .011717
c       Bismuth          rho=-9.8
m12     83209.70c        1
c       Titanium commercial Ti6Al4V Grade5
m9      22000.60c -0.94 13027.70c -0.06
c    Material 6 lithium-doped polyethylene (nat) (as suppl by JCS) rho=-1.06
m50   1001.60c          -0.086  $MAT
      3006.60c       -0.004875 3007.60c       -0.070125 6000.60c         -0.5776
      8016.60c       -0.261333 17000.60c       -4e-005
mt50    poly.60t
c       Li2CO3 NOT enriched              rho=-2.11
m14     3006.70c 0.15 3007.70c 1.85 6000.70c 1 8016.70c 3
c       Piombo           rho=-11.35
m88     82204 0.014000
        82206.70c 0.241000
        82207.70c 0.221000
        82208.70c 0.524000
c ***********************************************************************
c  Neutron source Be-9(p,n) (see heading for reference)
c  beam energy = 5 MeV
c  yielding emission directions: 120, 100, 90, 80, 60, 40, 20,0
c  Yield reported in neutron/(sr*microC)
c  Parabolic distribution (si1,sp1) along X axis of absolute reference system
c  ************************************************************************
sdef pos 42 27.5 62.0000001 vec=0 0 1 dir=d4 erg fdir=d5
c   ------------------------------------------------------------------
c   ------------------------------------------------------------------
c         130    120   110    100      95       90 85       80
si4   A   -0.6428 -0.5 -0.342 -0.17365 -0.087156 0  0.087156 0.17365
```

```
       0.342 0.5 0.6428 0.766 0.866 0.9397 0.98481 1
c      70    60  50     40    30    20     10      0
c
c  yileding direction probability (% total)
c      130    120   110    100      95       90   85    80
sp4    5.6151097499 5.5640632976 5.5130168453 5.4619703931 5.3088310362
       5.1556916794 5.1301684533 5.1046452272 4.8494129658 4.5941807044
       5.6661562021 6.7381316998 7.6569678407 8.5758039816 9.213884635
       9.8519652884
c      70    60  50     40    30    20     10      0
c
c     source spectra in 8 yileding directions                           c
ds5  S 31 31 32 32 33 33 34 34 35 35 36 36 37 37 38
c
c       energy bin (MeV) and yielding
c
c -------*---------*---------*---------*---------*---------*---------*---------*
si31 A 0.298 0.328 0.358 0.391 0.426 0.464 0.503
       0.543 0.585 0.627 0.67 0.714 0.758 0.802
       0.847 0.891 0.936 0.982 1.027 1.074 1.12
       1.166 1.212 1.259 1.306 1.353 1.4 1.448
       1.495 1.542 1.59 1.638 1.685 1.733 1.781
       1.829 1.877 1.925 1.973 2.021 2.069 2.118
sp31   114600 90240 99160 117300 125500 132300 129900
       129300 127900 125300 121900 117900 114100 111200
       110000 110800 113000 115900 118200 121000 123800
       127300 131700 137700 144300 151300 158700 166500
       172700 177000 178900 177700 173100 165500 152700
       132300 106400 78360 51220 27620 9915 170.783
si32 A 0.298 0.328 0.358 0.391 0.426 0.464 0.503
       0.543 0.585 0.627 0.67 0.714 0.758 0.802
       0.847 0.891 0.936 0.982 1.027 1.074 1.12
       1.166 1.212 1.259 1.306 1.353 1.4 1.448
       1.495 1.542 1.59 1.638 1.685 1.733 1.781
       1.829 1.877 1.925 1.973 2.021 2.069 2.118
       2.166 2.214 2.263 2.311
sp32   38440 30970 71370 120000 148300 148800 147900
       144700 141400 137000 130800 124100 118300 114000
       111500 110800 111500 112800 113500 114500 115400
       116000 116800 118400 120200 121700 122600 123700
       124200 124400 124900 125900 126700 127900 128300
       127900 126100 122500 115800 103600 85980 65280
       43680 24090 8909 119.127
si33 A 0.263 0.297 0.331 0.37 0.411 0.454 0.499
       0.545 0.592 0.639 0.687 0.736 0.785 0.834
       0.883 0.933 0.983 1.034 1.084 1.135 1.185
       1.237 1.288 1.339 1.391 1.442 1.494 1.546
       1.598 1.65 1.702 1.754 1.806 1.858 1.91
       1.963 2.015 2.067 2.12 2.172 2.225 2.277
       2.33 2.383 2.435
sp33   51530 48330 74410 102900 115500 127600 133000
       133600 131700 128600 124700 120800 117400 114700
       113000 111900 110600 109400 108400 107700 107200
       107400 107900 108400 108800 108600 108200 108000
       107700 107500 106900 106000 104500 102800 100500
       97220 91520 84190 74040 61470 47220 32570
       18750 8621 1594
si34 A 0.298 0.328 0.358 0.391 0.426 0.464 0.503
       0.543 0.585 0.627 0.67 0.714 0.758 0.802
       0.847 0.891 0.936 0.982 1.027 1.074 1.12
       1.166 1.212 1.259 1.306 1.353 1.4 1.448
       1.495 1.542 1.59 1.638 1.685 1.733 1.781
       1.829 1.877 1.925 1.973 2.021 2.069 2.118
       2.166 2.214 2.263 2.311 2.359 2.408 2.456
       2.505 2.554
sp34   158000 126100 168400 177000 166400 151600 138900
       128000 119200 113000 109000 106200 104700 104200
       104300 104400 104300 103800 103200 103100 103000
       102700 102100 101000 99300 97370 95310 93220
       91060 89060 87150 85240 83360 81900 80420
       78790 76890 74750 72540 70120 66770 62240
       56430 49410 41120 32080 23130 14920 7958
       2861 57.499
```

```
si35 A 0.298 0.328 0.358 0.391 0.426 0.464 0.503
       0.543 0.585 0.627 0.67 0.714 0.758 0.802
       0.847 0.891 0.936 0.982 1.027 1.074 1.12
       1.166 1.212 1.259 1.306 1.353 1.4 1.448
       1.495 1.542 1.59 1.638 1.685 1.733 1.781
       1.829 1.877 1.925 1.973 2.021 2.069 2.118
       2.166 2.214 2.263 2.311 2.359 2.408 2.456
       2.505 2.554 2.602 2.651 2.699 2.748 2.797
sp35   129600 103700 137700 152700 167000 163600 161600
       156100 147800 137200 125500 117300 111900 106600
       102500 99910 98460 97630 96750 95970 95070
       93970 92570 90720 88310 85420 82210 78820
       75300 71730 68210 64820 61510 58400 55610
       53160 51130 49280 47590 46060 44680 43550
       42440 41530 40680 39570 37860 34730 30330
       25240 19760 14260 9224 4932 1779 35.616
si36 A 0.298 0.328 0.358 0.391 0.426 0.464 0.503
       0.543 0.585 0.627 0.67 0.714 0.758 0.802
       0.847 0.891 0.936 0.982 1.027 1.074 1.12
       1.166 1.212 1.259 1.306 1.353 1.4 1.448
       1.495 1.542 1.59 1.638 1.685 1.733 1.781
       1.829 1.877 1.925 1.973 2.021 2.069 2.118
       2.166 2.214 2.263 2.311 2.359 2.408 2.456
       2.505 2.554 2.602 2.651 2.699 2.748 2.797
       2.845 2.894 2.942 2.991
sp36   205800 165700 263000 318200 285700 257000 223400
       211400 198900 181300 163100 149100 134400 122000
       111900 104800 99920 96550 93870 91640 89650
       87800 86070 84540 83100 81650 80080 78430
       76640 74840 73120 71460 69840 68480 67350
       66440 65790 65440 65320 65630 66600 68330
       70330 72880 76400 80650 85440 90830 95620
       100200 103100 103600 100100 90670 76600 59140
       40280 22660 8370 52.247
si37 A 0.298 0.328 0.358 0.391 0.426 0.464 0.503
       0.543 0.585 0.627 0.67 0.714 0.758 0.802
       0.847 0.891 0.936 0.982 1.027 1.074 1.12
       1.166 1.212 1.259 1.306 1.353 1.4 1.448
       1.495 1.542 1.59 1.638 1.685 1.733 1.781
       1.829 1.877 1.925 1.973 2.021 2.069 2.118
       2.166 2.214 2.263 2.311 2.359 2.408 2.456
       2.505 2.554 2.602 2.651 2.699 2.748 2.797
       2.845 2.894 2.942 2.991 3.04 3.089 3.138
sp37   99170 79918.8 128122 214508 235282 226634 235564
       236598 228044 212628 192042 169764 150306 134984
       123892 116466 111108 106596 102366 98230 94376
       90644.2 87344.8 84543.6 82212.4 80266.6 78781.4 77879
       77409 77333.8 77672.2 78386.6 79411.2 80990.4 82992.6
       85474.2 88557.4 92289.2 96350 100768 105374 110450
       115902 121918 129062 136206 143538 151904 159800
       168354 177002 183206 187342 185368 177472 161398
       138368 111390 82438 54491.8 29816.8 10922.8 213.6432
si38 A 0.298 0.328 0.358 0.391 0.426 0.464 0.503
       0.543 0.585 0.627 0.67 0.714 0.758 0.802
       0.847 0.891 0.936 0.982 1.027 1.074 1.12
       1.166 1.212 1.259 1.306 1.353 1.4 1.448
       1.495 1.542 1.59 1.638 1.685 1.733 1.781
       1.829 1.877 1.925 1.973 2.021 2.069 2.118
       2.166 2.214 2.263 2.311 2.359 2.408 2.456
       2.505 2.554 2.602 2.651 2.699 2.748 2.797
       2.845 2.894 2.942 2.991 3.04 3.089 3.138
       3.186
sp38   84790 69520 237900 266000 270600 266900 256700
       254800 227700 189200 165800 141800 128800 120100
       115100 113100 111400 109700 107700 105300 102500
       98950 95270 91980 89420 87450 85840 84580
       83640 83290 83850 85270 87270 90110 93570
       97560 101900 106500 111200 116200 121900 129000
       136500 145100 155100 165600 177400 190400 202600
       215100 226400 234000 238700 237300 229000 210000
       183100 152200 118900 86040 55620 29810 10640
       21.166
c *****************************************************************************
```

```
c                sdef end
c ****************************************************************************
prdmp   j 5000000 j 2 j
c ****************************************************************************
c
c                *******************TALLY*************************
c
c ****************************************************************************
c
fc34 dose neutronica lato epi
f34:n           624
e34 0.5e-6 1e-2 20
fm34   2.53e9
c
fc314 dose neutronica lato front 30
f314:n          1474
e314 0.5e-6 1e-2 20
fm314   2.53e9
c
c
fc324 dose neutronica lato front 60
f324:n          1475
e324 0.5e-6 1e-2 20
fm324   2.53e9
c
fc334 dose neutronica lato front 100
f334:n          1476
e334 0.5e-6 1e-2 20
fm334   2.53e9
c
fc344 dose neutronica lato front 150
f344:n          1477
e344 0.5e-6 1e-2 20
fm344   2.53e9
c
fc354 dose neutronica lato front 200
f354:n          1478
e354 0.5e-6 1e-2 20
fm354   2.53e9
c
fc364 dose neutronica lato front 300
f364:n          1479
e364 0.5e-6 1e-2 20
fm364   2.53e9
c
c
c
fc132   Photon Dose at Beam Port Aperture Thermal
f132:p  8.1
fs132   -1310
sd132   78.5 1e20
e132    100.0
c     cell  flag  user  seg  mult  cos  ener  tim
c     1     1     last  last 1     last last  last
fm132   2.53e9
c
c
c
fc2314 photon Dose at Beam Port lato front 30
f2314:p         1474
e2314 0.5e-6 1e-2 20
fm2314   2.53e9
c
c
fc2324 photon Dose at Beam lato front 60
f2324:p         1475
e2324 0.5e-6 1e-2 20
fm2324   2.53e9
c
fc2334 photon Dose at Beam lato front 100
f2334:p         1476
e2334 0.5e-6 1e-2 20
fm2334   2.53e9
```

```
c
fc2344 photon Dose at Beam lato front 150
f2344:p          1477
e2344 0.5e-6 1e-2 20
fm2344   2.53e9
c
fc2354 photon Dose at Beam lato front 150
f2354:p          1478
e2354 0.5e-6 1e-2 20
fm2354   2.53e9
c
fc2364 photon Dose at Beam lato front 300
f2364:p          1479
e2364 0.5e-6 1e-2 20
fm2364   2.53e9
c
c       deltaU=0.23 per bin
c
c
c      This energy structure has bins of equal lethargy
c      with 10 bins per decade
c
#      e0
1.000E-10
1.259E-10
1.585E-10
1.995E-10
2.512E-10
3.162E-10
3.981E-10
5.012E-10
6.310E-10
7.943E-10
1.000E-09
1.259E-09
1.585E-09
1.995E-09
2.512E-09
3.162E-09
3.981E-09
5.012E-09
6.310E-09
7.943E-09
1.000E-08
1.259E-08
1.585E-08
1.995E-08
2.512E-08
3.162E-08
3.981E-08
5.012E-08
6.310E-08
7.943E-08
1.000E-07
1.259E-07
1.585E-07
1.995E-07
2.512E-07
3.162E-07
3.981E-07
5.012E-07
6.310E-07
7.943E-07
1.000E-06
1.259E-06
1.585E-06
1.995E-06
2.512E-06
3.162E-06
3.981E-06
5.012E-06
6.310E-06
7.943E-06
```

```
1.000E-05
1.259E-05
1.585E-05
1.995E-05
2.512E-05
3.162E-05
3.981E-05
5.012E-05
6.310E-05
7.943E-05
1.000E-04
1.259E-04
1.585E-04
1.995E-04
2.512E-04
3.162E-04
3.981E-04
5.012E-04
6.310E-04
7.943E-04
1.000E-03
1.259E-03
1.585E-03
1.995E-03
2.512E-03
3.162E-03
3.981E-03
5.012E-03
6.310E-03
7.943E-03
1.000E-02
1.259E-02
1.585E-02
1.995E-02
2.512E-02
3.162E-02
3.981E-02
5.012E-02
6.310E-02
7.943E-02
1.000E-01
1.259E-01
1.585E-01
1.995E-01
2.512E-01
3.162E-01
3.981E-01
5.012E-01
6.310E-01
7.943E-01
1.000E+00
1.259E+00
1.585E+00
1.995E+00
2.512E+00
3.162E+00
3.981E+00
5.012E+00
6.310E+00
7.943E+00
1.000E+01
1.259E+01
1.585E+01
1.995E+01
c
c
c
c   Photon attenuation Factors for A-150 Tissue Equivalent Plastic
c   Calculated from NIST data from report
c   J.H. Hubbell and S.M. Seltzer, Tables of X-Ray Mass Attenuation Coefficients
c   and Mass Energy-Absorption Coefficients 1 keV to 20 MeV for Elements Z = 1
c   to 92 and 48 Additional Substances of Dosimetric Interest, NISTIR 5632,
c   National Institute of Standards and Technology, (May 1995).
```

```
c   available online at  http://physics.nist.gov/xaamdi
c
c  Energy               Kerma              $   Energy              Kerma
c  (MeV)                (Gy cm2)           $  (MeV)               (Gy cm2)
#  de132                df132            $     de142               df142
   1.00000E-03          3.61456E-10        $   1.00000E-03         3.61456E-10
   1.50000E-03          1.74648E-10        $   1.50000E-03         1.74648E-10
   2.00000E-03          1.01644E-10        $   2.00000E-03         1.01644E-10
   3.00000E-03          4.60280E-11        $   3.00000E-03         4.60280E-11
   4.00000E-03          2.57698E-11        $   4.00000E-03         2.57698E-11
   4.03810E-03          2.52777E-11        $   4.03810E-03         2.52777E-11
   4.03811E-03          3.44584E-11        $   4.03811E-03         3.44584E-11
   5.00000E-03          2.32399E-11        $   5.00000E-03         2.32399E-11
   6.00000E-03          1.64193E-11        $   6.00000E-03         1.64193E-11
   8.00000E-03          9.40427E-12        $   8.00000E-03         9.40427E-12
   1.00000E-02          6.04190E-12        $   1.00000E-02         6.04190E-12
   1.50000E-02          2.65805E-12        $   1.50000E-02         2.65805E-12
   2.00000E-02          1.47563E-12        $   2.00000E-02         1.47563E-12
   3.00000E-02          6.62349E-13        $   3.00000E-02         6.62349E-13
   4.00000E-02          4.10868E-13        $   4.00000E-02         4.10868E-13
   5.00000E-02          3.21882E-13        $   5.00000E-02         3.21882E-13
   6.00000E-02          2.97529E-13        $   6.00000E-02         2.97529E-13
   8.00E-02             3.28259E-13        $   8.00E-02            3.28259E-13
   1.00E-01             4.03754E-13        $   1.00E-01            4.03754E-13
   1.50E-01             6.57543E-13        $   1.50E-01            6.57543E-13
   2.00E-01             9.41132E-13        $   2.00E-01            9.41132E-13
   3.00E-01             1.51840E-12        $   3.00E-01            1.51840E-12
   4.00E-01             2.07966E-12        $   4.00E-01            2.07966E-12
   5.00E-01             2.61559E-12        $   5.00E-01            2.61559E-12
   6.00E-01             3.12333E-12        $   6.00E-01            3.12333E-12
   8.00E-01             4.06574E-12        $   8.00E-01            4.06574E-12
   1.00E+00             4.91875E-12        $   1.00E+00            4.91875E-12
   1.25E+00             5.87607E-12        $   1.25E+00            5.87607E-12
   1.50E+00             6.74126E-12        $   1.50E+00            6.74126E-12
   2.00E+00             8.26094E-12        $   2.00E+00            8.26094E-12
   3.00E+00             1.08004E-11        $   3.00E+00            1.08004E-11
   4.00E+00             1.29778E-11        $   4.00E+00            1.29778E-11
   5.00E+00             1.49565E-11        $   5.00E+00            1.49565E-11
   6.00E+00             1.68327E-11        $  6.00E+00            1.68327E-11
   8.00E+00             2.04056E-11        $   8.00E+00            2.04056E-11
   1.00E+01             2.38568E-11        $   1.00E+01            2.38568E-11
   1.50E+01             3.23484E-11        $   1.50E+01            3.23484E-11
   2.00E+01             4.08561E-11        $   2.00E+01            4.08561E-11
c
c
c   Neutron Kerma Factors for A-150 Tissue Equivalent Plastic
c   Calculated from Kerma data in ICRU Report 63 and JENDL-3.2
c   cross sections and Q-values
c   These kerma factors are reported in
c   J.T. Goorley, W.S. Kiger, III, R.G. Zamenhof, "Reference Dosimetry
c   Calculations for Neutron Capture Therapy with Comparison of
c   Analytical and Voxel Models," Medical Physics, February 2002.
c
c  Neutron              Neutron             Neutron             Neutron
c  Energy               Kerma               Energy              Kerma
c  (MeV)                (Gy cm2)            (MeV)               (Gy cm2)
#   de34                df34          $   de42                  df42
1.00000E-10             4.44494E-12   $   1.00000E-10            4.44494E-12
2.53000E-08             2.79626E-13   $   2.53000E-08            2.79626E-13
3.60000E-08             2.37072E-13   $   3.60000E-08            2.37072E-13
6.30000E-08             1.78919E-13   $   6.30000E-08            1.78919E-13
1.10000E-07             1.35666E-13   $   1.10000E-07            1.35666E-13
2.00000E-07             1.00915E-13   $   2.00000E-07            1.00915E-13
3.60000E-07             7.50493E-14   $   3.60000E-07            7.50493E-14
5.00000E-07             6.38492E-14   $   5.00000E-07            6.38492E-14
6.30000E-07             5.69897E-14   $   6.30000E-07            5.69897E-14
1.10000E-06             4.32088E-14   $   1.10000E-06            4.32088E-14
2.00000E-06             3.22046E-14   $   2.00000E-06            3.22046E-14
3.60000E-06             2.42501E-14   $   3.60000E-06            2.42501E-14
6.30000E-06             1.87500E-14   $   6.30000E-06            1.87500E-14
1.10000E-05             1.48721E-14   $   1.10000E-05            1.48721E-14
2.00000E-05             1.23297E-14   $   2.00000E-05            1.23297E-14
3.60000E-05             1.13995E-14   $   3.60000E-05            1.13995E-14
```

```
6.30000E-05          1.23893E-14  $  6.30000E-05          1.23893E-14
1.10000E-04          1.58294E-14  $  1.10000E-04          1.58294E-14
2.00000E-04          2.40881E-14  $  2.00000E-04          2.40881E-14
2.36228E-04          2.75903E-14  $  2.36228E-04          2.75903E-14
2.85955E-04          3.24685E-14  $  2.85955E-04          3.24685E-14
3.17034E-04          3.55456E-14  $  3.17034E-04          3.55456E-14
3.41898E-04          3.80188E-14  $  3.41898E-04          3.80188E-14
3.57438E-04          3.95688E-14  $  3.57438E-04          3.95688E-14
3.60000E-04          3.98246E-14  $  3.60000E-04          3.98246E-14
3.69869E-04          4.08154E-14  $  3.69869E-04          4.08154E-14
3.76085E-04          4.14400E-14  $  3.76085E-04          4.14400E-14
3.82301E-04          4.20649E-14  $  3.82301E-04          4.20649E-14
3.86186E-04          4.24556E-14  $  3.86186E-04          4.24556E-14
3.89294E-04          4.27683E-14  $  3.89294E-04          4.27683E-14
3.92013E-04          4.30419E-14  $  3.92013E-04          4.30419E-14
3.93567E-04          4.31983E-14  $  3.93567E-04          4.31983E-14
3.94927E-04          4.33352E-14  $  3.94927E-04          4.33352E-14
3.95704E-04          4.34134E-14  $  3.95704E-04          4.34134E-14
3.96384E-04          4.34819E-14  $  3.96384E-04          4.34819E-14
3.96772E-04          4.35209E-14  $  3.96772E-04          4.35209E-14
3.97161E-04          4.35601E-14  $  3.97161E-04          4.35601E-14
3.97404E-04          4.35846E-14  $  3.97404E-04          4.35846E-14
3.97598E-04          4.36041E-14  $  3.97598E-04          4.36041E-14
3.97841E-04          4.36286E-14  $  3.97841E-04          4.36286E-14
3.97920E-04          4.36365E-14  $  3.97920E-04          4.36365E-14
3.97960E-04          4.36405E-14  $  3.97960E-04          4.36405E-14
3.98000E-04          4.36446E-14  $  3.98000E-04          4.36446E-14
3.98040E-04          4.36486E-14  $  3.98040E-04          4.36486E-14
3.98080E-04          4.36526E-14  $  3.98080E-04          4.36526E-14
3.98159E-04          4.36606E-14  $  3.98159E-04          4.36606E-14
3.98277E-04          4.36725E-14  $  3.98277E-04          4.36725E-14
3.98512E-04          4.36961E-14  $  3.98512E-04          4.36961E-14
3.98747E-04          4.37198E-14  $  3.98747E-04          4.37198E-14
3.98982E-04          4.37434E-14  $  3.98982E-04          4.37434E-14
3.99453E-04          4.37909E-14  $  3.99453E-04          4.37909E-14
3.99923E-04          4.38382E-14  $  3.99923E-04          4.38382E-14
4.00746E-04          4.39211E-14  $  4.00746E-04          4.39211E-14
4.01687E-04          4.40158E-14  $  4.01687E-04          4.40158E-14
4.03334E-04          4.41817E-14  $  4.03334E-04          4.41817E-14
4.05215E-04          4.43712E-14  $  4.05215E-04          4.43712E-14
4.08508E-04          4.47030E-14  $  4.08508E-04          4.47030E-14
4.12271E-04          4.50822E-14  $  4.12271E-04          4.50822E-14
4.16975E-04          4.55564E-14  $  4.16975E-04          4.55564E-14
4.24501E-04          4.63153E-14  $  4.24501E-04          4.63153E-14
4.35791E-04          4.74546E-14  $  4.35791E-04          4.74546E-14
4.50844E-04          4.89747E-14  $  4.50844E-04          4.89747E-14
4.73423E-04          5.12572E-14  $  4.73423E-04          5.12572E-14
5.03528E-04          5.43043E-14  $  5.03528E-04          5.43043E-14
5.48686E-04          5.88820E-14  $  5.48686E-04          5.88820E-14
6.08897E-04          6.49960E-14  $  6.08897E-04          6.49960E-14
6.30000E-04          6.71412E-14  $  6.30000E-04          6.71412E-14
1.10000E-03          1.14963E-13  $  1.10000E-03          1.14963E-13
2.00000E-03          2.05814E-13  $  2.00000E-03          2.05814E-13
2.20448E-03          2.26359E-13  $  2.20448E-03          2.26359E-13
2.92701E-03          2.98715E-13  $  2.92701E-03          2.98715E-13
3.40870E-03          3.46783E-13  $  3.40870E-03          3.46783E-13
3.60000E-03          3.65840E-13  $  3.60000E-03          3.65840E-13
3.64954E-03          3.70713E-13  $  3.64954E-03          3.70713E-13
3.81312E-03          3.88463E-13  $  3.83018E-03          3.88463E-13
3.95060E-03          4.00283E-13  $  3.95060E-03          4.00283E-13
4.02586E-03          4.07664E-13  $  4.02586E-03          4.07664E-13
4.08607E-03          4.13566E-13  $  4.08607E-03          4.13566E-13
4.13123E-03          4.17991E-13  $  4.13123E-03          4.17991E-13
4.16134E-03          4.20941E-13  $  4.16134E-03          4.20941E-13
4.18768E-03          4.23520E-13  $  4.18768E-03          4.23520E-13
4.20273E-03          4.24994E-13  $  4.20273E-03          4.24994E-13
4.21778E-03          4.26468E-13  $  4.21778E-03          4.26468E-13
4.22531E-03          4.27205E-13  $  4.22531E-03          4.27205E-13
4.23284E-03          4.27942E-13  $  4.23284E-03          4.27942E-13
4.23848E-03          4.28494E-13  $  4.23848E-03          4.28494E-13
4.24224E-03          4.28863E-13  $  4.24224E-03          4.28863E-13
4.24507E-03          4.29140E-13  $  4.24507E-03          4.29140E-13
4.24695E-03          4.29324E-13  $  4.24695E-03          4.29324E-13
```

```
4.24836E-03        4.29462E-13  $  4.24836E-03        4.29462E-13
4.24930E-03        4.29554E-13  $  4.24930E-03        4.29554E-13
4.25024E-03        4.29646E-13  $  4.25024E-03        4.29646E-13
4.25071E-03        4.29692E-13  $  4.25071E-03        4.29692E-13
4.25118E-03        4.29738E-13  $  4.25118E-03        4.29738E-13
4.25165E-03        4.29784E-13  $  4.25165E-03        4.29784E-13
4.25183E-03        4.29801E-13  $  4.25183E-03        4.29801E-13
4.25191E-03        4.29809E-13  $  4.25191E-03        4.29809E-13
4.25200E-03        4.29818E-13  $  4.25200E-03        4.29818E-13
4.25209E-03        4.29827E-13  $  4.25209E-03        4.29827E-13
4.25217E-03        4.29835E-13  $  4.25217E-03        4.29835E-13
4.25235E-03        4.29852E-13  $  4.25235E-03        4.29852E-13
4.25262E-03        4.29879E-13  $  4.25262E-03        4.29879E-13
4.25299E-03        4.29915E-13  $  4.25299E-03        4.29915E-13
4.25346E-03        4.29961E-13  $  4.25346E-03        4.29961E-13
4.25419E-03        4.30032E-13  $  4.25419E-03        4.30032E-13
4.25493E-03        4.30105E-13  $  4.25493E-03        4.30105E-13
4.25641E-03        4.30250E-13  $  4.25641E-03        4.30250E-13
4.25788E-03        4.30394E-13  $  4.25788E-03        4.30394E-13
4.26047E-03        4.30647E-13  $  4.26047E-03        4.30647E-13
4.26342E-03        4.30936E-13  $  4.26342E-03        4.30936E-13
4.26859E-03        4.31442E-13  $  4.26859E-03        4.31442E-13
4.27449E-03        4.32019E-13  $  4.27449E-03        4.32019E-13
4.28188E-03        4.32743E-13  $  4.28188E-03        4.32743E-13
4.29369E-03        4.33898E-13  $  4.29369E-03        4.33898E-13
4.30550E-03        4.35054E-13  $  4.30550E-03        4.35054E-13
4.32912E-03        4.37365E-13  $  4.32912E-03        4.37365E-13
4.35274E-03        4.39676E-13  $  4.35274E-03        4.39676E-13
4.39408E-03        4.43719E-13  $  4.39408E-03        4.43719E-13
4.44133E-03        4.48339E-13  $  4.44133E-03        4.48339E-13
4.51219E-03        4.55264E-13  $  4.51219E-03        4.55264E-13
4.60668E-03        4.64494E-13  $  4.60668E-03        4.64494E-13
4.77204E-03        4.80634E-13  $  4.77204E-03        4.80634E-13
4.96102E-03        4.99058E-13  $  4.96102E-03        4.99058E-13
5.29173E-03        5.31250E-13  $  5.29173E-03        5.31250E-13
5.76417E-03        5.77135E-13  $  5.76417E-03        5.77135E-13
6.30000E-03        6.29042E-13  $  6.30000E-03        6.29042E-13
1.10000E-02        1.06321E-12  $  1.10000E-02        1.06321E-12
2.00000E-02        1.84214E-12  $  2.00000E-02        1.84214E-12
3.60000E-02        3.05259E-12  $  3.60000E-02        3.05259E-12
6.30000E-02        4.73058E-12  $  6.30000E-02        4.73058E-12
8.20000E-02        5.75862E-12  $  8.20000E-02        5.75862E-12
8.60000E-02        5.94719E-12  $  8.60000E-02        5.94719E-12
9.00000E-02        6.13575E-12  $  9.00000E-02        6.13575E-12
9.40000E-02        6.33318E-12  $  9.40000E-02        6.33318E-12
9.80000E-02        6.51159E-12  $  9.80000E-02        6.51159E-12
1.05000E-01        6.81119E-12  $  1.05000E-01        6.81119E-12
1.15000E-01        7.23270E-12  $  1.15000E-01        7.23270E-12
1.25000E-01        7.63403E-12  $  1.25000E-01        7.63403E-12
1.35000E-01        8.00675E-12  $  1.35000E-01        8.00675E-12
1.45000E-01        8.36788E-12  $  1.45000E-01        8.36788E-12
1.55000E-01        8.73740E-12  $  1.55000E-01        8.73740E-12
1.65000E-01        9.04968E-12  $  1.65000E-01        9.04968E-12
1.75000E-01        9.36736E-12  $  1.75000E-01        9.36736E-12
1.85000E-01        9.68121E-12  $  1.85000E-01        9.68121E-12
1.95000E-01        9.98580E-12  $  1.95000E-01        9.98580E-12
2.10000E-01        1.04076E-11  $  2.10000E-01        1.04076E-11
2.30000E-01        1.09545E-11  $  2.30000E-01        1.09545E-11
2.50000E-01        1.14481E-11  $  2.50000E-01        1.14481E-11
2.70000E-01        1.19096E-11  $  2.70000E-01        1.19096E-11
2.90000E-01        1.24743E-11  $  2.90000E-01        1.24743E-11
3.10000E-01        1.28289E-11  $  3.10000E-01        1.28289E-11
3.30000E-01        1.32964E-11  $  3.30000E-01        1.32964E-11
3.50000E-01        1.37555E-11  $  3.50000E-01        1.37555E-11
3.70000E-01        1.41255E-11  $  3.70000E-01        1.41255E-11
3.90000E-01        1.44907E-11  $  3.90000E-01        1.44907E-11
4.20000E-01        1.51419E-11  $  4.20000E-01        1.51419E-11
4.60000E-01        1.57566E-11  $  4.60000E-01        1.57566E-11
5.00000E-01        1.64266E-11  $  5.00000E-01        1.64266E-11
5.40000E-01        1.70759E-11  $  5.40000E-01        1.70759E-11
5.80000E-01        1.76556E-11  $  5.80000E-01        1.76556E-11
6.20000E-01        1.82752E-11  $  6.20000E-01        1.82752E-11
6.60000E-01        1.88736E-11  $  6.60000E-01        1.88736E-11
```

```
7.00000E-01           1.94039E-11  $  7.00000E-01           1.94039E-11
7.40000E-01           1.98649E-11  $  7.40000E-01           1.98649E-11
7.80000E-01           2.04259E-11  $  7.80000E-01           2.04259E-11
8.20000E-01           2.08799E-11  $  8.20000E-01           2.08799E-11
8.60000E-01           2.13469E-11  $  8.60000E-01           2.13469E-11
9.00000E-01           2.18163E-11  $  9.00000E-01           2.18163E-11
9.40000E-01           2.23092E-11  $  9.40000E-01           2.23092E-11
9.80000E-01           2.28603E-11  $  9.80000E-01           2.28603E-11
1.05000E+00           2.36298E-11  $  1.05000E+00           2.36298E-11
1.15000E+00           2.45460E-11  $  1.15000E+00           2.45460E-11
1.25000E+00           2.55497E-11  $  1.25000E+00           2.55497E-11
1.35000E+00           2.65177E-11  $  1.35000E+00           2.65177E-11
1.45000E+00           2.73629E-11  $  1.45000E+00           2.73629E-11
1.55000E+00           2.80958E-11  $  1.55000E+00           2.80958E-11
1.65000E+00           2.89011E-11  $  1.65000E+00           2.89011E-11
1.75000E+00           2.97242E-11  $  1.75000E+00           2.97242E-11
1.85000E+00           3.05147E-11  $  1.85000E+00           3.05147E-11
1.95000E+00           3.11357E-11  $  1.95000E+00           3.11357E-11
2.10000E+00           3.27196E-11  $  2.10000E+00           3.27196E-11
2.30000E+00           3.35541E-11  $  2.30000E+00           3.35541E-11
2.50000E+00           3.49891E-11  $  2.50000E+00           3.49891E-11
2.70000E+00           3.68385E-11  $  2.70000E+00           3.68385E-11
2.90000E+00           3.95773E-11  $  2.90000E+00           3.95773E-11
3.10000E+00           3.89012E-11  $  3.10000E+00           3.89012E-11
3.30000E+00           4.23470E-11  $  3.30000E+00           4.23470E-11
3.50000E+00           4.43569E-11  $  3.50000E+00           4.43569E-11
3.70000E+00           4.47748E-11  $  3.70000E+00           4.47748E-11
3.90000E+00           4.46120E-11  $  3.90000E+00           4.46120E-11
4.20000E+00           4.42501E-11  $  4.20000E+00           4.42501E-11
4.60000E+00           4.38531E-11  $  4.60000E+00           4.38531E-11
5.00000E+00           4.46659E-11  $  5.00000E+00           4.46659E-11
5.40000E+00           4.53246E-11  $  5.40000E+00           4.53246E-11
5.80000E+00           4.65006E-11  $  5.80000E+00           4.65006E-11
6.20000E+00           4.89765E-11  $  6.20000E+00           4.89765E-11
6.60000E+00           4.72068E-11  $  6.60000E+00           4.72068E-11
7.00000E+00           4.79027E-11  $  7.00000E+00           4.79027E-11
7.40000E+00           5.11996E-11  $  7.40000E+00           5.11996E-11
7.80000E+00           5.52665E-11  $  7.80000E+00           5.52665E-11
8.20000E+00           5.23236E-11  $  8.20000E+00           5.23236E-11
8.60000E+00           5.20473E-11  $  8.60000E+00           5.20473E-11
9.00000E+00           5.57453E-11  $  9.00000E+00           5.57453E-11
9.40000E+00           5.78586E-11  $  9.40000E+00           5.78586E-11
9.80000E+00           5.67362E-11  $  9.80000E+00           5.67362E-11
1.05000E+01           5.70824E-11  $  1.05000E+01           5.70824E-11
1.15000E+01           5.98040E-11  $  1.15000E+01           5.98040E-11
1.25000E+01           6.29993E-11  $  1.25000E+01           6.29993E-11
1.35000E+01           6.43676E-11  $  1.35000E+01           6.43676E-11
1.45000E+01           6.62510E-11  $  1.45000E+01           6.62510E-11
1.60000E+01           6.90054E-11  $  1.60000E+01           6.90054E-11
1.80000E+01           7.18951E-11  $  1.80000E+01           7.18951E-11
2.00000E+01           7.23619E-11  $  2.00000E+01           7.23619E-11
c ************************************************************************
c
c              *******************MESH************************
c
c ************************************************************************
fmesh1124:n geom=xyz origin -400 27 -400              $ mesh source zx
        imesh 500 iints 900
        jmesh 28 jints 1
        kmesh 500 kints 900
        emesh=2e-7 5e-1 5
fmesh1134:n geom=xyz origin 41.5 -112.5 -400
        imesh 42.5 iints 1
        jmesh 200.5 jints 312
        kmesh 500 kints 900
        emesh=2e-7 5e-1 5
fmesh1144:n geom=xyz origin -400 -112.5 61.5
        imesh 500 iints 900
        jmesh 200.5 jints 312
        kmesh 62.5 kints 1
        emesh=2e-7 5e-1 5
c ************************************************************************
phys:n  20 20   $ neutron energy cutoff (analog Monte Carlo model)
```

```
phys:p
print    10 20 40 50 60 70 72 98 100 110 126 130 140 160 170
c void     1 21I 23 25 26 122I 149 150 151 152 153 154 155 156 155I 312
nps      5e+9

c***************************************************************
```

Bibliography

[1] G.L. Locher. Am. J. Roentgenol. Radium Ther. *Medical Physics*, pages 1–13, 1936.

[2] Japan Atomic Energy Agency Nuclear Data Center. *Cross-Section Graphs of JENDL-4.0.*

[3] J.C. Yanch. A Monte Carlo investigation of dosimetric properties of monoenergetic neutron beams for NCT. *Radiat. Res.*, pages 1–20, 126(1991).

[4] K. Hideghéty and W. Sauerwein. Postoperative treatment of glioblastoma with BNCT at the Petten irradiation facility. pages 111–116, 175(1999).

[5] Y. Immahori and S. Ueda. Positron emission tomography-based boron neutron capture therapy using boronophenylalanine for high-grade gliomas. *Clin. Cancer Res.*, pages 1833–41, 4(1998).

[6] R. Henriksson and J. Capala. Swedish Brain Tumor Study Group. *Radiither Oncology*, pages 183–191, 88(2008).

[7] H. Joensuu. Boron neutron capture therapy of brain tumors: clinical trials at the finnish facility using boronophenylalanine . *J. Neurooncol.*, pages 123–134, 62(2003).

[8] Pinelli et al. TAOrMINA: from the first idea to the application on the human liver. *International Congress on Neutron Capture Therapy, Essen, Germany*, pages 1065–1072, (2002).

[9] Suzuki et al. First attempt of boron neutron capture therapy (BNCT) for hepatocellular carcinoma. *Jpn. J. Clin. Oncol.*, pages 376–381, 37(2008).

[10] Gonzalez et al. First BNCT treatment of a skin melanoma in Argentina:dosimetric analysis and clinical outcome. *Applied Radiation and Isotopes*, page 1101–1105, 61(2004).

[11] L. Kankaanranta. Boron neutron capture therapy in the treatment of locally recurred head and neck cancer: final analysis of a phase I/II trial. *Int J Radiat Oncol Biol Phys*, pages 67–75, 82(2012).

[12] A.G.W. Sauerwein, A. Witting, Raymond Moss, and Y. Nakagawa. *Neutron Capture Therapy, Principles and Applications.* Springer, 2012.

[13] C. Yanch and T.E. Blue. Accelerator-based epithermal neutron sources for boron neutron capture therapy of brain tumors. *Journal of Neuro-Oncology*, pages 19–31, 62(2003).

[14] S. Agosteo, P. Colautti, J. Esposito, A. Fazzi, M.V. Introini, and A. Pola. Characterization of the energy distribution of neutrons generated by 5 MeV protons on a thick beryllium target at different emission angles. *Applied Radiation and Isotopes*, (2011).

[15] M. Stacey. *Nuclear Reactor Physics*. John Wiley Sons Inc, 2001.

[16] Liu et al. Neutron spectra measurement and comparison of the HFR and THOR BNCT beams. 67(2004)), journal = Appl Radiat Isot, pages = 137-140.

[17] Howard et al. Measurement of the Thick Target Be(p,n) Neutron Energy Spectra. *Nuclear Science and Engineering*, page 145–160, 138(2001).

[18] Hanna Koivunoro. *Dosimetry and Dose Planning in Boron Neutron Capture Therapy: Monte Carlo Studies*. HU-PD195. Agoust 2012.

[19] D.L. Bleuel, R.J. Donahue, B.A. Ludewigt, and J. Vujic. Designing accelerator-based epithermal neutron beams for boron neutron capture theraphy. *Medical Physics*, pages 561–569, 1998.

[20] Stuart Green. Developments in Accelerator based Boron Neutron Capture Therapy. *Radiation Physics and Chemestry*, pages 561–569, 51(1998).

[21] D.A. Allen and T.D. Beynon. A Design study for an accelerator-based epithermal neutron beam for BNCT. *Phys. Med. Biol.*, pages 807–821, 40(1995).

[22] M.S. Herrera, S.J. Gonzalez, D.M. Minsky, and A.J. Kreiner. Evaluation of performance of an accelerator-based BNCT facility for the treatment of different tumor targets. *Physica Medica*, pages 436–446, 29(2013).

[23] Nagler et al. Status of the SARAF Project. pages 168–170, (2006).

[24] Kobayashi et al. Development of Liquid Lithium Target of 7Li(p,n)7Be Reactions for accelerator based BNCT Irradiation System. *World Congress on Medical Physics and Biomedical Engineering*, pages 1907–1910, (2013).

[25] H. Tanaka, Y. Sakurai, M. Suzuki, T Takata, S. Maunaga, Y. Kinashi, G Kashino, Y. Liu, T. Mitsumoto, S. Yajiama, H. Tsutsui, M. Takada, A. Maruhashi, and O. Ono. Improvement of dose distribution on phantom by using ephitermal neutron source based on the Be(p,n) reaction using a 30 MeV proton cyclotron accelerator. *Applied Radiation and Isotopes*, pages S258–S261, 67(2009).

[26] Yamamoto et al. The status of Tsukuba BNCT Trial: BPA-Based Boron Neutron Capture Therapy Combined with X-ray Irradiation. *Applied Radiation and Isotopes*, pages 1817–1818, 69(2012).

[27] Kobayashi et al. Construction of a BNCT facility using an 8-MeV high power proton linac in Tokai. *Medical Applications*, pages 4083–4085, 08(2012).

[28] J.M. Verbeke. Neutron Beam Opyimization for BNCT Using the D-D D-T High Energy Neutron Sources. *Nuclear Technology*, pages 257–272, 129(2000).

[29] J. Reijonen. D-D neutron generator development at LBNL. *Applied Radiation and Isotopes*, pages 598–602, 63(2005).

[30] Salehi Danial, Sardari Dariush, and Milad Salehi. Evaluation of Design Neutron Filters in BNCT. *Open Access Scientific Reports*, 1:537, 2012.

[31] Denise B. Pelowitz. *MCNP6^{TM}User's Manual Version 1.0.* La-CP-13-00634, Rev.0, May 2013.

[32] NIST Physical Measurement Laboratory. *Radiation Dosimetry Data.*

[33] ICRP-60. *International Commission on Radiobiological Protection.* Vienna, 1991.

[34] IAEA TECDOC-1223. *Current status of neutron capture therapy.* Vienna, 2001.

[35] Bortolussi et al. Exploring boron neutron capture therapy for non-small cell lung cancer. 30(8)2014), journal = Phys Med, pages = 888-897.

[36] Hamidi et al. BNCT neutron beam characterization using a resonance absorption filter method. *Nucl Instrum Methods Phys Res*, page 99–105, 476(2002).

[37] Riley et al. Performance characteristics of the MIT fission converter based epithermal neutron beam. 48(2003)), journal = Phys Med Biol, pages = 943-958.

[38] Nakagawa et al. Clinical review of the Japanese experience with boron neutron capture therapy and a proposed strategy using epithermal neutron beams. 62(2003)), journal = J Neurooncol, pages = 87-99.

[39] Tung et al. Characteristics of the new THOR epithermal neutron beam for BNCT. 61(2004)), journal = Appl Radiat Isot, pages = 861-864.

[40] T. Seppaälä. FiR 1 epithermal neutron beam model and dose calculation for treatment planning in neutron capture therapy. (2002)), journal = Ph.D.Thesis. Report Series in Physics, HU-P-D103. University of Helsinki: Helsinki, Finland.

[41] Auterinen et al. Metamorphosis of a 35 years old Triga reactor into a modern BNCT facility. (2001)), journal = Frontiers in neutron capture therapy, pages = 267-275.

[42] Sakurai et al. The medical-irradiation characteristics for neutron capture therapy at the Heavy Water Neutron Irradiation Facility of Kyoto University Research Reactor. 29(2002)), journal = Med Phys, pages = 2328-2337.

[43] Binns et al. Dosimetric comparison of six epithermal neutron beams using an ellipsoidal water phantom. 29(2002)), journal = Research and development in neutron capture therapy, pages = 405-409.

[44] Brookhaven National Laboratory Nuclear Data Center. *Thermal Neutron Capture gamma's by Target.*

[45] Physical Measuremeent Laboratory National Institute of Standards and Tecnology. *Tables of X-Ray Mass Attenuation Coefficients and Mass Energy-Absorption Coefficients from 1 keV to 20 MeV for Z = 1 to 92.*

[46] John R. Lamarsh. *Introduction to NUCLEAR REACTOR THEORY.* Addison-Wesley, Reading (Massachusetts USA), 1966.

[47] M.S. Herrera, S.J. Gonzalez, A.A. Burlon, D.M. Minsky, and A.J. Kreiner. Treatment planning capability assessment of a beam shaping assembly fo accelerator-based BNCT. *Applied Radiation and Isotopes*, pages 1870–1873, (2011).

[48] M.S. Herrera, G.A. Moreno, and A.J. Kreiner. New method to evaluate the 7Li(p,n)7Be reaction near threshold. *Nuclear Instrument and Methods in Physics Research B*, pages 64–71, 349(2015).

[49] Christopher N. Culbertson, Stuart Green, Anna J. Mason, David Picton, Gareth Baugh, Richard P. Hugtenburg, Zaizthe Yin, Malcolm C. Scott, and John M. Nelson. In-phantom Characterisation studies at Birmingham Accelerator-Generated Epithermal Neutron Source (BAGINS) BNCT facility. *Applied Radiation and Isotopes*, pages 733–738, 61(2004).

[50] K.H. Beckurts and K. Wirtz. *Neutron Physics*. Springer-Berlag, Berlin, 1964.

[51] National Council on Radiation Protection NCRP and Measurement. *Protection Against Neutron Radiation, Report No.38*. 1971.

[52] Laboratori Nazionali di Legnaro INFN-LNL. CN Accelerator - 7 MV.

[53] E. Lewis. *Foundamentals of Nuclear Reactor Physics*. Academic Press, 2008.

Ringraziamenti

Vorrei ringraziare Silva e il Professor Altieri che con la loro quotidiana simpatia e passione in quello che fanno hanno reso quest'esperienza unica.

Grazie al Baldo e al Piga, perchè sono semplicemente loro.